Characterization of *Herschel*-selected strong lens candidates through *HST* and sub-mm/mm observations

E. Borsato [1]⋆ L. Marchetti [2,3,4]⋆ M. Negrello [5]⋆ E. M. Corsini [1,6]⋆ D. Wake [7] A. Amvrosiadis,[8] A. J. Baker,[9,10] T. J. L. C. Bakx [11,12] A. Beelen [13] S. Berta,[14] A. Beyer,[15] D. L. Clements [16] A. Cooray,[17] P. Cox [18] H. Dannerbauer,[19,20] G. de Zotti,[6] S. Dye [21] S. A. Eales,[5] A. Enia [22,23] D. Farrah,[24,25] J. Gonzalez-Nuevo [26,27] D. H. Hughes,[28] D. Ismail,[29] S. Jin [30,31] A. Lapi [32] M. D. Lehnert,[33] R. Neri [14] I. Pérez-Fournon,[19,20] D. A. Riechers,[15] G. Rodighiero [1,6] D. Scott,[34] S. Serjeant [35] F. Stanley,[14] S. Urquhart,[35] P. van der Werf,[36] M. Vaccari [3,4,37] L. Wang,[38,39] C. Yang [40] and A. Young [9]

Affiliations are listed at the end of the paper

ABSTRACT

We have carried out *Hubble Space Telescope* (*HST*) snapshot observations at 1.1 μm of 281 candidate strongly lensed galaxies identified in the wide-area extragalactic surveys conducted with the *Herschel Space Observatory*. Our candidates comprise systems with flux densities at 500 μm, $S_{500} \geq 80$ mJy. We model and subtract the surface brightness distribution for 130 systems, where we identify a candidate for the foreground lens candidate. After combining visual inspection, archival high-resolution observations, and lens subtraction, we divide the systems into different classes according to their lensing likelihood. We confirm 65 systems to be lensed. Of these, 30 are new discoveries. We successfully perform lens modelling and source reconstruction on 23 systems, where the foreground lenses are isolated galaxies and the background sources are detected in the *HST* images. All the systems are successfully modelled as a singular isothermal ellipsoid. The Einstein radii of the lenses and the magnifications of the background sources are consistent with previous studies. However, the background source circularized radii (between 0.34 and 1.30 kpc) are ∼3 times smaller than the ones measured in the sub-millimetre/millimetre for a similarly selected and partially overlapping sample. We compare our lenses with those in the Sloan Lens Advanced Camera for Surveys (ACS) Survey confirming that our lens-independent selection is more effective at picking up fainter and diffuse galaxies and group lenses. This sample represents the first step towards characterizing the near-infrared properties and stellar masses of the gravitationally lensed dusty star-forming galaxies.

Key words: gravitational lensing: strong – galaxies: high-redshift – galaxies: photometry.

1 INTRODUCTION

The very bright tail of the number counts of galaxies at sub-millimetre and millimetre (sub-mm/mm) wavelengths comprises a mixture of distinct galaxy populations: low-redshift ($z \lesssim 0.1$) late-type galaxies, flat spectrum radio sources, high-redshift ($z \gtrsim 1$) gravitationally lensed dusty star-forming galaxies (DSFGs), and hyper-luminous infrared galaxies (Negrello et al. 2007, 2010, 2017; Vieira et al. 2013; Wardlow et al. 2013; Nayyeri et al. 2016; Rowan-Robinson et al. 2018; Ward et al. 2022). This distribution allows us to efficiently select strong gravitational lensing systems by combining a flux density cut (e.g. $S_{500} \geq 100$ mJy at 500 μm) with shallow optical and radio surveys to remove the contaminants. This approach became

effective in the last decade thanks to the wide-area surveys carried out, in particular, by the *Herschel Space Observatory* (Pilbratt et al. 2010) and the South Pole Telescope (SPT, e.g. Vieira et al. 2010; Carlstrom et al. 2011; Mocanu et al. 2013). Negrello et al. (2017) and then Ward et al. (2022) identified 80 + 11 candidate lensed galaxies with $S_{500} \geq 100$ mJy in the > 600 deg^2 of the *Herschel*-Astrophysical Terahertz Large Area Survey (H-ATLAS, Eales et al. 2010). Bakx et al. (2018) extended the selection down to $S_{500} = 80$ mJy by including DSFGs with photometric redshift $z_{phot} > 2$, as derived from the sub-mm colours (the *Herschel* bright sources – HerBS – sample). At flux densities $S_{500} < 100$ mJy, the number density of unlensed DSFGs exponentially increases (see Negrello et al. 2007; Cai et al. 2013, for details); therefore, the HerBS sample is expected to contain a mixture of both lensed and unlensed DSFGs, with the latter dominating over the former at $S_{500\,\mu m} \lesssim 100$ mJy. Wardlow et al. (2013) identified 42 candidate high-z lensed DSFGs with $S_{500} \geq 80$ mJy in the 95 deg^2 of the *Herschel* Multi-tiered Extragalactic Survey (HerMES, Oliver et al. 2012), while Nayyeri

et al. (2016) published a catalogue of 77 candidate lensed DSFGs with $S_{500} \geq 100$ mJy in the 300 deg² of the HerMES Large Mode Survey (HeLMS, Oliver et al. 2012) and the 79 deg² of the *Herschel* Stripe 82 Survey (HerS; Viero et al. 2014). Following a different approach, González-Nuevo et al. (2012, 2019) lowered the Spectral and Photometric Imaging Receiver (SPIRE) flux density cut ($S_{350} \geq 85$ mJy at 350 μm and $S_{250} \geq 35$ mJy at 250 μm) constraints on both the *Herschel*/SPIRE colours and the presence of close-by near-infrared (near-IR) sources acting as potential lensing galaxies, increasing the number of strong lens candidates by a factor of ∼5.

Using a similar approach to Negrello et al. (2010) but at mm wavelengths, the SPT collaboration produced a sample of 48 candidate lensed galaxies with deboosted $S_{1.4} \geq 20$ mJy at 1.4 mm over an area of 2500 deg² (Vieira et al. 2013; Spilker et al. 2016; Everett et al. 2020; Reuter et al. 2020; Cai, Negrello & De Zotti 2022). Lastly, Cañameras et al. (2015) applied a combination of flux density cut and colour selection on candidates extracted from the *Planck* Catalogue of Compact Sources, identifying 11 lensed DSFGs. Later, Harrington et al. (2016), Berman et al. (2022), and Kamieneski et al. (2023a) identified 30 strongly lensed galaxies by cross-matching the *Planck* catalogue, the *WISE* All-Sky Survey, and the *Herschel* surveys. Three and two of these systems were also included in the Wardlow et al. (2013) and Negrello et al. (2017) samples, respectively.

To confirm whether a sub-mm/mm bright galaxy is gravitationally lensed, high-resolution follow-up observations are needed. The multiple images of a background source, which are the distinctive features of lensing, have typical separations of a few arcseconds. They can not be resolved by either *Herschel* (full width at half-maximum, FWHM ≃ 18, 24, and 35 arcsec at 250, 350, and 500 μm, respectively) or SPT (FWHM ≃ 1 arcmin at 1.4 mm). Because lensed DSFGs emit mostly in the far-IR/sub-mm/mm (Negrello et al. 2014), the best way to detect and characterize the multiple images is via high-angular resolution observations at sub-mm/mm wavelengths obtained with interferometers, such as the Atacama Large Millimetre Array (ALMA), the Submillimetre Array (SMA), and the Northern Extended Millimetre Array (NOEMA, e.g. Bussmann et al. 2013; Amvrosiadis et al. 2018). These data can then be used to reconstruct the intrinsic morphology of the background DSFGs via lens modelling techniques (e.g. Dye et al. 2018; Maresca et al. 2022), which provide crucial information on the spatial distribution of the gas and dust and on the star formation rate surface density in those galaxies (e.g. Cañameras et al. 2017; Yang et al. 2019; Jarugula et al. 2021; Sun et al. 2021; Dye et al. 2022). Interestingly, at these wavelengths, the object acting as a lens, which is usually a massive red-and-dead foreground elliptical galaxy with very low dust content, remains undetected, thus facilitating the source reconstruction. However, it is not possible to constrain all the physical properties of the lensed DSFGs with the long-wavelength data alone. Indeed, one parameter that remains elusive is the background source stellar mass, which is crucial to understand better the evolutionary stage of a galaxy (e.g. Renzini 2009). Constraining the stellar mass of the background sources requires them to be detected at optical/near-IR wavelengths, where the emission of the foreground lens dominates (e.g. Negrello et al. 2014). Hence, careful lens photometric modelling and subtraction are needed to reveal the lensed background sources in the high-resolution optical/near-IR images. This analysis represents the first step to constrain the stellar masses by fitting the background source spectral energy distribution (SED, Negrello et al. 2014).

So far, high-resolution near-IR follow-up observations of tens of sub-mm/mm selected candidate lensed galaxies have been obtained in the near-IR with the *Hubble Space Telescope* (*HST*, e.g. Negrello et al. 2014) and with ground-based telescopes exploiting adaptive

optics (e.g. Fu et al. 2012; Calanog et al. 2014; Messias et al. 2014). These observations are characterized by long integration times (i.e. from tens of minutes to hours) and have been mainly aimed at identifying and studying the background source. Instead, we report on *HST* snapshot observations of a much larger sample of 281 sub-mm bright *Herschel*-selected systems. The primary goal of these short observations is to efficiently confirm the gravitational lensing nature of the sub-mm selected systems either by detecting the characteristic lensing features, such as arcs or multiple images, or by identifying massive low-z early-type galaxies (ETGs) located at the position of the sub-mm emission and thus potentially acting as the lens. These observations represent the first step to enable more detailed follow-ups to study the background sources and, at the same time, provide data to study the properties of the lenses.

This paper is organized as it follows. Section 2 presents the full sample of candidates we have followed up with *HST* and details the *HST* snapshot observations. Section 3 discusses the visual classification of the *HST* images. In Section 4, we focus on the subsample of systems that show clear evidence of lensing features in the *HST* images and describe the fitting techniques adopted for modelling the surface brightness of the lenses. Section 5 presents the lens modelling we apply and the results for a subsample of candidates. Section 6 discusses our results, focusing on the comparison with the Sloan Lens ACS Survey (SLACS), while the main conclusions are summarized in Section 7. In this paper, we adopt the values of $H_0 = 67.7$ km s⁻¹ Mpc⁻¹, $\Omega_{0,\,m} = 0.31$, and $\Omega_{0,\,\Lambda} = 0.69$ from Planck18 cosmology (see Planck Collaboration VI 2020[1] for details).

2 SAMPLE, OBSERVATIONS, AND DATA REDUCTION

2.1 Sample selection

Our sample consists of candidate $z \gtrsim 1$ (gravitationally lensed and unlensed) DSFGs extracted from the *Herschel* wide-area extragalactic surveys (i.e. H-ATLAS, HerMES, HeLMS, and HerS) for which we obtained the *HST* snapshot observations described in the following section. Many of our targets are selected from Bussmann et al. (2013), Wardlow et al. (2013), Calanog et al. (2014), Nayyeri et al. (2016), Negrello et al. (2017), and Bakx et al. (2018). Due to the varying quality of *Herschel* and ancillary data available at the time of these different works, they could select candidates only in specific sky areas and applied slightly different selection criteria to identify their most reliable candidate lensed system. Nevertheless, these selections generally relied upon a bright flux density cut at 500 μm following the approach by Negrello et al. (2010). In summary, the objects we observed with *HST* were identified as candidate lensing systems by having either the flux density measured at 500 μm, $S_{500} \gtrsim 100$ mJy (as done in Wardlow et al. 2013, Nayyeri et al. 2016, Negrello et al. 2017) or by having $S_{500} \gtrsim 80$ mJy and photometric redshifts of the potential background source $z > 2$ (as the candidates presented in Bakx et al. 2018). Exceptions are the candidates from Calanog et al. (2014) that were selected by means of their bright ($S_{500} \gtrsim 80$ mJy) SPIRE 500 μm flux densities, but also thanks to multiwavelength observations and specific source-extraction techniques applied on deeper *Herschel* maps available only for the HerMES fields. We refer the reader to Calanog et al. (2014) for more details. As a result, Calanog et al. (2014) candidates include targets with flux densities at

---

[1] Available in the ASTROPY.COSMOLOGY package through ASTROPY, see Astropy Collaboration (2013, 2018).

500 μm below the flux limit used in the other quoted works. For the candidates in the H-ATLAS survey, we use the flux densities coming from Harris et al. (2012), Negrello et al. (2017), and Bakx et al. (2018), when available, if not, we adopt the flux densities published in the H-ATLAS Data Release 1 (DR1, Valiante et al. 2016) or Data Release 2 (DR2, Maddox et al. 2018). The candidates belonging to the other surveys were covered by the catalogues of Wardlow et al. (2013), Bussmann et al. (2013, 2015), Calanog et al. (2014), and Nayyeri et al. (2016).

The goal of our *HST* observations is to observe as many candidates as possible to confirm their nature by means of the higher resolution *HST* imaging and thus increase the number of confirmed *Herschel*-selected lensing systems to allow for better statistical studies. Over the years, we have been awarded *HST* snapshot time to follow up on our targets. However, since the time granted was not enough to observe the full list of *Herschel*-selected lensing systems candidates, and because of the filler nature of the snapshot program, which only guarantees a partial completion rate, we had to prioritize those candidates with a higher probability of being lensed to maximize our success rate. This resulted in prioritizing the brightest sources at 500 μm (i.e. the higher the flux density, the higher the probability for the system to be lensed) or those having other multiwavelength data and/or redshift information. The success rate of the *HST* observations was entirely determined by the *HST* observing schedule and does not depend on the candidate properties. In the end, only a fraction (290 out of 398) of the full sample has been observed, as detailed in the following section, which is the focus of this paper. Given that this subsample represents a random collection of the entire candidate population, we limit our focus on presenting the properties of this subsample without drawing any statistical conclusion on the parent sample, which would otherwise be biased by observational constraints that were out of our control.

2.2 *HST* snapshot observations and data reduction

Our *HST* snapshot follow-up observations were carried out in three different cycles.

(i) *Proposal ID 12 488 (PI: M. Negrello) in Cycle 19.* 200 targets were proposed with $S_{500} \gtrsim 85$ mJy, that were selected from the preliminary source catalogues of HerMES (63 targets) and H-ATLAS (137 targets). At the time, the only *Herschel* data available were for four of the final five H-ATLAS fields (the three fields on the Celestial Equator named GAMA09, GAMA12, and GAMA15 and the one close to the North Galactic Pole named NGP), so the targets were spread across the Equatorial and Northern sky. The observations were carried out from 2011 October to 2013 August.

(ii) *Proposal ID 15 242 (PI: L. Marchetti), in Cycle 25.* 200 targets were proposed with $S_{500} \geq 100$ mJy from the full *Herschel* coverage, but in particular from HeLMS and HerS (Nayyeri et al. 2016) and with $S_{500} \geq 80$ mJy from the H-ATLAS SGP field near the South Galactic Pole. The sample also included some of the targets submitted for observations in the Cycle 19 proposal that had not been observed or for which the *HST* data obtained were corrupted due to issues with the *HST* tracking system. The observations were carried out from 2017 October to 2018 June.

(iii) *Proposal ID 16 015 (PI L. Marchetti) in Cycle 26.* This was a continuation of the Cycle 25 proposal. The observations were carried out from 2019 November to 2020 September.

In summary, a total of 290 candidates were observed as part of these three snapshot programmes: 173 from H-ATLAS, 60 from

HerMES, 42 from HeLMS, and 15 from HerS. Unfortunately, the data of nine systems are corrupted due to issues with the *HST* tracking system, so the final sample with available *HST* snapshot observations amount to 281 systems. All the *HST* snapshot proposals share the same observing strategy with short observations of ~ 4 or ~ 11 min on source performed with the wide-*YJ* filter *F110W* of the Wide Field Camera 3 (WFC3) IR channel (Dressel 2022). The *F110W* filter has a pivot wavelength $\lambda_p = 1153.4$ nm and a passband rectangular width of 443.0 nm, corresponding to a wavelength coverage between 883.2 and 1412.1 nm. This observing band was chosen to maximize the signal-to-noise ratio (SNR) for short exposures and efficiently cover the stellar emission from the foreground galaxy in the gravitational lensing system, usually an ETG (e.g. Auger et al. 2009). The IR channel of the WFC3 allows to read out the detector with different samplings while the exposure accumulates. The sampling strategy varies depending on the specific scientific case. Our targets were observed with the MULTIACCUM observing mode using either eight samplings with 10-s sampling intervals linearly spaced between one another (SPARS10 sampling sequence) for a total exposure time of 251.75 s, or nine samplings with 25-s sampling intervals linearly spaced between one another (SPARS25 sampling sequence) for a total exposure time of 711.74 s. Due to the filler nature of the snapshot programmes, the total exposure time was defined according to the available time slot. Each set of observations is flat-field corrected, background subtracted, cosmic-ray cleaned, distortion corrected, rotated, and drizzled. For drizzling, we use a four-point subpixel dithering pattern that results in an output pixel size of 0.064 arcsec, which is roughly half of the original pixel size. The size of the field of view (FOV) is 136 arcsec $\times$ 123 arcsec. The reduction steps are performed with the ASTRODRIZZLE package (Hoffmann et al. 2021). Additionally, we perform a first-order astrometric correction by matching the *Gaia* early Data Release 3 sources (Gaia Collaboration 2021) with their nearest *HST* counterparts.

2.3 Multiwavelength data

We use archival ALMA, SMA, and NOEMA high-resolution multiwavelength observations for 77 systems and include them in our analysis. For the ALMA data, we download the Stokes *I* continuum images from the science archive.[2] For the SMA data, we either use the reduced continuum images from Enia et al. (2018), or we download the ultraviolet (UV) tables from the science archive.,[3] and we produce the continuum images with the Common Astronomy Software Applications[4] (CASA) software. HerBS-89a is the only source for which we use NOEMA data. The details of the data reduction are available in Neri et al. (2020, but see Berta et al. 2021 for a detailed study of this galaxy). These multiwavelength observations have an angular resolution ranging from 1 to 0.03 arcsec for ALMA, 0.5 arcsec for SMA, and 0.3 arcsec for NOEMA. More details on the instrumental setup and references will be given in the source-by-source description in Section 4.3. In addition to these high-resolution observations, we search both previous literature works and the NASA/IPAC Extragalactic Database[5] for the lens candidates and/or potential lenses redshifts.

---

[2] https://almascience.eso.org/aq/?result_view = observations.
[3] https://lweb.cfa.harvard.edu/cgi-bin/sma/smaarch.pl.
[4] Available at https://casa.nrao.edu/.
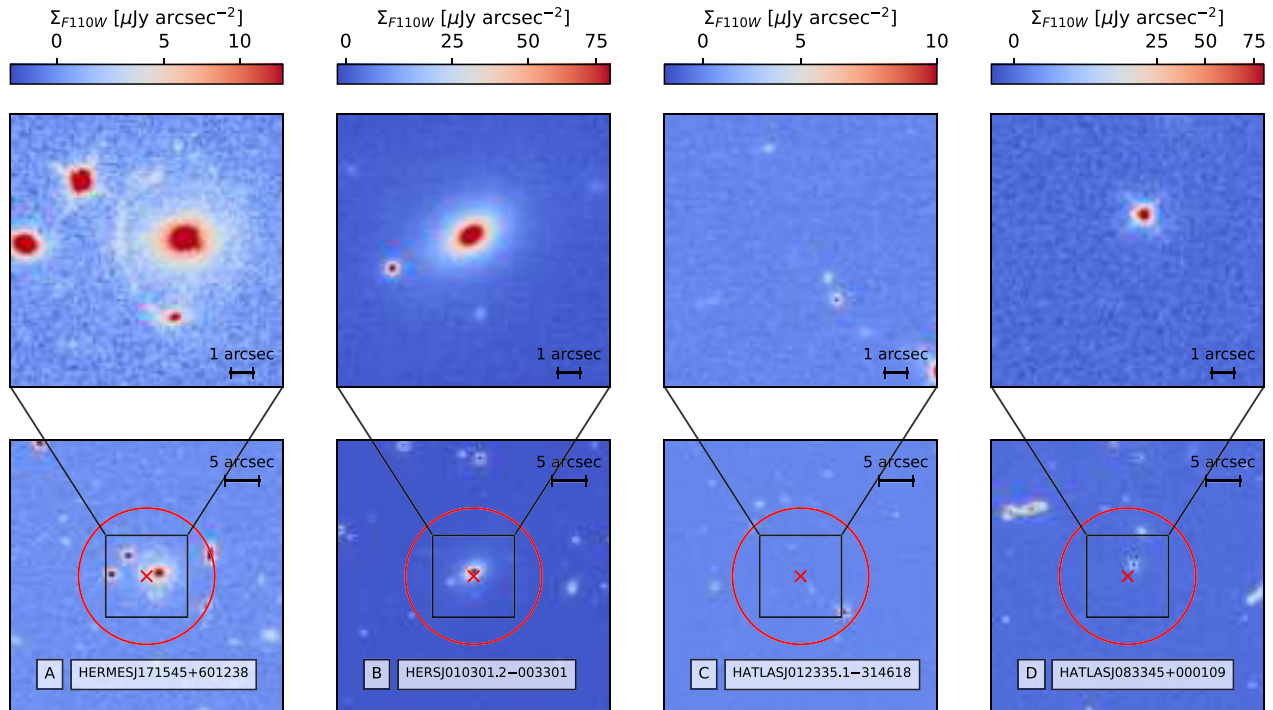[5] Available at https://ned.ipac.caltech.edu/

Figure 1. From left to right panels: examples of sample systems assigned to classes A, B, C, and D, respectively. In each column, the bottom panel shows a 20 arcsec × 20 arcsec cutout of the *HST* image, while the top panel shows a 12 arcsec × 12 arcsec zoom-in on the central source. The cross marks the position of the *Herschel* detection used to identify our targets, while the circle roughly corresponds to the ∼ 20 arcsec FWHM of the *Herschel*/SPIRE beam at 250 µm. The images are oriented with N up and E to the left.

3 LENS CLASSIFICATION

We assign each one of the 281 sources in our sample to a class that describes the likelihood of the source being a strong lensing system:

(i) *Class A:* the source is confirmed to be strongly lensed because it satisfies one or both of the following criteria: (i) the *HST* image shows a near-IR object located close to the position of the *Herschel* detection, while lensing features (such as arcs and/or multiple images) are visible either before or only after the subtraction of the near-IR source (supposedly acting as a lens), and (ii) lensing features are clearly detected in high spatial resolution sub-mm/mm ancillary data described in Section 2.3.

(ii) *Class B:* a single galaxy or a group of galaxies is visible close to the position of the *Herschel* detection, but there is no detection of lensing features even after the subtraction of the foreground galaxy. Therefore, this class tags objects that are likely to be a lens, but the background source is probably too faint to be detected in the relatively shallow *HST* data.

(iii) *Class C:* no source is detected in the *HST* image approximately within the ∼20 arcsec SPIRE FWHM at 250 µm of the position of the *Herschel* detection. These cases are likely to be either high-z unlensed DSFGs or lensing events where the lens is either at high redshift or has an intrinsically low luminosity, or both.

(iv) *Class D:* the source is a contaminant, for example, a dusty star, an unlensed quasi-stellar object (QSO), or a low redshift, sub-mm bright, and spiral galaxy (previously misinterpreted as a lens candidate).

The adopted classes are similar to those introduced by Negrello et al. (2017). The main difference is our use of the information provided by the *HST* images after the modelling and subtracting the detected near-IR source. This mainly affects the definition of class A [criterion (i)] and class B.

In order to allocate the 281 objects to the four classes, we proceed by first carrying out a visual inspection of the *HST* data alone, without performing any galaxy subtraction and without relying on any multiwavelength ancillary data. Based on this simple visual analysis, we are able to assign 25 objects to class A, 105 to class B, 146 to class C, and 5 to class D. Four examples extracted from the A, B, C, and D classes are shown in Fig. 1.

As a second step in the classification, we exploit the available high spatial resolution sub-mm/mm data to look for evidence of multiple images and arcs. In this way, we are able to identify 31 more lensed objects (promoting them to A class) that have been previously classified as B or C and 26 individual unlensed DSFGs or overdensities of unlensed DSFGs. In summary, after the use of ancillary data, the number of objects assigned to class A increases from 25 to 56 and the number of systems in classes B and C decreases to 76 and 120, respectively. In contrast, that of objects in class D increases from 5 to 29.

Finally, as described in detail in Section 4, in the *HST* images, we perform, if possible, the modelling of the surface brightness of the foreground galaxies and subtract it from the *HST* image to reveal any lensing feature. In this way, we are able to identify nine new lensed galaxies that have been previously assigned to class B.

In conclusion, after the visual inspection of the *HST* images, use of ancillary data, and surface brightness modelling, we are able to assign 65 objects to class A, 67 to class B, 120 to class C, and 29 to class D. The systems classified as A are listed in Table 1, those classified as D are listed in Table 2, while the rest of the sample is listed in Table B1. The details on the redshifts and their references are available in Table 3.

Table 1. Properties of the 65 systems classified as A by visual inspection, through multiwavelength follow-up observations, or after the lens subtraction.

No.	IAU name	Alt. name	Ref.	RA [h m s]	Dec. [d m s]	Vis. class	Multiw. obs.	Prev. classification	Ref.	S_{250} [mJy]	S_{350} [mJy]	S_{500} [mJy]	Ref.
(1)	(2)	(3)	(4)	(5)	(6)	(7)	(8)	(9)	(10)	(11)	(12)	(13)	(14)
S.1	HATLASJ000330.6 − 321136	HERBS155	Ba18	00:03:31	−32:11:36.00	A	−	−	−	59.9 ± 5.8	94.2 ± 5.8	85.6 ± 7.2	Ba18
S.2	HATLASJ000912.7 − 300807	SD.v1.70	Zh18	00:09:13	−30:08:07.00	A	−	−	−	352.8 ± 5.4	272.6 ± 6.1	156.1 ± 6.8	Ne17
S.3	HELMSJ001353.5 − 060200	HELMS31	Na16	00:13:54	−06:02:00.00	A	−	−	−	178.0 ± 7.0	176.0 ± 6.0	120.0 ± 7.0	Na16
S.4	HELMSJ003619.8 + 002420	HELMS14	Na16	00:36:20	+00:24:20.00	A	−	−	−	251.0 ± 6.0	247.0 ± 6.0	148.0 ± 7.0	Na16
S.5	HELMSJ005841.2 − 011149	HELMS23	Na16	00:58:41	−01:11:49.00	A	−	−	−	391.0 ± 7.0	273.0 ± 6.0	126.0 ± 8.0	Na16
S.6	HERSJ011722.3 + 005624	HERS10	Na16	01:17:22	+00:56:24.00	A	−	−	−	105.0 ± 6.0	125.0 ± 6.0	117.0 ± 7.0	Na16
S.7	HERSJ012620.5 + 012950	HERS5	Na16	01:26:21	+01:29:50.00	A	−	−	−	268.0 ± 8.0	228.0 ± 7.0	133.0 ± 9.0	Na16
S.8	HERSJ020941.2 + 001558	9io9 HERS1 PJ020941.3 ACT-S J0210 + 0016	Ge15 Na16 Hr16 Su17	02:09:41	+00:15:58.00	A	A	Lensed	Ge15 Hr16 Li22	826.0 ± 7.0	912.0 ± 7.0	718.0 ± 8.0	Na16
S.9	HERMESJ032637 − 270044	HECDFS05	Wa13	03:26:36	−27:00:44.00	A	−	Lensed	Ca14	155.0	131.0	84.0	Ca14
S.10	HERMESJ033732 − 295353	HECDFS02	Wa13	03:37:32	−29:53:53.00	A	−	Lensed	Wa13 Ca14	133.0	147.0	122.0	Ca14
S.11	HATLASJ083051 + 013225	G09v1.97 HERBS4	Bu13 Ba18	08:30:51	+01:32:24.87	A	A	Lensed	Bu13 Ca14 Ne17 Am18 En18 Ya19 Ma22	248.5 ± 7.5	305.3 ± 8.1	269.1 ± 8.7	Ne17
S.12	HERMESJ100144 + 025709	HCOSMOS01	Ca14	10:01:44	+02:57:08.62	A	A	Lensed	Ca14 Bu15	86.0 ± 6.0	96.0 ± 6.0	71.0 ± 6.0	Bu15
S.13	HERMESJ103827 + 581544	HLock04	Wa13	10:38:27	+58:15:43.60	A	A	Lensed	Bu13 Wa13 Ca14	190.0	156.0	101.0	Ca14
S.14	HERMESJ110016 + 571736	HLock12	Ca14	11:00:16	+57:17:35.92	A	−	Lensed	Ca14 Am18	224.0	159.0	79.0	Ca14
S.15	HATLASJ114638 − 001132	G12v2.30 HERBS2	Bu13	11:46:38	−00:11:32.00	A	A	Lensed	Bu13 Om13 Ca14 Ne17 Am18	316.0 ± 6.6	357.9 ± 7.4	291.8 ± 7.7	Ne17
S.16	HATLASJ125126 + 254928	HERBS52	Ba18	12:51:26	+25:49:28.31	A	A	−	−	57.4 ± 7.4	96.8 ± 8.2	109.4 ± 8.8	Ne17
S.17	HATLASJ125760 + 224558	−	−	12:58:00	+22:45:57.82	A	−	−	−	272.4 ± 7.3	215.0 ± 8.1	137.8 ± 8.7	Ne17
S.18	HATLASJ133008 + 245900	NBv1.78 HERBS12	Bu13 Ba18	13:30:08	+24:58:59.70	A	A	Lensed	Hs12 Bu13 Ca14 Ne17 En18	271.2 ± 7.2	278.2 ± 8.1	203.5 ± 8.5	Ne17
S.19	HATLASJ133846 + 255057	HERBS29	Ba18	13:38:46	+25:50:56.84	A	A	Lensed	Ne17 Am18	159.0 ± 7.4	183.1 ± 8.2	137.6 ± 9.0	Ne17

Table 1 – *continued*

No. (1)	IAU name (2)	Alt. name (3)	Ref. (4)	RA [h m s] (5)	Dec. [d m s] (6)	Vis. class (7)	Multiw. obs. (8)	Prev. classification (9)	Ref. (10)	S_{250} [mJy] (11)	S_{350} [mJy] (12)	S_{500} [mJy] (13)	Ref. (14)
S_20	HATLASJ142935 − 002837	G15v2.19 H1429 − 0028	Ca14 Me14	14:29:35	−00:28:37.00	A	A	Lensed	Ca14 Me14 Ne17 Am18 Dy18	801.8 ± 6.6	438.5 ± 7.5	199.8 ± 7.7	Ne17
S_21	HERMESJ171451 + 592634	HFLS02	Wa13	17:14:51	+59:26:34.12	A	−	Lensed	Ca14	164.0	148.0	87.0	Ca14
S_22	HERMESJ171545 + 601238	HFLS08	Ca14	17:15:45	+60:12:38.34	A	−	Lensed	Ca14	86.0	93.0	67.0	Ca14
S_23	HATLASJ225844.7 − 295124	HERBS26	Bal8	22:58:45	−29:51:25.00	A	−	−	−	175.4 ± 5.2	187.0 ± 5.9	142.6 ± 7.5	Ne17
S_24	HELMSJ232210.3 − 033559	HELMS19	Na16	23:22:10	−03:35:59.00	A	−	−	−	114.0 ± 6.0	160.0 ± 7.0	134.0 ± 8.0	Na16
S_25	HATLASJ233037.2 − 331217	HERBS123	Bal8	23:30:37	−33:12:18.00	A	−	−	−	106.2 ± 5.9	107.9 ± 6.0	90.0 ± 7.5	Ba18
Confirmed after the lens subtraction													
S_26	HELMSJ001626.0 + 042613	HELMS22	Na16	00:16:26	+04:26:13.00	B	A	Lensed	Am18 Dy18	130.0 ± 15.0	180.0 ± 18.0	130.0 ± 15.0	Zh18
S_27	HATLASJ002624.8 − 341737	HERBS22	Bal8	00:26:25	−34:17:38.00	B	−	−	−	137.7 ± 5.2	185.9 ± 5.8	148.8 ± 6.8	Ne17
S_28	HELMSJ004723.6 + 015751	HELMS9	Na16	00:47:24	+01:57:51.00	C	A	Lensed	Am18 Dy18	398.0 ± 6.0	320.0 ± 6.0	164.0 ± 8.0	Na16
S_29	HERSJ012041.6 − 002705	HERS2	Na16	01:20:42	−00:27:05.00	B	−	−	−	240 ± 6	260 ± 6	189 ± 7	Na16
S_30	HATLASJ085112 + 004934	−	−	08:51:12	+00:49:33.83	B	−	−	−	125.1 ± 7.3	118.3 ± 8.3	77.7 ± 8.8	Va16
S_31	HATLASJ085359 + 015537	G09v1.40	Bu13	08:53:59	+01:55:37.21	B	A	Lensed	Bu13 Ca14 Am18 En18 Bu21	396.4 ± 7.6	367.9 ± 8.2	228.2 ± 8.9	Ne17
S_32	HERMESJ104549 + 574512	HLock06	Wa13	10:45:49	+57:45:11.52	B	−	Lensed	Ca14	136.0	127.0	96.0	Ca14
S_33	HERMESJ105551 + 592845	HLock08	Wa13	10:55:51	+59:28:45.44	B	−	−	−	142.0	119.0	84.0	Ca14
S_34	HERMESJ105751 + 573026	HLSW−01 HLock01	Ga11 Wa13	10:57:51	+57:30:26.42	B	A	Lensed	Ga11 Wa13 Bu13 Ca14 Am18	402.0	377.0	249.0	Ca14
S_35	HATLASJ132630 + 334410	NAv1.195	Bu13	13:26:30	+33:44:09.90	C	A	Lensed	Bu13 Am18 En18	190.6 ± 7.3	281.4 ± 8.2	278.5 ± 9.0	Ne17

Table 1 – *continued*

No. (1)	IAU name (2)	Alt. name (3)	Ref. (4)	RA [h m s] (5)	Dec. [d m s] (6)	Vis. class (7)	Multiw. obs. (8)	Prev. classification (9)	Ref. (10)	S_{250} [mJy] (11)	S_{350} [mJy] (12)	S_{500} [mJy] (13)	Ref. (14)
S_36	HATLASJ133543 + 300404	NA.v1.489 HERBS35	Na17 Ba18	13:35:43	+30:04:03.66	B	A	Lensed	Na17	136.6 ± 7.2	145.7 ± 8.0	125.0 ± 8.5	Ne17
S_37	HATLASJ142140 + 000448	HerBS140	Ba18	14:21:40	+00:04:48.00	B	–	–	–	96.8 ± 7.2	98.5 ± 8.2	87.4 ± 8.7	Ba18
S_38	HERMESJ142824 + 352620	HBootes03	Wa13	14:28:24	+35:26:19.54	B	A	Lensed	Bo06 Bu13	323.0	243.0	139.0	Ca14
S_39	HATLASJ223753.8 − 305828	HERBS68	Ba18	22:37:54	−30:58:28.00	B	–	–	–	139.1 ± 4.9	144.9 ± 5.1	100.6 ± 6.2	Ne17
S_40	HATLASJ225250.7 − 313657	HERBS47	Ba18	22:52:51	−31:36:58.00	B	–	–	–	127.4 ± 4.2	138.7 ± 4.9	111.4 ± 5.9	Ne17
S_41	HELMSJ233441.0 − 065220	HELMS1	Na16	23:34:41	−06:52:20.00	B	A	–	–	431.0 ± 6.0	381.0 ± 7.0	272.0 ± 7.0	Na16
S_42	HELMSJ233633.5 − 032119	HELMS41	Na16	23:36:34	−03:21:19.00	B	–	–	–	130.0 ± 6.0	131.0 ± 6.0	110.0 ± 7.0	Na16
Confirmed through sub-mm/mm follow-up													
S_43	HELMSJ001615.7 + 032435	HELMS13	Na16	00:16:16	+03:24:35.00	B	A	Lensed	Am18 Dy18	176.0 ± 13.0	210.0 ± 15.0	134.0 ± 11.0	Zh18
S_44	HELMSJ002220.9 − 015524	HELMS29	Na16	00:22:21	−01:55:24.00	B	A	–	–	66.0 ± 6.0	102.0 ± 6.0	121.0 ± 7.0	Na16
S_45	HELMSJ003814.1 − 002252	HELMS24 ACT-S J0038 − 0022	Na16 Sul7	00:38:14	−00:22:52.00	C	A	–	–	73.35 ± 5.55	119.01 ± 6.01	122.87 ± 6.69	Sul7
S_46	HELMSJ003929.6 + 002426	HELMS11	Na16	00:39:30	+00:24:26.00	C	A	–	–	140.0 ± 7.0	157.0 ± 7.0	154.0 ± 8.0	Na16
S_47	HELMSJ004714.2 + 032454	HELMS8	Na16	00:47:14	+03:24:54.00	C	A	Lensed	Am18 Dy18	312.0 ± 6.0	244.0 ± 7.0	168.0 ± 8.0	Na16
S_48	HELMSJ005159.4 + 062240	HELMS18	Na16	00:52:00	+06:22:41.00	B	A	Lensed	Am18 En18 Ma22	163.0 ± 13.0	202.0 ± 15.0	142.0 ± 12.0	Zh18
S_49	HATLASJ005724.2 − 273122	HERBS60	Ba18	00:57:24	−27:31:22.00	B	A	–	–	73.3 ± 5.8	101.2 ± 6.1	103.6 ± 7.5	Ba18
S_50	HERMESJ021831 − 053131	SXDF1100.001 (Orochi) HXMM02	Ik11 Wa13	02:18:31	−05:31:31.00	B	A	Lensed	Bu13 Bu15	78.0 ± 7.0	122.0 ± 8.0	99.0 ± 7.0	Bu15
S_51	HERMESJ033211 − 270536	HECDFS04	Wa13	03:32:11	−27:05:36.00	C	A	Lensed	Bu15	56.0 ± 6.0	61.0 ± 6.0	55.0 ± 6.0	Bu15
S_52	HERMESJ044154 − 540352	HADFS01	Wa13	04:41:54	−54:03:52.00	B	A	Lensed	Bu15	76.0 ± 6.0	100.0 ± 6.0	94.0 ± 6.0	Bu15
S_53	HATLASJ083932 − 011760	HERBS105	Ba18	08:39:32	−01:18:00.00	C	A	–	–	73.8 ± 7.4	88.5 ± 8.1	93.2 ± 8.7	Ba18
S_54	HATLASJ091841 + 023048	G09v1.326 HERBS32	Ca14 Ba18	09:18:41	+02:30:47.97	B	A	–	–	125.7 ± 7.2	150.7 ± 8.2	128.4 ± 8.7	Ne17
S_55	HATLASJ113526 − 014606	G12v2.43 HERBS10	Bu13 Ba18	11:35:26	−01:46:06.00	C	A	Lensed	Gi23	278.8 ± 7.4	282.9 ± 8.2	204.0 ± 8.6	Ne17

Table 1 – *continued*

No.	IAU name	Alt. name	Ref.	RA [h m s]	Dec. [d m s]	Vis. class	Multiw. obs.	Prev. classification	Ref.	S_{250} [mJy]	S_{350} [mJy]	S_{500} [mJy]	Ref.
(1)	(2)	(3)	(4)	(5)	(6)	(7)	(8)	(9)	(10)	(11)	(12)	(13)	(14)
S_56	HATLASJ115433.6 + 005042	HERBS177	Ba18	11:54:34	+00:50:42.30	B	A	–	–	53.9 ± 7.4	85.8 ± 8.1	83.9 ± 8.6	Ba18
S_57	HATLASJ120127.6 − 014043	HERBS61	Ba18	12:01:28	−01:40:44.00	B	A	Lensed	En18	67.4 ± 6.5	112.1 ± 7.4	103.9 ± 7.7	Ne17
S_58	HATLASJ131611 + 281220	HERBS89	Ba18	13:16:11	+28:12:20.39	C	A	Lensed	Be21	71.8 ± 5.7	103.4 ± 5.7	95.7 ± 7.0	Ba18
S_59	HATLASJ134429 + 303036	NAv1.56 HERBS1	Bu13 Ba18	13:44:29	+30:30:35.77	B	A	Lensed	Bu13 Fa17 Am18 En18	462.0 ± 7.4	465.7 ± 8.6	343.3 ± 8.7	Ne17
S_60	HATLASJ141352 − 000027	G15v2.235 HERBS15	Bu13 Ba18	14:13:52	−00:00:27.00	B	A	Lensed	Bu13 Am18	188.6 ± 7.4	217.0 ± 8.1	176.4 ± 8.7	Ne17
S_61	HATLASJ142414 + 022304	ID 141 G15v2.779 HERBS13	Co11 Bu13 Ba18	14:24:14	+02:23:03.62	B	A	Lensed	Co11 Bu12 Dy18 En18 Dy22	112.2 ± 7.3	182.2 ± 8.2	193.3 ± 8.5	Ne17
S_62	HERMESJ142826 + 345547	HBootes02	Wa13	14:28:26	+34:55:47.03	B	A	Lensed	Wa13 Bu13 Ca14	159.0	195.0	156.0	Ca14
S_63	HATLASJ230815.5 − 343801	HERBS28	Ba18	23:08:16	−34:38:01.00	B	A	–	–	79.4 ± 5.4	135.4 ± 5.7	140.0 ± 7.0	Ne17
S_64	HELMSJ232439.5 − 043936	HELMS7	Na16	23:24:40	−04:39:36.00	B	A	Lensed	Am18 Ma22	214.0 ± 7.0	218.0 ± 7.0	172.0 ± 9.0	Na16
S_65	HELMSJ233620.8 − 060828	HELMS6	Na16	23:36:21	−06:08:28.00	B	A	–	–	193.0 ± 7.0	252.0 ± 6.0	202.0 ± 8.0	Na16

Notes. Column (1): source reference number. Column (2): IAU name of the *Herschel* detection. Columns (3) and (4): alternative name and reference. Columns (5) and (6): ICRS RA and Dec. coordinate (J2000.0) of the *Herschel* detection. Column (7): classification after the visual inspection [criterium (i)]. Column (8): lens classification including the multiwavelength observations. Columns (9) and (10): confirmed lensed system and reference. Columns (11)–(14): SPIRE flux density at 250, 350, and 500 μm, and reference. Following are the abbreviations used for the references: A117: Albareti et al. (2017); Am18: Amvrosiadis et al. (2018); Ba18: Bakx et al. (2018); Be21: Berta et al. (2021); Bo06: Borys et al. (2006); Bu13: Bussmann et al. (2013); Bu15: Bussmann et al. (2015); Bu21: Butler et al. (2021); Cal4: Calanog et al. (2014); Co11: Cox et al. (2011); Dy18: Dye et al. (2018); Dy22: Dye et al. (2022); En18: Enia et al. (2018); Fa17: Falgarone et al. (2017); Ga11: Gavazzi et al. (2011); Ge15: Geach et al. (2015); Gi23: Giulietti et al. (2023); Hs12: Harris et al. (2012); Hr16: Harrington et al. (2016); Ik11: Ikarashi et al. (2011); Ma19: Ma et al. (2019); Ma22: Maresca et al. (2022); Me14: Messias et al. (2014); Na16: Nayyeri et al. (2016); Na17: Nayyeri et al. (2017); Ne17: Negrello et al. (2017); Om13: Omont et al. (2013); Su17: Su et al. (2017); Sh21: Shirley et al. (2021); Ur22: Urquhart et al. (2022); Va16: Valiante et al. (2016); Wa13: Wardlow et al. (2013); Ya17: Yang et al. (2017); and Ya19: Yang et al. (2019).

Table 2. Properties of the 26 systems confirmed to be unlensed by multiwavelength follow-up.

No. (1)	Name (2)	Alt. name (3)	Ref. (4)	RA [h m s] (5)	Dec. [d m s] (6)	Multiw. (7)	Ref. (8)	Nature (9)	Ref. (10)	HST counterpart (11)	z (12)	Ref. (13)
S.72	HERMESJ003824 − 433705	HELAISS02	Cal4	00:38:24	−43:37:05.00	ALMA band 7	Bu13	Multiple	–	Yes	–	–
S.86	HERMESJ022022 − 015329	HXMM04	Wa13	02:20:22	−01:53:29.00	ALMA band 7	Bu15	Single	Bu15	Yes	(0.21 ± 0.14)	Wa13
S.87	HERMESJ022029 − 064846	HXMM09	Wa13	02:20:29	−06:48:46.00	ALMA band 7	Bu15	Multiple/merger	Bu15	No	(0.21 ± 0.09)	Wa13
S.89	HERMESJ022548 − 041750	HXMM05	Wa13	02:25:48	−04:17:50.00	ALMA band 7, 8 / SMA at 340 GHz	Le19 / Bu13	Single DSFG	Le19	No	2.985	Wa13
S.90	HERMESJ045027 − 524126	HADFS08	Cal4	04:50:27	−52:41:26.00	ALMA band 7	Bu15	Merger	–	Yes	–	–
S.92	HATLASJ084933 + 021443	HerBS8	Cal4	08:49:33	+02:14:43.14	ALMA band 3 / ALMA band 4, 6, 7 / SMA at 340 GHz	2018.1.01146.S / Iv13 / Iv13	Protocluster	Iv13	Yes	2.41	Bu13
S.119	HATLASJ222503.7 − 304847	HerBS166	Ba18	22:25:04	−30:48:48.00	ALMA band 7	Ma19	Multiple	–	Yes	(4.52 ± 0.62)	Ba18
S.140	HATLASJ000455.3 − 330811	HerBS170	Ba18	00:04:55	−33:08:12.00	ALMA band 6	2018.1.00526.S	Multiple	–	No	(4.24 ± 0.58)	Ba18
S.151	HELMSJ005258.6 + 061319	HELMS10	Na16	00:52:59	+06:13:19.00	ALMA band 7	2013.1.00749.S	Multiple	–	Yes	(3.2 ± 0.2)	Le18
S.156	HATLASJ012335.1 − 314618	HerBS145	Ba18	01:23:35	−31:46:19.00	ALMA band 6	2018.1.00526.S	Single/QSO	–	Yes	2.73	Ur22
S.164	HERMESJ021943 − 052433	HXMM20	Cal4	02:19:43	−05:24:33.00	ALMA band 7	GG19	Protocluster	GG19	Yes	2.602	GG19
S.165	HERMESJ022206 − 070727	HXMM23	Cal4	02:22:06	−07:07:27.00	ALMA band 7	Bu15	Single	Bu15	Yes	–	–
S.167	HERMESJ022251 − 032414	HXMM22	Cal4	02:22:51	−03:24:14.00	ALMA band 7	Bu15	Single	Bu15	No	–	–
S.176	HERMESJ043830 − 541832	HADFS02	Cal4	04:38:30	−54:18:32.00	ALMA band 7	Bu15	Multiple/merger	Bu15	Yes	(3.40 ± 0.70)	Ag18
S.177	HERMESJ044947 − 525427	HADFS09	Cal4	04:49:47	−52:54:27.00	ALMA band 7	Bu15	Multiple	Bu15	Yes	–	–
S.178	HATLASJ083153 + 014014	–	–	08:31:53	+01:40:14.43	ALMA band 3 / ALMA band 5 / ALMA band 8	Pe20 / 2019.2.00027.S / DS21	Quasar	DS21	Yes	3.9136	DS21
S.188	HATLASJ091454 − 010357	HerBS142	Ba18	09:14:54	−01:03:57.00	ALMA band 6	2018.1.00526.S	Multiple/merger	Bu15	Yes	(3.22 ± 0.44)	Ba18
S.193	HERMESJ100057 + 022014	HCOSMOS02	Cal4	10:00:57	+02:20:13.70	ALMA band 3 / ALMA band 4 / ALMA band 6 / ALMA band 6 / ALMA band 7 / ALMA band 7	Wa18, Ch21 / 2019.1.00151.S / 2013.1.00118.S / Ch21 / 2016.1.00463.S / 2016.1.00478.S	Protocluster	GG19	Yes	2.497	Cal4
S.201	HATLASJ115521 − 021332	HERBS179	Ba18	11:55:21	−02:13:32.00	ALMA band 6	2018.1.00526.S	Single	–	Yes	(4.07 ± 0.56)	Ba18
S.207	HATLASJ121812.8 + 011841	HerBS83	Ba18	12:18:13	+01:18:41.67	ALMA band 6	2018.1.00526.S	Multiple	–	No	*	Co23
S.211	HATLASJ122407.4 − 003247	HerBS161	Ba18	12:24:07	−00:32:47.00	ALMA band 6	2018.1.00526.S	Multiple	–	Yes	(3.82 ± 0.52)	Ba18
S.212	HATLASJ122459.1 − 005647	HerBS150	Ba18	12:24:59	−00:56:47.00	ALMA band 6	2018.1.00526.S	Multiple	–	Yes	(4.57 ± 0.63)	Ba18
S.240	HATLASJ141118 − 010655	HerBS201	Ba18	14:11:18	−01:06:55.00	ALMA band 6	2018.1.00526.S	Multiple	–	No	(4.00 ± 0.55)	Ba18
S.271	HATLASJ232200.0 − 355622	HerBS118	Ba18	23:22:00	−35:56:22.00	ALMA band 6	2018.1.00526.S	Single	–	Yes	(3.80 ± 0.52)	Ba18
S.278	HATLASJ083345 + 000109	HerBS88	Ba18	08:33:45	+00:01:09.41	ALMA band 7	2013.1.00358.S	Single/QSO	–	Yes	2.530596	Al17
S.279	HATLASJ090613.8 − 010042	HerBS165	Ba18	09:06:14	−01:00:43.00	ALMA band 6	2018.1.00526.S	Single/QSO	–	Yes	*	Co23

Notes. Column (1): source reference number. The candidates are ordered first by their lens classification and then by their RA. Column (2): IAU name of the *Herschel* detection. Columns (3) and (4): alternative name and reference. Columns (5) and (6): ICRS RA and Dec. coordinate (J2000.0) of the *Herschel* detection. Columns (7) and (8): multiwavelength observations and reference. Columns (9) and (10): possible nature of the system and reference. Column (11): presence of near-IR counterparts. Columns (12) and (13): redshift of the source and reference. Following are the abbreviations used for the references that are not already included in Tables 1 and 3: Ag18: Aguirre et al. (2018); Ch21: Champagne et al. (2021); DS21: Díaz-Santos et al. (2021); GG19: Gómez-Guijarro et al. (2019); Iv13: Ivison et al. (2013); Le18: Lewis et al. (2018); Le19: Leung et al. (2019); Pe20: Penney et al. (2020); and Wa18: Wang et al. (2018).

Table 3. Redshift of the candidate lenses and background sources of the confirmed lensing systems.

No.	Name	z_l	Ref.	z_s	Ref.
(1)	(2)	(3)	(4)	(5)	(6)
S_1	HATLASJ000330.6 − 321136	(0.38 ± 0.10)	Sh21	3.077	Ur22
S_2	HATLASJ000912.7 − 300807	(0.28 ± 0.08)	Sh21	(1.19 ± 0.10)	Zh18
S_3	HELMSJ001353.5 − 060200	(0.60 ± 0.18)	Na16	1.948	Co23
S_4	HELMSJ003619.8 + 002420	0.257573	Na16	1.617	Co23
S_5	HELMSJ005841.2 − 011149	(0.38 ± 0.08)	Na16	1.498	Co23
S_6	HERSJ011722.3 + 005624	(0.87 ± 0.05)	Na16	2.469	Co23
S_7	HERSJ012620.5 + 012950	(0.43 ± 0.05)	Na16	1.449	Co23
S_8	HERSJ020941.2 + 001558	0.201854	Na16	2.55293	Ge15
S_9	HERMESJ032637 − 270044	–	–	–	–
S_10	HERMESJ033732 − 295353	(0.19 ± 0.05)	Sh21	–	–
S_11$_1$	HATLASJ083051 + 013225$_1$	0.626	Bu13	3.6345	Ya17
S_11$_2$	HATLASJ083051 + 013225$_2$	1.002	Bu13	3.6345	Ya17
S_12	HERMESJ100144 + 025709	0.608	Ca14	–	–
S_13	HERMESJ103827 + 581544	0.591465	Al17	–	–
S_14	HERMESJ110016 + 571736	0.780518	Al17	–	–
S_15	HATLASJ114638 − 001132	1.2247	Bu13	3.2596	Y17
S_16	HATLASJ125126 + 254928	(0.62 ± 0.10)	Ne17	3.4419	Ba20
S_17	HATLASJ125760 + 224558	0.555449	Al17	(1.53 ± 0.30)	Ne17
S_18	HATLASJ133008 + 245860	0.4276	Bu13	3.112	Ca14
S_19	HATLASJ133846 + 255057	(0.42 ± 0.10)	Ne17	(2.34 ± 0.40)	Ba18
S_20	HATLASJ142935 − 002837	0.21844	Me14	1.0271	Me14
S_21	HERMESJ171451 + 592634	1.236	Sh21	3.17844	HC16
S_22	HERMESJ171545 + 601238	(0.40 ± 0.09)	Sh21	2.264	Ca14
S_23	HATLASJ225844.7 − 295124	(0.69 ± 0.21)	Sh21	(2.48 ± 0.040)	Ba18
S_24	HELMSJ232210.3 − 033559	(0.14 ± 0.09)	Na16	4.688	Co23
S_25$_1$	HATLASJ233037.2 − 331217$_1$	(0.66 ± 0.17)	Sh21	2.170	Ur22
S_25$_2$	HATLASJ233037.2 − 331217$_2$	(0.66 ± 0.17)	Sh21	2.170	Ur22
S_26	HELMSJ001626.0 + 042613	0.2154	Am18	2.509	Na16
S_27	HATLASJ002624.8 − 341737	(0.93 ± 0.35)	Wa22	3.050	Ur22
S_28	HELMSJ004723.6 + 015751	0.3650	Am18	1.441	Na16
S_29	HERSJ012041.6 − 002705	(0.73 ± 0.04)	Na16	2.015	Co23
S_30	HATLASJ085112 + 004934	(0.66 ± 0.32)	Sh21	(1.77 ± 0.27)	MG19
S_31	HATLASJ085359 + 015537	(1.16 ± 0.22)	Sh21	2.0925	Ya16
S_32	HERMESJ104549 + 574512	(0.20 ± 0.02)	Wa13	2.991	Wa13
S_33	HERMESJ105551 + 592845	(0.38 ± 0.11)	Wa13	1.699[a]	Wa13
S_34	HERMESJ105751 + 573026	(0.60 ± 0.04)	Ga11	2.9575	Ga11
S_35	HATLASJ132630 + 334410	0.7856	Bu13	2.951	Bu13
S_36$_1$	HATLASJ133543 + 300404$_1$	0.9825	St14	2.685	Ca14
S_36$_2$	HATLASJ133543 + 300404$_2$	0.9845	St14	2.685	Ca14
S_36$_3$	HATLASJ133543 + 300404$_3$	0.9815	St14	2.685	Ca14
S_36$_4$	HATLASJ133543 + 300404$_4$	0.9945	St14	2.685	Ca14
S_37	HATLASJ142140 + 000448	(1.11 ± 0.41)	Sh21	2.781	Co23
S_38	HERMESJ142824 + 352620	1.034	Bo06	1.325	Bo06
S_39	HATLASJ223753.8 − 305828	(0.54 ± 0.14)	Sh21	(2.13 ± 0.38)	Wa22
S_40	HATLASJ225250.7 − 313657	(0.69 ± 0.26)	Sh21	2.433	Ur22
S_41	HELMSJ233441.0 − 065220	–	–	1.905	Co23
S_42	HELMSJ233633.5 − 032119	–	–	2.335	Co23
S_43	HELMSJ001615.7 + 032435	0.663	Na16	2.765	Na16
S_44	HELMSJ002220.9 − 015524	(0.90 ± 0.15)	Sh21	5.162	As16
S_45	HELMSJ003814.1 − 002252	(0.17 ± 0.08)	Na16	4.984	Co23
S_46	HELMSJ003929.6 + 002426	(0.72 ± 0.23)	Sh21	2.848	Co23
S_47	HELMSJ004714.2 + 032454	(0.48 ± 0.08)	Na16	1.19	Na16
S_48$_1$	HELMSJ005159.4 + 062240$_1$	0.60266	Ok21	2.392	Na16
S_48$_3$	HELMSJ005159.4 + 062240$_3$	0.59852	Ok21	2.392	Na16
S_49	HATLASJ005724.2 − 273122	(0.89 ± 0.41)	Wa22	3.261	Ur22
S_50	HERMESJ021831 − 053131	1.350	Wa13	3.3950	Wa13
S_51	HERMESJ033211 − 270536	–	–	–	–
S_52	HERMESJ044154 − 540352	–	–	–	–
S_53	HATLASJ083932 − 011760	(0.42 ± 0.12)	Sh21	2.669	Co23
S_54$_1$	HATLASJ091841 + 023048$_1$	(0.91 ± 0.32)	Sh21	2.5811	Ha12
S_54$_2$	HATLASJ091841 + 023048$_2$	(0.91 ± 0.32)	Sh21	2.5811	Ha12
S_55	HATLASJ113526 − 014606	–	–	3.1276	Ha12
S_56	HATLASJ115433.6 + 005042	(0.52 ± 0.11)	Sh21	(3.90 ± 0.50)	Ba20

Table 3 – *continued*

No.	Name	z_l	Ref.	z_s	Ref.
(1)	(2)	(3)	(4)	(5)	(6)
S_57	HATLASJ120127.6 − 014043	(0.88 ± 0.35)	Sh21	(4.06 ± 0.38)	MG19
S_58	HATLASJ131611 + 281220	(0.90 ± 0.13)	Be21	2.9497	Ne20
S_59	HATLASJ134429 + 303036	0.6721	Bu13	2.3010	Ha12
S_60$_1$	HATLASJ141352 − 000027$_1$	0.5478	Bu13	2.4782	Ha12
S_60$_3$	HATLASJ141352 − 000027$_3$	0.5494	Bu13	2.4782	Ha12
S_61$_1$	HATLASJ142414 + 022304$_1$	0.595	Bu13	4.243	Co11
S_61$_2$	HATLASJ142414 + 022304$_2$	0.595	Bu13	4.243	Co11
S_62	HERMESJ142826 + 345547	0.414	Wa13	2.804	Wa13
S_63	HATLASJ230815.5 − 343801	(0.72 ± 0.21)	Wa22	(4.03 ± 0.38)	MG19
S_64	HELMSJ232439.5 − 043936	(0.67 ± 0.26)	Sh21	2.473	Na16
S_65	HELMSJ233620.8 − 060828	0.3958	Na16	3.434	Na16

Notes. Column (1): source reference number. Column (2): IAU name of the *Herschel* detection. Columns (3) and (4): redshift of the lens candidate and reference. Columns (5) and (6): redshift of the background source and reference. The bracketed values are photometric redshifts. Following are the abbreviations used for the references that are not already included in Table 1: As16: Asboth et al. (2016); Ba20: Bakx et al. (2020); Co23: Cox et al. (2023); HC16: Hernán-Caballero et al. (2016); MG19: Manjón-García et al. (2019); Ne20: Neri et al. (2020); Ok21: Okido et al. (2021); St14: Stanford et al. (2014); Wa22: Ward et al. (2022); and Ya16: Yang et al. (2016).

4 SURFACE BRIGHTNESS MODELLING

We group all the systems, for which we are able to identify the foreground lensing galaxies or a suitable candidate according to the following configurations:

(i) systems in which a clearly isolated galaxy is acting as a lens. In this case, we model this single object (type 1);

(ii) systems in which two or three galaxies are probably acting as lenses (e.g. they are very close to each other or even blended, and the lensing features are consistent with multiple lenses). In this case, we model all the galaxies at the same time (type 2);

(iii) systems in which more than one galaxy is clearly visible in the foreground, but either they are sufficiently small or distant with respect to each other that they can be separately modelled (type 3);

(iv) one system which shows no trace of a lens, likely due to a combination of high redshift and obscuration (HAT-LASJ113526 − 014606; see Giulietti et al. 2023 for details). This system will not be included in the lens surface brightness modelling.

For the systems confirmed as lensed by multiwavelength data alone, we use the location of the background sources sub-mm emission to identify the foreground lensing galaxies in the *HST* observations.

It is worth noticing that for types 2 and 3 systems, we can not be sure whether all the galaxies are contributing to the lensing. In most cases, we do not know the redshift of all the galaxies, so we can not rule out the possibility that they are unrelated field objects.

We still provide the models of all the galaxies of interest to enable future studies once all the redshifts are known. In order to best characterize the galaxies acting as lenses and provide the best-fitting model of their surface brightness, we use either a parametric or a non-parametric approach depending on the lens morphology and configuration of the lensing system.

For the parametric modelling, we adopt the Galaxy Surface Photometry 2-Dimensional Decomposition algorithm (GASP2D; Méndez-Abreu et al. 2008, 2017) to model the type 1 and type 3 lensing systems and the Galaxy Fitting algorithm (GALFIT; Peng et al. 2002, 2010) for the type 2 foreground lensing systems. GASP2D has the advantage of automatically setting the initial guess values needed to fit the galaxy image, whereas GALFIT allows us to perform the simultaneous fit of multiple systems. We adopt the non-parametric

Isophote Fitting algorithm (ISOFIT; Ciambur 2015) to model highly inclined disc lenses for which GASP2D and GALFIT fail. In the following sections, we describe the approaches adopted for the different cases. We point out in the source-by-source descriptions the cases for which we made exceptions to the above prescriptions.

4.1 Parametric approaches

Both GASP2D and GALFIT adopt a set of analytical functions to model the light distribution of the galaxy components. They derive the best-fitting values of the structural parameters by comparing the model of the surface brightness distribution with the observed photon counts of the galaxy in each image pixel with an iterative procedure of non-linear least-squares minimization. The model surface brightness is convolved with the point spread function (PSF) measured on the galaxy image to deal with the smearing effects due to the telescope optics and instrumental setup. Each image pixel is weighted according to the inverse of the variance of its total photon counts due to the contribution of both the galaxy and sky, the detector photon-noise limitation and readout noise are also taken into account. GASP2D and GALFIT are written in IDL[6] and C,[7] respectively. They provide the best-fitting values of the structural parameters of the galaxy components and their formal errors, as well as the model and residual image of the galaxy to be compared to the observed one.

4.1.1 Residual sky subtraction

The sky level provided by the image reduction consists of a global estimate across the FOV after automatically masking the luminous sources. This subtraction proves to be unreliable in the analysis of the faintest lensing features since a residual sky level could still be present in the image. Therefore, we measure and subtract the residual sky level as follows.

We start by masking the system as well as the foreground stars, companion, and background galaxies, and lensing features using the MAKE_SOURCES_MASK task of the PHOTUTILS.BACKGROUND PYTHON

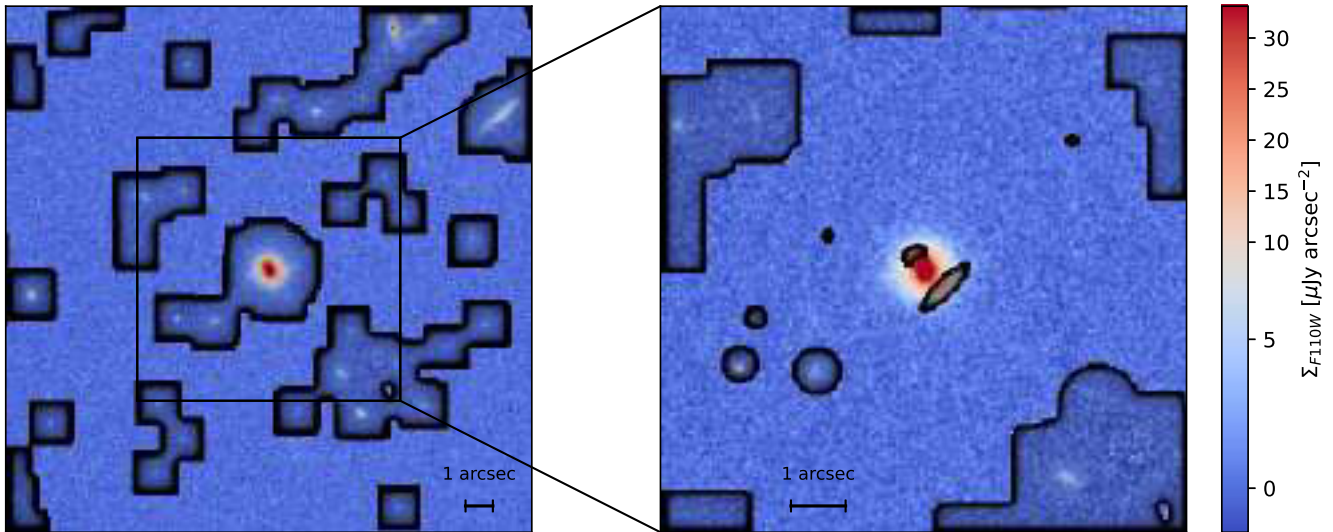
[6] https://www.l3harrisgeospatial.com/Software-Technology/IDL
[7] https://users.obs.carnegiescience.edu/peng/work/galfit/galfit.html

Figure 2. Left panel: image of S_7 with the pixel mask (corresponding to the regions with black contours) used to estimate the residual sky level and standard deviation of the background. The highlighted box marks the FOV of the zoom-in shown in the right panel. Right panel: trimmed sky-subtracted image and pixel mask used to fit the surface brightness distribution of the lensing galaxy of S_7.

package[8] (Bradley et al. 2021). The source segmentation algorithm identifies all the above sources and creates their footprints by selecting the N_{pixel} connected pixels with photon counts over a given threshold σ. Then, the algorithm enlarges the available footprints with binary dilation (e.g. Nadadur & Haralick 2000) through an m pixel $\times$ m pixel matrix to build the pixel mask of all the luminous sources in the image. We repeat this process twice to identify both the compact ($N_{pixel} = 5$, $m = 11$, and $\sigma = 2$) and extended ($N_{pixel} = 10$, $m = 51$, and $\sigma = 2$) sources. In both cases, we reiterate the source identification and footprint dilation of the masked image until no more pixels are added to the mask. The values of N_{pixel}, m, and σ are chosen such that the resulting masks cover most of the sources and, at the same time, leave some background-dominated regions in the image. The final pixel mask is the combination of the footprints built for compact and extended sources, which we visually check and manually edit to remove the spurious sources, such as residual cosmic rays and bad pixels.

We calculate the residual sky level as the biweight location of the unmasked pixels. This is an estimator for the central location of a distribution that is very robust against outliers (e.g. Beers, Flynn & Gebhardt 1990). Then, we subtract it from the image. We derive the standard deviation rms_{bkg} of the sky-subtracted image through the median absolute deviation of the unmasked pixels using $\sigma = MAD/\Phi^{-1}(3/4)$, where MAD is the median absolute deviation, $1/\Phi^{-1}(3/4) \approx 1.4826$ is the normal inverse cumulative distribution function evaluated at a probability of 3/4. The biweight location and MAD are available through ASTROPY.STATS package (Astropy Collaboration 2018). The image of HERSJ012620.5 + 012950 (HERS5, S_7; Nayyeri et al. 2016) with the pixel mask adopted to estimate the residual sky level is shown in Fig. 2 (left panel) as an example.

4.1.2 Pixel mask and noise map

We trim the sky-subtracted images to reduce the computing time to perform a reliable photometric decomposition. Each galaxy is centred

in an FOV ranging from 200 pixel $\times$ 200 pixel (corresponding to 12.8 arcsec $\times$ 12.8 arcsec) to 400 pixel $\times$ 400 pixel (25.6 arcsec $\times$ 25.6 arcsec) to fully cover all the lensing features. We also trim the pixel mask to the same region. Then, we unmask the pixels corresponding to the source in the central circular region of ~100-pixel (6.4 arcsec) radius. This allows us to set up the final pixel mask, which we use for the parametric fitting of the source surface brightness. The trimmed image and final pixel mask that we use to model the surface brightness distribution of S_7 are shown in Fig. 2 (right panel). In addition, we build the noise map of the images by calculating the variance (in units of electrons) of each pixel as $\sigma^2 = (RON^2 + \sigma_{sky}^2 + \sigma_{gal}^2)/GAIN^2$, where $\sigma_{sky}^2 = I_{sky} \cdot GAIN$ and $\sigma_{gal}^2 = I_{gal} \cdot GAIN$ with I_{sky} and I_{gal} the surface brightness of the sky and lens in ADU, RON is the detector readout noise (in ADU) scaled for the number of samplings performed during the exposure (see Dressel 2022 for details), and GAIN is the detector gain (in e$^-$ ADU^{-1}). Since the sky level that was actually subtracted during image reduction is not readily available, we use $rms_{bkg}^2 = RON^2 + \sigma_{sky}^2$. Nevertheless, we estimate the expected variance of the sky from the equation above, verifying that $\sigma_{sky} > RON$.

4.1.3 PSF model

For each image, we build a PSF model from the non-saturated point sources with the highest SNR available in the full *WFC3/F110W* FOV. For each point source, we identify the centroid with the FIND_CENTROIDS task of the PHOTUTILS package and we extract a cutout of 100 pixel $\times$ 100 pixel (6.4 arcsec $\times$ 6.4 arcsec) corresponding to $\sim$ 20 FWHM $\times$ 20 FWHM. We get the stacked PSF by summing all the point-source cutouts. Before stacking, we normalize the total flux of each point source to unity after removing spurious sources and surface brightness gradient due to nearby bright and extended sources. The stacked PSF is smoothed using a PYTHON two-dimensional Savitsky–Golay filter[9] (e.g. Ratzlaff & Johnson 1989) to remove noise. Then, we mask the smoothed PSF model using image segmentation and replace the background pixels with their mean
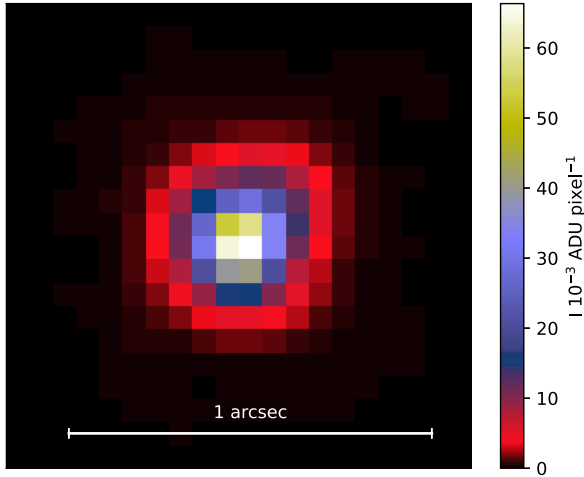
---

[8]https://photutils.readthedocs.io/en/stable/index.html

[9]https://github.com/espdev/sgolay2

Figure 3. Image of the normalized PSF model adopted to fit the surface brightness distribution of S_7.

value. We adopt the resulting stacked, smoothed, and background-subtracted PSF to model the surface brightness distribution of the source. The average number of point sources we use to build the PSFs is 2. We show in Fig. 3 the PSF model adopted for the parametric fit of S_7.

4.1.4 Parametric modelling

We perform the parametric modelling of the systems following the steps reported in the flowchart given in Fig. 4 and taking into account the PSF model, pixel mask, and noise map associated with the image.

Both GASP2D and GALFIT algorithms are based on a χ^2 minimization. Thus, it is important to adopt initial guesses for the free parameters as close as possible to their actual values. This ensures that the iteration procedure does not stop on a local minimum of the χ^2 distribution. GASP2D automatically sets the guess values by performing a one-dimensional decomposition of the azimuthally averaged radial profiles of the surface brightness, ellipticity, and position angle of the source, which we measured by fitting ellipses to the isophotes with the ISOFIT task (see Section 4.2 for details) and adopting the final pixel mask. For GALFIT, we preliminarily fit a de Vaucouleurs law and adopt for the ellipticity and position angle of the mean values of the azimuthally averaged radial profiles. The best-fitting values of this preliminary decomposition are adopted as guess values for the actual parametric fitting of the source.

We always start by fitting a single Sérsic component to the source. Then, we visually inspect the residual image to look for spurious sources and/or lensing features. We update the pixel mask to account for them and repeat the fit. If significant residuals are still visible, we add a second component and repeat again the fit. We check the new residual image and iterate the fitting procedure up to a maximum of three Sérsic extended components and one unresolved nuclear component. The additional luminous components are included to remove the residual under/oversubtracted structures at scales similar to the PSF or larger. As a final step, we double-check the best-fitting values to avoid hitting the boundaries of the allowed ranges for the structural parameters, for which we adopt the ones implemented in GASP2D, which are [0.3, 10] for the Sérsic index and [0.5 FWHM$_{PSF}$, $+\infty$) for the effective radius
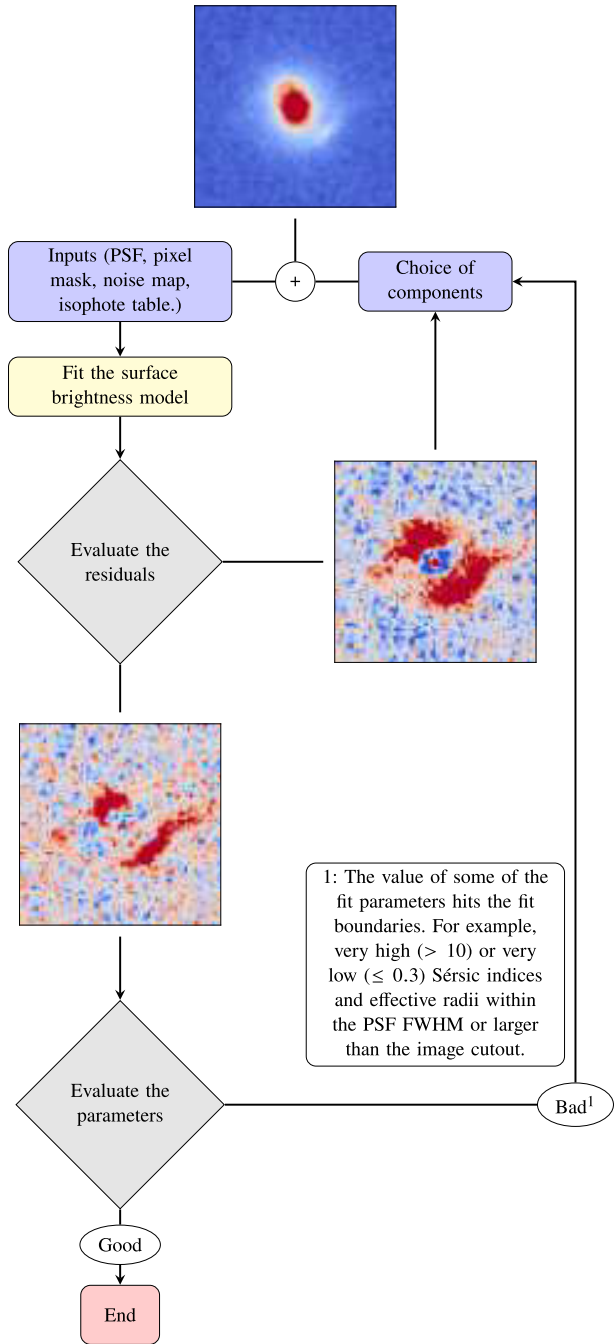

Figure 4. Flowchart describing the steps of the parametric surface brightness modelling.

(see, Méndez-Abreu et al. 2008, 2017, for details). This issue occurs mostly for the Sérsic index of a few luminous components, which we fix to 0.5, 1, or 4. If the best-fitting effective radius of the single Sérsic fit is smaller than the PSF FWHM or larger than the cutout radius, we add a nuclear point source or enlarge the cutout. When necessary, we mask out the dust patches and lanes as much as possible to recover a reliable model of the surface brightness distribution.

The input files adopted by the two algorithms to perform surface brightness modelling are listed in Table 4.

Table 4. Input files adopted to perform the surface brightness modelling with the different fitting algorithms used in this work.

Algorithm	Noise map	PSF model	Isophote table	Parametric functions	Parameter guesses	Pixel mask
GASP2D	Yes	Yes	Yes	Yes	Optional	Yes
GALFIT	Yes	Yes	No	Yes	Yes	Yes
ISOFIT + CMODEL	No	No	Yes	No	No	Yes

4.1.5 Error estimate

The formal errors on the fitted parameters obtained from the χ^2 minimization procedure usually underestimate the real errors of the structural parameters (e.g. Méndez-Abreu et al. 2008). Therefore, we estimate the errors on the fitted parameters by analysing a sample of mock galaxies we build through a series of Monte Carlo (MC) simulations following Dalla Bontà et al. (2018).

To mimic the observational setup, we carry out the MC simulations in two different exposure-time bins, corresponding to 251 and 712 s, respectively. For each modelled galaxy (Table 5 and Table A1), we build at least 70 mock galaxies by randomly choosing each component parameters p_i in the range $\hat{p}_i - 0.3\hat{p}_i < p_i < \hat{p}_i + 0.3\hat{p}_i$, where $\hat{p}_i$ is the best-fitting value. We create more than 7800 mock galaxies in total. The image size of each mock source range between 200 pixel × 200 pixel (12.8 arcsec × 12.8 arcsec) to 400 pixel × 400 pixel (25.6 arcsec × 25.6 arcsec) to enclose the largest fitted lens of that particular magnitude bin. We convolve the mock galaxies of each magnitude bin with a PSF that was randomly chosen from those produced to fit the systems of that particular magnitude bin. We adopt the same pixel scale, detector gain, and readout noise of the real images. In addition, we add a background level corresponding to the median rms$_{bkg}$ measured in the real images of that particular magnitude bin, and we add the photon noise in order to match the SNR of the mock and real images.

We run GASP2D or GALFIT with the appropriate combination of components to analyse the images of the mock galaxies. We then group the modelled galaxies according to their component combination (i.e. Sérsic, de Vaucouleurs, Sérsic–Sérsic, etc.). For each component of each modelled galaxy, we bin the different values of the mock galaxies in bins of one- or two-magnitude width centred on the magnitude of the best-fitting model component. We study the distribution of the relative errors on the effective surface brightness I_e, effective radius R_e, and Sérsic index n as ($p_{output}/p_{input} - 1$) and of the absolute errors on the position angle PA and axial ratio q as ($p_{output} - p_{input}$). All the distributions appear to be nearly Gaussian after removing all the systems for which the fit failed, for example, when one of the fitted components goes to zero or the model extends significantly more than the cutout. We measure the biweight location and median absolute deviation of each distribution to detect possible systematic errors and derive the errors on the single parameters, respectively. We do not identify any systematic error, as all biweight location values are consistent with zero.

4.2 Non-parametric approach

We use ISOFIT to model the surface brightness distribution of the highly inclined disc foreground lensing galaxies ($i > 80°$) for which GASP2D and GALFIT fail to recover the structural parameters. ISOFIT models the galaxy isophotes, taking into account deviations from a perfect elliptical shape. It supersedes the IRAF[10] task ELLIPSE (Jedrzejewski 1987) by sampling the isophotes according to eccentric

anomaly rather than azimuthal angle and fitting simultaneously all the higher order Fourier harmonics. ISOFIT provides a table with the best-fitting parameters of the galaxy isophotes, which can be used to build the model image through the IRAF task CMODEL (Ciambur 2015). Before fitting the isophotes, we subtract the residual sky level and built the pixel mask, as it has been done for the images of the systems to be fitted with the parametric approach and described in Sections 4.1.1 and 4.1.2. Since ISOFIT models the observed surface brightness distribution of the galaxy through an isophotal fit and without disentangling the light contribution of its structural components, we do not need to account for the image PSF and noise map. The input files needed by ISOFIT are listed in Table 4. Unfortunately, we are not able to model HATLASJ142935 − 002837 (G15v2.19; S_20) due to the low SNR of the image, which is heavily obscured by a complex pattern of dust that is not possible to be successfully masked. For the analysis of S_20, we refer the reader to Calanog et al. (2014) and Messias et al. (2014), who managed to model this lens using Keck and ancillary ALMA observations. As such, the following results are limited to the 63 systems we could model.

4.3 Surface brightness modelling results

After subtracting the foreground lens candidates, we check the residuals for lensing morphology, finding nine new lensed systems. The confirmed lenses increase to 65 systems. For 42 of these, we detect the observed-frame near-IR emission of the background source. As a result, the fraction of confirmed systems increases more than doubled, from 9 per cent to 23 per cent. The number of B, C, and D systems becomes 67, 120, and 29, respectively, while their fractions change to 24 per cent, 43 per cent, and 10 per cent.

Fig. 5 shows the distribution of the flux densities at 500 μm of our sample systems divided according to their classification. Most of the systems have $S_{500} \geq 80$ mJy, except for those from Calanog et al. (2014). We note that, as a consequence of the preliminary nature of the H-ATLAS catalogues used in Negrello et al. (2014), several systems end up having $S_{500} < 80$ mJy in the final release of the H-ATLAS catalogues (Valiante et al. 2016; Maddox et al. 2018). We adopt the revised S_{500} values in Fig. 5. We confirm, according to expectations (Negrello et al. 2007; Wardlow et al. 2013), that the number of A and B systems increases at increasing flux densities, whereas the number of C and D systems peaks at lower flux densities. Unfortunately, due to the sporadic coverage of both the multiwavelength follow-ups and *HST* snapshots, we can not draw meaningful statistical conclusions on the population of lensed DSFGs. In Fig. 6, we show the S_{350}/S_{500} distribution as a function of the flux density at 500 μm for the A systems. In this case, the different colours refer to the different classification methods. *HST* confirmed systems, both before and after the lens subtraction, tend to have lower S_{350}/S_{500} flux density ratios than those of the systems confirmed by multiwavelength follow-ups. This is consistent with them being at lower redshifts and sampling redder, less obscured, stellar emission. Most of the systems have SEDs peaking at 350 μm, as illustrated in Fig. 7. This should be the case for galaxies with

[10]https://github.com/iraf-community/iraf

Table 5. Structural parameters of four representative confirmed lensing systems obtained from a parametric fit of their surface brightness distributions.

No.	IAU name	Type	Components	μ_e [mag arcsec^{-2}]	R_e [arcsec]	n	q	PA [deg]	$m_{\rm PSF}$ [mag]	C/T	χ^2	$N_{\rm dof}$
(1)	(2)	(3)	(4)	(5)	(6)	(7)	(8)	(9)	(10)	(11)	(12)	(13)
S.12	HERMESJ100144+025709	1	Sérsic	21.74 ± 0.05	0.82 ± 0.02	$5.35^{+0.11}_{-0.10}$	0.606 ± 0.005	$71.89^{+0.73}_{-0.76}$	–	[1]	1.05	43 906
S.11	HATLASJ083051+0132225$_1$	2	Sérsic	$22.60^{+0.13}_{-0.12}$	0.36 ± 0.02	4.86 ± 0.36	0.84 ± 0.01	$33.02^{+1.44}_{-1.45}$	–	[1]	1.04	32 063
	HATLASJ083051+0132225$_2$		Sérsic	$23.28^{+0.15}_{-0.13}$	0.69 ± 0.04	$1.34^{+0.13}_{-0.12}$	0.48 ± 0.02	$22.24^{+1.87}_{-1.83}$	–	[1]		
S.8	HERSJ020941.2+001558$_1$	3	Sérsic	$21.13^{+0.19}_{-0.16}$	1.54 ± 0.18	5.11 ± 0.23	0.916 ± 0.004	$82.42^{+0.93}_{-0.99}$	–	$0.56^{+0.07}_{-0.08}$	0.97	121 439
			Sérsic	$23.16^{+0.13}_{-0.12}$	5.03 ± 0.13	$0.75^{+0.07}_{-0.06}$	0.75 ± 0.02	$81.91^{+1.29}_{-1.26}$		$0.31^{+0.06}_{-0.05}$		
			Sérsic	$22.28^{+0.15}_{-0.13}$	$2.10^{+0.06}_{-0.07}$	0.47 ± 0.04	0.92 ± 0.02	$66.03^{+3.11}_{-3.18}$		$0.13^{+0.03}_{-0.02}$		
	HERSJ020941.2+001558$_2$		Sérsic	20.49 ± 0.06	$0.315^{+0.010}_{-0.009}$	2.86 ± 0.07	0.969 ± 0.007	$156.46^{+0.93}_{-0.92}$	–	[1]	0.97	124 612
S.50	HERMESJ021831−053131	1	Sérsic	$23.60^{+0.13}_{-0.12}$	0.83 ± 0.05	5.12 ± 0.38	0.38 ± 0.01	$148.55^{+1.47}_{-1.43}$	–	[1]	1.07	49 835

Notes. Column (1): source reference number. Column (2): IAU name of the *Herschel* detection. Indices 1 and 2 refer to the two components of the system. Column (3): type of the system. Column (4): adopted model for the lens candidate. Columns (5): effective surface brightness (i.e. the surface brightness at the effective radius). Column (6): effective radius (i.e. the semimajor axis of the isophote containing half of the light of the component). Column (7): Sérsic index. Column (8): axis ratio. Column (9): position angle. Column (10): total magnitude of the unresolved component. Column (11): luminosity ratio of the component with respect to the galaxy. Column (12): reduced χ^2 of the fit. Column (13): number of degrees of freedom of the fit. The values in brackets are left fixed in the fit.
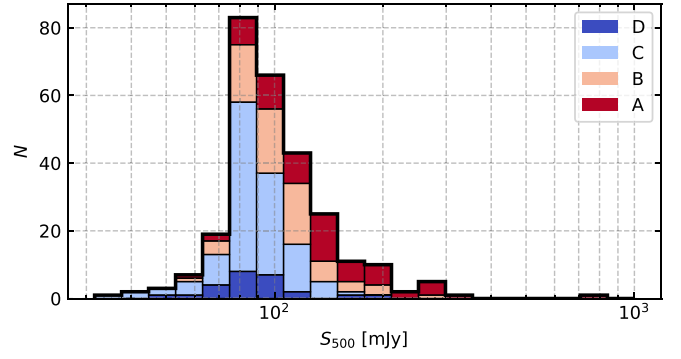
Figure 5. Distribution of the 281 sample systems with *HST* snapshot observations as a function of the S_{500} flux density. The stacked histograms from top to bottom refer to the systems classified as A, B, C, and D, respectively.
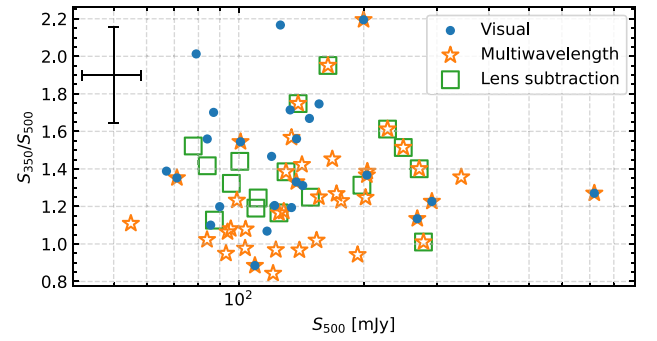
Figure 6. Flux density ratio S_{350}/S_{500} as function of the flux density at 500 μm for the systems classified as A. The circles, stars and squares mark confirmed lenses that are classified according to visual inspection, multiwavelength follow-up observations, and after the lens subtraction, respectively. The cross at the top left corner gives the median measurement error.
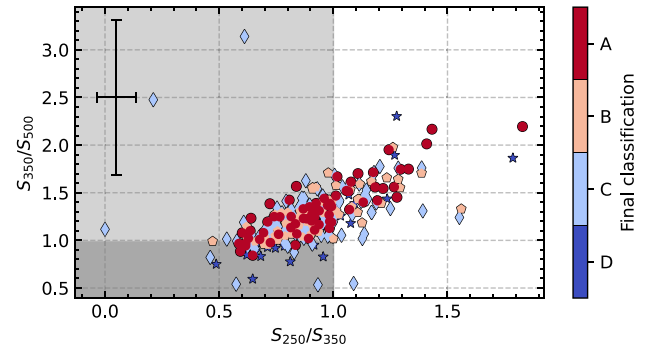
Figure 7. Distribution of the *Herschel* sub-mm flux density ratios of the 281 systems with *HST* snapshot observations. The circles, squares, pentagons, and stars correspond to the A, B, C, and D classes, respectively. The light-shaded area marks the region of the systems with the SED peaking at 350 μm, while the dark-shaded area indicates the region of the systems with the SED peaking at 500 μm. The cross at the top left corner gives the median measurement error.

bright S_{500} flux densities, which are expected to be located at $1 \lesssim z \lesssim 4$ and potentially lensed (González-Nuevo et al. [2012]). We note that the C and D systems tend to spread over a wider range of flux density ratios than the A or B systems. This is in line with them being mostly contaminants with a varying range of intrinsic properties. We find that 47 of the 64 systems classified as A (73 per cent) have
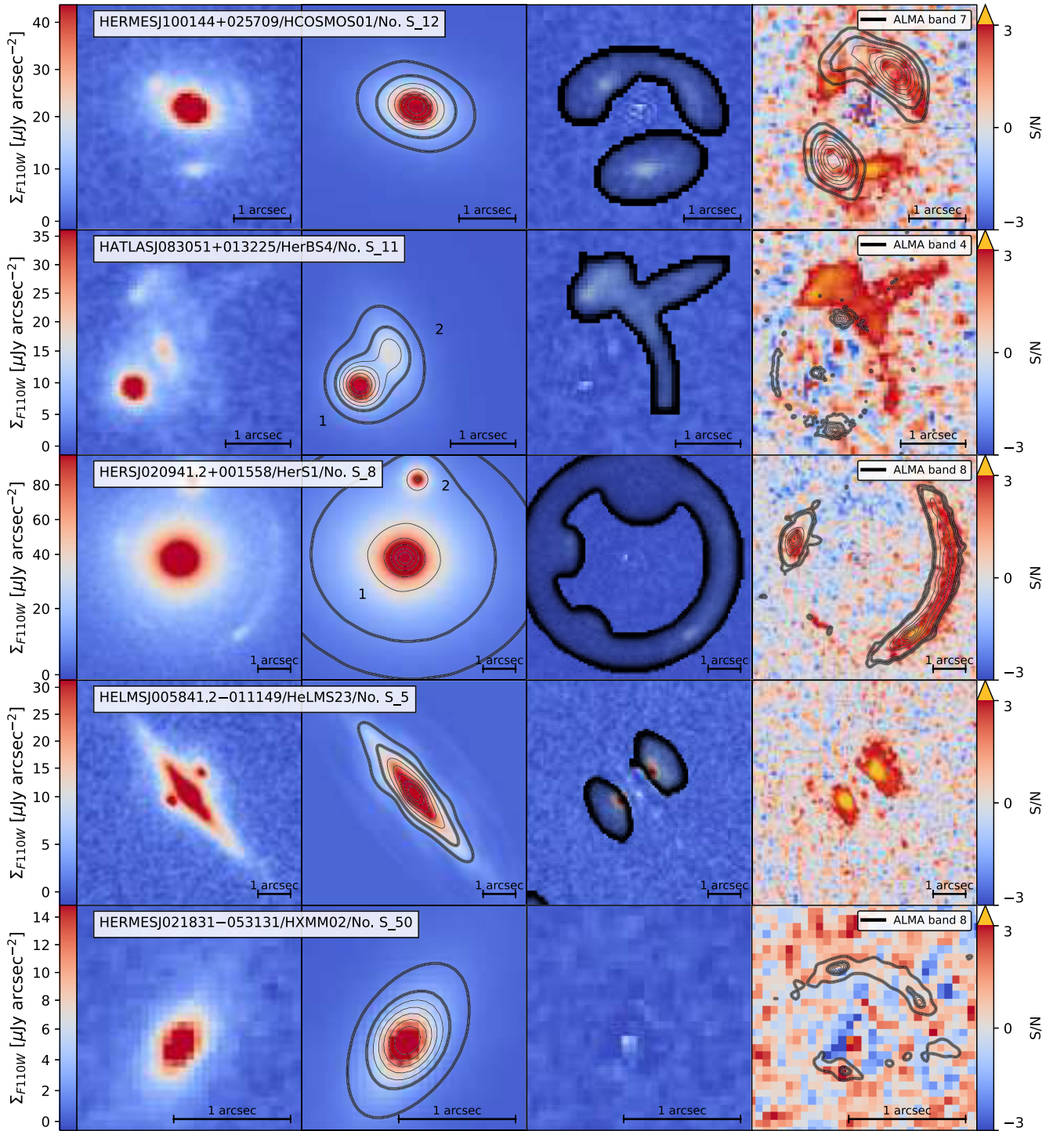
Figure 8. From left to right panels: observed *F110W HST* image, best-fitting lens model, residual, and SNR residual map of five representative lensing systems: one for each type plus a confirmed one by multiwavelength data only. The remaining sample systems are shown in Fig. A1). The best-fitting lens model and residual images result from the surface brightness modelling, while the SNR map is the ratio between the residual image and noise map. The contours in the model images are taken at two levels corresponding to SNR = 5 and 10 (thick curves), and five uniformly spaced levels between the SNR = 10 and the maximum SNR in the model image (thin curves). The residual map shows the pixel mask (corresponding to the black-shaded regions) adopted for the surface brightness modelling. The residual maps show the contours of available high-resolution multiwavelength data taken at two levels corresponding to SNR = 5 and 10 (thick curves), and five uniformly spaced levels between the SNR = 10 and the maximum SNR in the multiwavelength image (thin black curves). The images are oriented such that N is up and E is to the left.

$S_{500} > 100$ mJy, 12 (19 per cent) have $80 < S_{500} < 100$ mJy and 5 (8 per cent) have $S_{500} < 80$ mJy.

In the following, we analyse the systems confirmed as strong lenses (class A). Among the 63 successfully modelled systems,

which comprise one or more than one galaxy, we include the surface brightness distribution of 87 galaxies. A high fraction of these galaxies (~ 47 per cent) show complex surface brightness profiles that often need more than one component (e.g. two or three Sérsic

profiles or a combination of Sérsic profiles and PSF). For three systems (S_47, S_48, and S_81), we include spiral arms too. The parameters of the best-fitting models for four representative systems are given in Table 5. They are three type 1 lenses, one visually confirmed (S_12) and one with multiwavelength observations (S_50). In addition, there is one type 2 system (S_11) and one type 3 system (S_8). The remaining systems can be found in Table A1. In Fig. 8, we show the cutouts of the *HST* images, best-fitting models, *HST* residuals after model subtraction, and SNR maps of the systems listed in Table 5, and one system modelled with ISOFIT (S_5). The remaining systems are shown in Fig. A1.

In the rest of this section, we summarize the properties of each candidate lens we modelled. Table 3 reports the references for the redshifts of the lens and source mentioned hereafter. We find that 34 of the systems discussed here have already been studied in the literature. Bussmann et al. (2013, 2015), Enia et al. (2018), Dye et al. (2018), and Maresca et al. (2022) performed lens modelling and, in some cases, SED fitting of SMA and/or ALMA observations of 30, 29, 12, 6, and 7 sources, respectively, of these 11, 4, 8, 6, and 4 sources were target candidates of our observations and are thus included in our analysis. Giulietti et al. (2022) studied the far-IR/radio correlation of 28 sources, 18 of which are included in our sample. Calanog et al. (2014) analysed 11 more systems of our sample (Table 1), and performed the source reconstruction on the lens-subtracted *HST* images. Cox et al. (2011), Gavazzi et al. (2011), Bussmann et al. (2012), Fu et al. (2012), Messias et al. (2014), Geach et al. (2015), Nayyeri et al. (2017), Butler et al. (2021), Liu et al. (2022), Dye et al. (2022), and Giulietti et al. (2023) analysed single sources. None of these previous works focused on the photometric properties of the lenses or performed a detailed analysis and modelling of their surface brightness. Our results thus represent the best reference for such information. In the following description, we report any relevant information available for each system from these previous works.

4.3.1 HST *confirmed lenses*

HATLASJ000330.6 − 321136 (HerBS155; S_1): we model this type 1 foreground lens at $z_l^{phot} = 0.38$ (Shirley et al. 2021) with two Sérsic components using GASP2D. The background lensed source is located at $z_s^{spec} = 3.08$, as measured by the bright extragalactic ALMA redshift survey (BEARS; Urquhart et al. 2022). It forms two regular arcs on the SE and NW sides of the lens.

HATLASJ000912.7 − 300807 (SD.v1.70; S_2): we model this type 1 foreground lens at $z_l^{phot} = 0.28$ (Shirley et al. 2021) with three Sérsic components using GALFIT to account for the different location of their centres. The background lensed source is located at $z_s^{phot} = 1.19$ (Zhang et al. 2018), and it forms a complex and multicomponent arc-like main image on the SE side of the lens and a compact irregular secondary image on the NW side.

HELMSJ001353.5 − 060200 (HELMS31; S_3): we model this type 1 foreground lens at $z_l^{phot} = 0.60$ (Nayyeri et al. 2016) with a single Sérsic component and an exponential component using GASP2D.

HELMSJ003619.8 + 002420 (HELMS14; S_4): we model this type 1 foreground lens at $z_l^{spec} = 0.26$ (Nayyeri et al. 2016) with three Sérsic components using GALFIT to account for the different location of their centres. The background lensed source is located at $z_s^{spec} = 1.62$ (Cox et al. 2023) and forms an almost complete ring ($r \sim$ 2 arcsec) consisting of a diffuse component and three brighter knots located on the SE, SW, and NW sides of the lens. Two additional

faint NE and SW structures are visible close to the ring, but they do not have a clear lensed morphology.

HELMSJ005841.2 − 011149 (HELMS23; S_5): the foreground lens is a type 1 edge-on galaxy at $z_l^{phot} = 0.38$ (Nayyeri et al. 2016), which we model with ISOFIT. The background lensed source is located at $z_s^{spec} = 1.50$ (Cox et al. 2023) and gives rise to two bright knots along the galaxy minor axis, opposite to each other with respect to the galaxy nucleus.

HERSJ011722.3 + 005624 $_{1,2}$ (HERS10; S_6): this type 3 foreground lensing system is formed by a main galaxy (labelled as '1' in Fig. A1) at $z_1^{phot} = 0.87$ (Nayyeri et al. 2016) and possibly a secondary fainter galaxy (labelled as '2'), for which the redshift is not yet available. This prevents us from being more conclusive about the lensing nature of the secondary galaxy. We model the two galaxies with GASP2D using one Sérsic and one Gaussian component for the brighter galaxy and a single Sérsic component for the fainter one. The background lensed source is located at $z_s^{spec} = 2.47$ (Cox et al. 2023) and forms an arc on the E side of the lens and a diffuse secondary image on the NW side.

HERSJ012620.5 + 012950 (HERS5; S_7): we model this type 1 foreground lens at $z_1^{phot} = 0.43$ (Nayyeri et al. 2016) with one Sérsic and one Gaussian component using GASP2D. The background lensed source is located at $z_s^{spec} = 1.45$ (Cox et al. 2023) and forms two arcs on the NE and SW sides of the lens. The SW arc shows an additional diffuse radial component, which extends westward.

HERSJ020941.2 + 001558$_{1,2}$ (HERS1; S_8): this type 3 foreground lensing system is formed by a main galaxy (labelled as '1' in Fig. 8) and a second fainter galaxy (labelled as '2'), which are both located at $z_1^{spec} = 0.20$ (Nayyeri et al. 2016; Liu et al. 2022). We use GASP2D to model the brighter galaxy with three Sérsic components and the fainter one with a single Sérsic component. The background lensed source at $z_s^{spec} = 2.55$ (Geach et al. 2015) forms a bright extended arc on the SW side of the lens and two knots on the E and SE sides. This system was studied in detail by Geach et al. (2015) and Liu et al. (2022), who measured an Einstein radius of $\theta_E = 2.48^{+0.02}_{-0.01}$ arcsec. It has also been observed with SMA (340 GHz, Liu et al. 2022), ALMA (Band 7, Liu et al. 2022), VLA (1.4 and 5 GHz, Geach et al. 2015), extended Multi-Element Radio Linked Interferometer Network (eMERLIN) (1.52 GHz, Geach et al. 2015) in the sub-mm/mm wavelength range and with *HST* (1.6 μm, Liu et al. 2022), and Keck Near-Infrared Camera 2 (NIRC2) AO (*H* and K_s bands, Liu et al. 2022) in the near-IR. The sub-mm/mm follow-up observations show no significant difference in morphology with those performed in the near-IR.

HERMESJ032637 − 270044 (HECDFS05; S_9): we model this type 1 foreground lens with a single Sérsic component using GASP2D. The background lensed source forms two compact images on the E and W sides of the lens, which is circled by a fainter incomplete ring. This system was studied in detail by Calanog et al. (2014), who measured an Einstein radius of $\theta_E = 0.96^{+0.02}_{-0.03}$ arcsec.

HERMESJ033732 − 295353 (HECDFS02; S_10): we model this type 1 foreground lens at $z_1^{phot} = 0.19$ (Shirley et al. 2021) with three Sérsic components using GASP2D. The background lensed source forms a bright extended arc (divided into two knots on the NE side of the lens) and an inner secondary image on the SW side. This system was studied in detail by Calanog et al. (2014), who measured an Einstein radius of $\theta_E = 1.65^{+0.03}_{-0.05}$ arcsec.

HATLASJ083051 + 013225 $_{1,2}$ (HerBS4; S_11): this type 2 foreground lens is formed by two galaxies, one (labelled as '1' in Fig. 8) at $z_1^{spec} = 0.63$ and the other (labelled as '2') at $z_1^{spec} = 1.00$ (Bussmann et al. 2013). We deblend them with GALFIT by simultaneously modelling their surface brightness with a single Sérsic component

each. The background lensed source at $z_s^{spec} = 3.11$ (Yang et al. [2017]) shows a very complex structure with two intersecting arcs on the NW side of the lens. This system was studied in detail by Enia et al. ([2018]), Yang et al. ([2019]), and Maresca et al. ([2022]) who modelled high-resolution SMA (340 GHz, Bussmann et al. [2013]), ALMA (Band 7, Amvrosiadis et al. [2018]; and Band 4 Yang et al. [2019]) observations. This system was also observed with Keck/NIRC2 AO (K_s band, Calanog et al. [2014]). The sub-mm/mm follow-up observations show a ring around both lenses that splits into two arcs on the SE and S sides of the system, a third compact image on the N side of the second galaxy, and a further compact image between the two lenses.

HERMESJ100144 + 025709 (HCOSMOS01; S_12): we model this type 1 foreground lens at $z_l^{spec} = 0.61$ (Calanog et al. [2014]) with a single Sérsic component using GASP2D. The background lensed source forms three compact images on the NE, S, and NW sides of the lens, which is surrounded by a fainter ring. This system was studied in detail by Calanog et al. ([2014]), who measured an Einstein radius of $\theta_E = 0.91^{+0.01}_{-0.01}$ arcsec. It was also observed with ALMA (Band 7, Bussmann et al. [2015]) in the sub-mm/mm wavelength range and with Keck/NIRC2 AO (K_s band, Calanog et al. [2014]) in the near-IR. The sub-mm/mm follow-up observations show only two lensing features on the NW and SE sides of the lens, with the first one having an arc-like shape. Bussmann et al. ([2015]) used the ALMA data set to measure an Einstein radius of $\theta_E = 0.956 \pm 0.005$ arcsec.

HERMESJ103827 + 581544 (HLock04; S_13): we model this type 1 foreground lens at $z_l^{spec} = 0.59$ [Sloan Digital Sky Survey (SDSS) Data Release 13 (DR13), Albareti et al. [2017]] with two Sérsic components using GASP2D. The background lensed source forms two knots on the SE and NW sides of the lens, which is also surrounded by other fainter and more extended arcs. This system was studied in detail by Calanog et al. ([2014]), who measured an Einstein radius of $\theta_E = 2.40^{+0.01}_{-0.05}$ arcsec and it was also observed with SMA (340 GHz, Bussmann et al. [2013]). The sub-mm/mm follow-up observations show no significant difference in morphology with respect to the near-IR observations, with the exception of a positional offset. Bussmann et al. ([2013]) used the SMA data set to measure an Einstein radius of $\theta_E = 2.0 \pm 0.2$ arcsec.

HERMESJ110016 + 571736 (HLock12; S_14): we model this type 1 foreground lens at $z_l^{spec} = 0.78$ (SDSS DR13, Albareti et al. [2017]) with a single Sérsic component using GASP2D. The background lensed source gives rise to an extended arc on the NW side of the lens and a very faint compact secondary image on the SE side. This system was studied in detail by Calanog et al. ([2014]), who measured an Einstein radius of $\theta_E = 1.14^{+0.04}_{-0.07}$ arcsec.

HATLASJ114638 − 001132$_{1,2}$ (HerBS2; S_15): this type 2 foreground lens is formed by two galaxies at $z_s^{spec} = 1.22$ (Bussmann et al. [2013]), which we deblend by simultaneously modelling them with GALFIT using two Sérsic components each. The background lensed source at $z_s^{spec} = 3.26$ (Yang et al. [2017]) shows a very complex structure with multiple arcs and compact images. This system was studied in detail by Fu et al. ([2012]). It was also observed with ALMA (Band 6, Amvrosiadis et al. [2018]), SMA (340 GHz, Fu et al. [2012]), Plateau de Bure Interferometer (PdBI) (232 GHz, Omont et al. [2013]), and the Jansky Very Large Array (JVLA) (*Ka* band, Fu et al. [2012]) in the sub-mm/mm wavelength range and Keck/NIRC2 AO (*J* and K_s bands, Fu et al. [2012]) in the near-IR. The sub-mm/mm follow-up observations show three images: two arcs that both split into two knots on the S and N sides of the lenses and a compact image between the two lenses. There is only a partial overlap between the near-IR and sub-mm/mm observations.

HATLASJ125126 + 254928 (HerBS52; S_16): we model this type 1 foreground lens at $z_l^{phot} = 0.62$ (Negrello et al. [2017]), with a single Sérsic component using GASP2D. The background lensed source at $z_s^{spec} = 3.44$ (Bakx et al. [2020]) forms four knots located N, NE, S, and NW with respect to the lens, three of which are connected by a fainter arc extending on the N side. This object was also observed with ALMA (Band 6, Prop. ID 2018.1.00526.S, PI: I. Oteo). The sub-mm/mm follow-up observations show the counterparts of the N, NE, and S images.

HATLASJ125760 + 224558 (S_17): we model this type 1 foreground lens at $z_l^{spec} = 0.55$ (SDSS DR13, Albareti et al. [2017]) with a single Sérsic component using GASP2D. The background lensed source at $z_s^{phot} = 1.53$ (Negrello et al. [2017]) forms a compact ring and a brighter knot on the NW side of the lens, which is slightly offset with respect to the ring.

HATLASJ133008 + 245860 (HerBS12; S_18): we model this type 1 foreground lens at $z_l^{spec} = 0.43$ (Bussmann et al. [2013]) with one Sérsic and one Gaussian component using GASP2D. The background lensed source at $z_s^{spec} = 3.11$ (Calanog et al. [2014]) forms three compact images on the N, SE, and SW sides of the lens, which is also surrounded by a fainter incomplete ring. This system was studied in detail by Calanog et al. ([2014]), who measured an Einstein radius of $\theta_E = 0.944^{+0.002}_{-0.001}$ arcsec. It was also observed with ALMA (Band 7, Prop. ID 2018.1.00966.S, N. Indriolo), SMA (340 GHz, Bussmann et al. [2013]), PdBI (240 GHz, Omont et al. [2013]), and NOEMA (283 GHz, Yang et al. [2016]) in the sub-mm/mm wavelength range and with Keck/NIRC2 AO (K_s band, Calanog et al. [2014]) in the near-IR. The sub-mm/mm follow-up observations show no significant difference in morphology with respect to the near-IR observations. Bussmann et al. ([2013]) used the ALMA data set to measure an Einstein radius of $\theta_E = 0.88 \pm 0.02$ arcsec.

HATLASJ133846 + 255057 (HerBS29; S_19): we model this type 1 foreground lens at $z_l^{phot} = 0.42$ (Negrello et al. [2017]) with a single Sérsic component using GASP2D. The background lensed source at $z_s^{phot} = 2.34$ (Bakx et al. [2018]) forms two extended arcs with a sharp break on the S and N sides of the lens. This system was observed with SMA (340 GHz, Bussmann et al. [2013]) too. The sub-mm/mm follow-up observations show no significant difference in morphology with respect to the near-IR ones.

HERMESJ171451 + 592634 (HFLS02; S_21): we model this type 1 foreground lens at $z_l^{spec} = 1.24$ (Shirley et al. [2021]) with a single de Vaucouleurs component using GASP2D. The background lensed source at $z_s^{spec} = 3.18$ (Hernán-Caballero et al. [2016]) forms two arcs on the NE and SW sides of the lens, which is surrounded by a fainter ring. This system was studied in detail by Calanog et al. ([2014]), who measured an Einstein radius of $\theta_E = 0.87^{+0.02}_{-0.05}$ arcsec.

HERMESJ171545 + 601238$_{1,2}$ (HFLS08; S_22): this type 3 foreground lensing system is formed by a main galaxy (labelled as '1' in Fig. [A1]) at $z_l^{phot} = 0.40$ (Shirley et al. [2021]) and possibly a secondary unresolved galaxy (labelled as '2'), for which the redshift is not yet available. This prevents us from being more conclusive about the lensing nature of the secondary galaxy. We used GASP2D to model the brighter galaxy with two Sérsic components and one PSF and the fainter one with a single Sérsic component. The background lensed source at $z_s^{spec} = 2.26$ (Calanog et al. [2014]) forms an extended and irregular arc E of the lens and a compact secondary image on its W side. This system was studied in detail by Calanog et al. ([2014]), who measured an Einstein radius of $\theta_E = 1.95^{+0.05}_{-0.04}$ arcsec.

HATLASJ225844.8 − 295124 (HerBS26; S_23): this type 2 configuration is consistent with two blended galaxies at $z_l^{phot} = 0.69$ (Shirley et al. [2021]), which we deblend by simultaneously fitting them with GALFIT using one and two Sérsic components, respectively. The background lensed source is located at $z_s^{phot} = 2.48$ (Bakx et al. [2018]). It gives rise to an extended arc encircling the lens on the SW

side but without showing any clear secondary image. This is likely due to the shear effect caused by the multiple-lens system.

HELMSJ232210.3 − 033559$_{1,2}$ (HELMS19; S_24): this type 3 foreground lensing system is formed by a main galaxy (labelled as '1' in Fig. A1) at $z_1^{\rm phot} = 0.14$ (Nayyeri et al. 2016) and possibly a secondary fainter galaxy (labelled as '2'), for which the redshift is not yet available. This prevents us from being more conclusive about the lensing nature of the secondary galaxy. We model the two galaxies with GASP2D using two and one Sérsic components, respectively. The background lensed source is located at $z_s^{\rm spec} = 4.69$ (Cox et al. 2023) and forms an extended irregular arc on the E side of the lens, a compact secondary image on the SW side, and possibly a third fainter image on the NW side.

HATLASJ233037.2 − 331217$_{1,2}$ (HerBS123; S_25): this type 3 foreground lensing system is formed by a main galaxy (labelled as '1' in Fig. A1) at $z_1^{\rm phot} = 0.66$ (Shirley et al. 2021) and possibly a secondary unresolved galaxy (labelled as '2'), for which the redshift is not yet available. We deblend and model the two galaxies with GALFIT by using two Sérsic components and a single unresolved component, respectively. The background lensed source is located at $z_s^{\rm spec} = 2.17$, as measured by the BEARS survey (Urquhart et al. 2022). It shows a very complex structure with multiple knots embedded into a main arc and a second inner elongated image on the SE side. This kind of morphology is indicative of strong shear, supporting the idea of a multiple lensing system.

4.3.2 Lenses confirmed after the lens subtraction

HELMSJ001626.0 + 042613 (HELMS22; S_26): we model this type 1 foreground lens at $z_s^{\rm spec} = 0.22$ (Amvrosiadis et al. 2018) with two Sérsic components using GASP2D. The background lensed source at $z_s^{\rm spec} = 2.51$ (Nayyeri et al. 2016) forms an arc on the S side of the lens. This system was observed with ALMA (Band 6, Amvrosiadis et al. 2018; Band 7, Prop. ID 2016.1.01188.S, S. Eales) in the sub-mm/mm wavelength range. The sub-mm morphology shows two compact images on top of the *HST* arc and a secondary image closer to the lens on its NE side. This system was studied in detail by Dye et al. (2018), who measured an Einstein radius of $\theta_{\rm E} = 0.98 \pm 0.07$ arcsec. The sub-mm/mm follow-up observations show both the S arc that splits into two images and a fainter secondary image on the NE side.

HATLASJ002624.8 − 341737 (HerBS22; S_27): we model this type 1 foreground lens at $z_1^{\rm phot} = 0.93$ (Ward et al. 2022) with two Sérsic components using GASP2D. The background lensed source at $z_s^{\rm phot} = 2.70$ (Zhang et al. 2018) forms an arc on the SW of the lens and a fainter secondary image on the opposite side. The SW arc is split into two components: a main one and a fainter one, which are W and S of the lens, respectively.

HELMSJ004723.6 + 015751$_{1,2}$ (HELMS9; S_28): this type 2 foreground lens is formed by two galaxies at $z_s^{\rm spec} = 0.37$ (Amvrosiadis et al. 2018), which we deblend by simultaneously modelling them with GALFIT using two Sérsic components for the main galaxy (labelled as '1' in Table 5) and one de Vaucouleurs component for the second galaxy (labelled as '2'). The background lensed source at $z_s^{\rm spec} = 1.44$ (Nayyeri et al. 2016) shows a very complex structure with one confirmed arc on the N side of the lens and possibly multiple compact images. The background lensed source morphology is likely to be disturbed by additional features possibly related to the interaction with the two lenses. It was observed with ALMA (Band 6, Amvrosiadis et al. 2018) in the sub-mm/mm wavelength range. This system was studied in detail by Dye et al. (2018), who measured

an Einstein radius of $\theta_{\rm E} = 2.16 \pm 0.10$ arcsec. The sub-mm/mm follow-up observations show clearly the N arc we detected in the *HST* image and some hints for further lensed images on the S side of the lens galaxies.

HERSJ012041.6 − 002705 (HERS2; S_29): we model this type 1 foreground lens at $z_1^{\rm phot} = 0.73$ (Nayyeri et al. 2016) with two Sérsic components using GASP2D. The background lensed source forms an arc on the NE of the lens, a clump eastward of the arc and a fainter secondary image on the SW side of the lens.

HATLASJ085112 + 004934 (S_30): we model this type 1 foreground lens at $z_1^{\rm phot} = 0.66$ (Shirley et al. 2021) with three Sérsic components using GASP2D. The background lensed source at $z_s^{\rm phot} = 1.77$ (Manjón-García et al. 2019) forms three arcs on the SW, SE, and NE sides of the lens. The SW arc is divided into two parts by a bright clump. This is likely due to the shear effect caused by nearby galaxies.

HATLASJ085359 + 015537 (G09v1.40; S_31): we model this type 1 foreground lens with two Sérsic components using GASP2D. The background lensed source at $z_s^{\rm spec} = 2.09$ (Yang et al. 2016) forms a ring that splits into two arcs on the E and W sides of the lens. This system was studied in detail by Bussmann et al. (2013), Calanog et al. (2014), and Butler et al. (2021) with ALMA (Band 6, Butler et al. 2021 and Prop. ID 2017.1.00027.S, S. Eales; Band 7, Amvrosiadis et al. 2018 and Butler et al. 2021), and SMA (340 GHz, Bussmann et al. 2013) in the sub-mm/mm wavelength range and with Keck/NIRC2 AO (K_s band, Calanog et al. 2014) in the near-IR, respectively. These works measured an Einstein radius of $\theta_{\rm E} = 0.56^{+0.01}_{-0.02}$ arcsec from the Keck observations and $\theta_{\rm E} = 0.553 \pm 0.004$ arcsec from SMA observations. The sub-mm/mm follow-up observations show no significant difference in morphology with respect to the near-IR ones.

HERMESJ104549 + 574512 (HLock06; S_32): we model this type 1 foreground lens at $z_1^{\rm phot} = 0.20$ (Wardlow et al. 2013) with two Sérsic components using GASP2D. The background lensed source at $z_s^{\rm spec} = 2.91$ (Calanog et al. 2014) forms two images on the NW and SE sides of the lens. Bussmann et al. (2013) used the SMA data set to measure an Einstein radius of $\theta_{\rm E} = 0.10 \pm 0.03$ arcsec.

HERMESJ105551 + 592845 (HLock08; S_)33: this type 2 foreground lens is formed by two galaxies (labelled as '1' and '2' in Fig. A1) at $z_1^{\rm phot} = 0.38$ (Wardlow et al. 2013), which we deblend by simultaneously modelling them with GALFIT using one Sérsic component each. The background lensed source at $z_s^{\rm spec} = 1.70$ (Calanog et al. 2014) shows a complex morphology with a bright arc and a faint secondary image SW and NE of the galaxy 1 respectively, and a possible third image E of the galaxy 2.

HERMESJ105751 + 573026$_{1,2,3,4,5,6}$ (HLock01; S_34): this type 2 foreground lens is formed by a group of six galaxies (labelled from '1' to '6' in Fig. A1) at $z_1^{\rm phot} = 0.60$ (Gavazzi et al. 2011). We simultaneously model them with GALFIT using, respectively, two Sérsic components, one de Vaucouleurs and one Sérsic component, one Sérsic component, one de Vaucouleurs component, one Sérsic component, and a PSF. With respect to Gavazzi et al. (2011) we divide galaxy 5 into two separate components. The background lensed source at $z_s^{\rm spec} = 2.96$ (Gavazzi et al. 2011) forms a bright arc on the NE side of galaxy 1 that splits into two images in the proximity of galaxy 6, two additional bright compact images on the S and NW of galaxy 1, and, a faint counter image near the NE side galaxy 1 (which was predicted but not observed by Gavazzi et al. (2011). This system was also observed with SMA (340 GHz, Bussmann et al. 2013) and with Keck/NIRC2 AO (K_s band, Gavazzi et al. 2011).

HATLASJ132630 + 334410 (NAv1.195; S_35): we model this type 1 foreground lens at $z_l^{\rm spec} = 0.79$ (Bussmann et al. 2013) with one Sérsic component using GASP2D. The background lensed source at $z_s^{\rm spec} = 2.95$ (Bussmann et al. 2013) forms two images on the NW and SE sides of the lens. This system was observed with ALMA (Band 3, Berman et al. 2022 and Band 6, Prop. ID 2017.1.01214.S, Y. Min), and SMA (340 GHz, Bussmann et al. 2013). The sub-mm/mm follow-up observations show no significant difference in morphology with respect to the near-IR ones. Bussmann et al. (2013) and Kamieneski et al. (2023a) used the SMA and ALMA band 3 data sets to measure an Einstein radius of $\theta_{\rm E} = 1.80 \pm 0.02$ and $\theta_{\rm E} = 1.78_{-0.14}^{+0.21}$ arcsec, respectively.

HATLASJ133543 + 300404$_{1, 2, 3, 4}$ (HerBS35; S_36): this type 2 foreground lens is formed by a cluster of galaxies (labelled as '1', '2', '3', and '4' in Fig. A1) at $z_1^{\rm spec} = 0.98$ (Stanford et al. 2014; Nayyeri et al. 2017), which we deblend by simultaneously modelling them with GALFIT using one Sérsic and one PSF component for galaxy 1 and one Sérsic component each for the remaining ones. The background lensed source at $z_s^{\rm spec} = 2.69$ (Nayyeri et al. 2017) shows a complex morphology with a compact bright arc and a faint secondary image NE and SW of the galaxy 1, one arc S of the galaxies 1 and 2, and another arc N of the galaxies 3 and 4. This system was observed with SMA (228 GHz, Nayyeri et al. 2017), the JVLA (4 GHz, Nayyeri et al. 2017), and Keck/NIRC2 AO (K_s and H bands, Nayyeri et al. 2017). The sub-mm/mm follow-up observations show a complex morphology with various arcs and images that are not detected in the near-IR observations.

HATLASJ142140 + 000448 (HerBS140; S_37): we model this type 1 foreground lens at $z_l^{\rm PHOT} = 1.11$ (Shirley et al. 2021) with a single Sérsic component using GASP2D. The background lensed source is located at $z_s^{\rm spec} = 2.78$ (Cox et al. 2023) and forms a faint ring that splits on the N and S sides of the lens and a clump slightly offset of the ring on the NE side of the lens.

HERMESJ142824 + 352620 (HBootes03; S_38): we model this type 1 foreground lens at $z_s^{\rm spec} = 1.03$ (Borys et al. 2006) with two Sérsic components using GASP2D. The background lensed source at $z_s^{\rm spec} = 1.33$ (Borys et al. 2006) forms a closer arc on the NE of the lens and a diffuse secondary image on the SW side of the lens. It was observed with SMA (340 GHz, Bussmann et al. 2013), and ALMA (Band 6, Amvrosiadis et al. 2018) in the sub-mm/mm wavelength range. The sub-mm/mm follow-up observations show no significant difference in morphology with respect to the near-IR observations. This system was studied in detail by Bussmann et al. (2013), who measured an Einstein radius of $\theta_{\rm E} = 2.46_{-0.01}^{+0.01}$ arcsec.

HATLASJ223753.8 − 305828 (HerBS68; S_39): we model this type 1 foreground lens with one Sérsic component using GASP2D. The background lensed source at $z_s^{\rm phot} = 2.13$ (Ward et al. 2022) or $z_s^{\rm phot} = 2.26$ (Manjón-García et al. 2019) forms an arc on the SE side of the lens and a faint secondary image on the E side. The SE arc shows a secondary faint farther arc that extends from the N tip of the main arc.

HATLASJ225250.7 − 313657 (HerBS47; S_40): we model this type 1 foreground lens with one Sérsic component using GASP2D. The background lensed source at $z_s^{\rm phot} = 2.70$ (Manjón-García et al. 2019) forms a bright arc on the NW side of the lens and a faint secondary image on the SE side. Both the arc and secondary image are split into two knots.

HELMSJ233441.0 − 065220 (HELMS1; S_41): we model this type 1 foreground lens with two Sérsic components using GASP2D. For this case, we first model and subtract the main images of the background lensed sources. Then, we mask the residual signal of the source and model the lens. The background lensed source is located at $z_s^{\rm spec} = 1.90$ (Cox et al. 2023) and forms an arc split into three bright unresolved images on the S side of the lens and a faint secondary image on the N side of the lens.

HELMSJ233633.5 − 032119$_{1, 2}$ (HELMS41; S_42): this type 2 foreground lens is formed by two galaxies, which we deblend by simultaneously modelling them with GALFIT using two Sérsic components for the first galaxy (labelled as '1' in Fig. A1) and one Sérsic component for the second galaxy (labelled as '2'). The background lensed source is located at $z_s^{\rm spec} = 2.34$ (Cox et al. 2023) and forms a ring (split into three arcs on the N, E, and W of the lens), as well as a secondary faint, more distant arc and a more diffuse component, which are located close to the N arc.

4.3.3 Sub-mm/mm confirmed lenses

HELMSJ001615.7 + 032435 (HELMS13; S_43): we model this type 1 foreground lens at $z_1^{\rm spec} = 0.66$ (Nayyeri et al. 2016) with one Sérsic component and one Gaussian using GASP2D. The background lensed source at $z_s^{\rm spec} = 2.77$ (Nayyeri et al. 2016) is detected by ALMA (Band 7, Amvrosiadis et al. 2018), and forms a wide arc on the NE side of the lens. No secondary image is found. This system was studied in detail by Dye et al. (2018), who measured an Einstein radius of $\theta_{\rm E} = 2.79 \pm 0.10$ arcsec.

HELMSJ002220.9 − 015524 (HELMS29; S_44): we model this type 1 foreground lens with one Sérsic component using GASP2D. The background lensed source at $z_s^{\rm spec} = 5.16$ (Asboth et al. 2016) was detected by ALMA (Band 6, Prop. ID 2015.1.01486.S, PI: D. Riechers; Band 7, Prop. ID 2015.1.01486.S, PI: D. Riechers; Band 8, Prop. ID 2015.1.01486.S and 2017.1.00043.S, PI: D. Riechers). It forms a ring split into two brighter knots on the N and S sides of the lens. *HST* shows an arc-like structure at ∼1.5–2 times the Einstein radius that is not detected in the sub-mm. We argue that it is part of the foreground galaxy. This system has also available deeper *HST F105W* (Prop. ID 14083, PI: I. Pérez-Fournon), *F125W* (Prop. ID 15464, PI: A. Long), and *F160W* observations (Prop. ID 14083, PI: I. Pérez-Fournon). No counterpart is found in the *HST* after subtracting the lens.

HELMSJ003814.1 − 002252 (HELMS24; S_45): we model this type 1 foreground lens at $z_1^{\rm phot} = 0.17$ (Nayyeri et al. 2016) with one PSF using GASP2D. The background lensed source at $z_s^{\rm spec} = 4.98$ (Su et al. 2017) is detected by ALMA (Band 7, Ma et al. 2019). It forms an arc and a closer faint secondary image on the NE and SW sides of the lens, respectively.

HELMSJ003929.6 + 002426 (HELMS11; S_46): the foreground lens is a type 1 edge-on galaxy, which we model with ISOFIT. The background lensed source is located at $z_s^{\rm spec} = 2.85$ (Cox et al. 2023) and was detected by ALMA (Band 7, Ma et al. 2019). It forms a ring with two brighter knots on the N and S sides of the lens. No *HST* counterpart is found after subtracting the lens.

HELMSJ004714.2 + 032454 (HELMS8; S_47): we model this type 1 foreground lens at $z_1^{\rm phot} = 0.48$ (Nayyeri et al. 2016) with one Sérsic component and one exponential component using GALFIT including also the spiral structure. Additional $m = 2, 3$ Fourier components are added to the spiral arms in order to model their N-S asymmetry. The background lensed source at $z_s^{\rm spec} = 1.19$ (Nayyeri et al. 2016) was detected by ALMA (Band 7, Amvrosiadis et al. 2018). It forms one arc on the S side of the lens and a compact secondary image on the N side. Near-IR counterparts of the background lensed source are visible only for the S arc. This system was studied in detail by Dye et al. (2018), who measured an Einstein radius of $\theta_{\rm E} = 0.59 \pm 0.03$ arcsec.

HELMSJ005159.4 + 062240$_{1,2,3}$ (HELMS18; S_48): this type 2 foreground lens is formed by a group three galaxies at $z_l^{spec} = 0.60$ (Okido et al. 2021), which we deblend by simultaneously modelling them with GALFIT using two Sérsic components for the first galaxy (labelled as '1' in Fig. A1), one de Vaucouleurs component for the second galaxy (labelled as '2'), and one exponential profile, a PSF, and spiral arms for the third galaxy (labelled as '3'). The background lensed source at $z_s^{spec} = 2.39$ (Nayyeri et al. 2016) was detected by ALMA (Band 6, Prop. ID 2017.1.00027.S, PI: S. Eales; Band 7, Amvrosiadis et al. 2018). It forms an arc on the SW side of galaxy 3, and a secondary image on the E side of galaxies 1 and 2. This system was studied in detail by Maresca et al. (2022), who modelled the band 7 observations and measured the Einstein radii to be $\theta_E = 3.80 \pm 0.02$ arcsec for the galaxies 1 and 2, and $\theta_E = 1.46 \pm 0.02$ arcsec for the galaxy 3. No *HST* counterpart is found after subtracting the lens.

HATLASJ005724.2 − 273122 (HerBS60; S_49): we model this type 1 foreground lens at $z_l^{phot} = 0.89$ (Ward et al. 2022) with one Sérsic component using GASP2D. The background lensed source at $z_s^{spec} = 3.26$ (Urquhart et al. 2022) is detected by ALMA (Band 6, Prop. ID 2018.1.00526.S, PI: I. Oteo). It forms a ring that splits into two knots on the E and the W side of the lens, respectively. No *HST* counterpart is found after subtracting the lens.

HERMESJ021831 − 053131 (HXMM02; S_50): we model this type 1 foreground lens at $z_l^{spec} = 1.35$ (Wardlow et al. 2013) with one Sérsic component using GASP2D. The background lensed source at $z_s^{spec} = 3.40$ (Wardlow et al. 2013) is detected by ALMA (Band 6, Prop. ID 2013.1.00781.S, PI: B. Hatsukade; Band 7, Prop. ID 2015.1.01528.S, PI: I. Smail; and Band 8, Prop. ID 2013.1.00749.S, PI: D. Riechers), and SMA (340 GHz, Bussmann et al. 2013). It forms an arc that splits into two knots on the N side of the lens, an elongated second image on the S side of the lens, and a third elongated image on the W side of the lens. This system was studied in detail by Bussmann et al. (2013) and Bussmann et al. (2015), who modelled the ALMA band 6 and SMA observations, respectively. They measured an Einstein radius of $\theta_E = 0.44 \pm 0.02$ and 0.507 ± 0.004 arcsec, respectively. No *HST* counterpart is found after subtracting the lens.

HERMESJ033211 − 270536 (HECDFS04; S_51): we model this type 1 foreground lens with one PSF using GASP2D. The background lensed source is detected by ALMA (Band 7, Bussmann et al. 2015). It forms an arc and a faint secondary image on the S and the NW sides of the lens, respectively. This system was studied in detail by Bussmann et al. (2015), who measured an Einstein radius of $\theta_E = 0.5$ arcsec.

HERMESJ044154 − 540352 (HADFS01; S_52): we model this type 1 foreground lens with one Sérsic component using GASP2D. The background lensed source was detected by ALMA (Band 7, Bussmann et al. 2015). It forms two arcs: one is more extended, splits into two knots, and is located on the E side of the lens, while the other is on the W side. This system was studied in detail by Bussmann et al. (2015), who measured an Einstein radius of $\theta_E = 1.006 \pm 0.004$ arcsec. No *HST* counterpart is found after subtracting the lens.

HATLASJ083932 − 011760 (HerBS105; S_53): the foreground lens is a type 1 edge-on galaxy, which we model with ISOFIT. The background lensed source is located at $z_s^{spec} = 2.67$ (Cox et al. 2023) and was detected by ALMA (Band 6, Prop. ID 2018.1.00526.S, PI: I. Oteo). It forms two blended images separated by the disc of the lens. No *HST* counterpart is found after subtracting the lens.

HATLASJ091841 + 023048$_{1,2}$ (HerBS32; S_54): this type 2 foreground lens is formed by two galaxies which we deblend by simultaneously modelling them with GALFIT using two Sérsic

components for first galaxy (labelled as '1' in Fig. A1) and one de Vaucouleurs component for the second one (labelled as '2'). The background lensed source at $z_s^{spec} = 2.58$ (Harris et al. 2012) is detected by ALMA (Band 3, Prop. ID 2017.1.01694.S, PI: I. Oteo; and Band 7, Giulietti et al. 2022). It forms an arc on the E side of galaxy 1 and a secondary image on the W side of galaxy 2. An additional third ALMA detection is found E of the two galaxies near an *HST* clump and shows a faint near-IR counterpart.

HATLASJ113526 − 014606 (HerBS10; S_55): the background lensed source at $z_s^{spec} = 3.13$ was detected by ALMA (Bands 3, 6, 7, and 8, Giulietti et al. 2023). It forms a wide arc on the SE and a secondary image on the NW. No foreground lens is detected in the near-IR, whereas there is a tentative detection for the background source. This system was studied in detail by Giulietti et al. (2023), who measured an Einstein radius of $\theta_E = 0.4241_{-0.0005}^{+0.0005}$ arcsec.

HATLASJ115433.6 + 005042 (HerBS177; S_56): we model this type 1 foreground lens at $z_l^{phot} = 0.52$ (Shirley et al. 2021) with one Sérsic component using GASP2D. The background lensed source at $z_s^{phot} = 3.90$ (Bakx et al. 2020) is detected by ALMA (Band 7, Prop. ID 2019.1.01784.S, PI: T. Bakx). It forms an arc on the E side of the lens and a secondary image on the W side. Potential near-IR counterparts of the background lensed source are visible on the S of the lens.

HATLASJ120127.6 − 014043 (HerBS61; S_57): we model this type 1 (or 2) foreground lens at $z_l^{phot} = 0.88$ (Shirley et al. 2021) with one Sérsic component and one exponential component using GASP2D. The background lensed source at $z_s^{phot} = 4.06$ (Manjón-García et al. 2019) is detected by SMA (340 GHz, Enia et al. 2018). It forms an arc on the NW side of the lens and a bright secondary image on the SE side. This system was studied in detail by Enia et al. (2018), who measured an Einstein radius of $\theta_E = 0.82 \pm 0.04$ arcsec.

HATLASJ131611 + 281220 (HerBS89; S_58): we model this type 1 foreground lens at $z_l^{phot} = 0.90$ (Berta et al. 2021) with one Sérsic component using GASP2D. The background lensed source at $z_s^{spec} = 2.9497$ (Neri et al. 2020) was resolved by NOEMA (255 GHz, Berta et al. 2021). It forms an arc on the S side of the lens and a compact image on the N side. This system was studied and modelled in detail by Berta et al. (2021), who measured an Einstein radius of $\theta_E = 0.4832 \pm 0.0006$ arcsec. There is a tentative detection of the background lensed source in *HST* on the E and W sides of the lens.

HATLASJ134429 + 303036 (HerBS1; S_59): we model this type 1 foreground lens at $z_l^{spec} = 0.67$ (Bussmann et al. 2013) with one Sérsic component and one exponential component using GASP2D. The background lensed source at $z_s^{spec} = 2.30$ (Harris et al. 2012) was detected by ALMA (Band 7, Falgarone et al. 2017) and SMA (340 GHz, Bussmann et al. 2013). It forms an arc on the W side of the lens and a more distant secondary image on the E side. This system was studied in detail by Bussmann et al. (2013) with the SMA data. They measured an Einstein radius of $\theta_E = 0.92 \pm 0.02$ arcsec.

HATLASJ141352 − 000027$_{1,2,3}$ (HerBS15; S_60): this type 3 foreground lens is formed by a cluster of galaxies at $z_l^{spec} = 0.55$ (Bussmann et al. 2013). We model three of the spectroscopically confirmed members, which are likely contributing to lensing, with GASP2D using one Sérsic and one exponential component for the main lens (labelled as '1' in Fig. A1), and one Sérsic component for the second (labelled as '2') and the third (labelled as '3'). The background lensed source at $z_s^{spec} = 2.48$ (Harris et al. 2012) is detected by ALMA (Bands 3, 6, and 7, Prop. ID, 2018.1.00861.S PI: C. Yang) and forms two arcs, one on the N of the galaxy 3 and the other on the E side of the galaxy 1. The background lensed source is only partly detected in *HST* images.

HATLASJ142414 + 022304$_{1,2}$ (HerBS13, ID 141; S_61): this type 2 foreground lens is formed by two galaxies at $z_1^{\rm spec} = 0.60$ (Bussmann et al. 2012), which we deblend by simultaneously modelling them with GALFIT using one Sérsic component and a PSF for the first galaxy (labelled as '1' in Fig. A1) and one Sérsic component for the second one (labelled as '2'). The background lensed source at $z_s^{\rm spec} = 4.24$ (Cox et al. 2011) is detected by ALMA (Bands 3 and 4, Dye et al. 2022; Bands 5, 6, and 7, Dye et al. 2018; and Band 8 Prop. ID 2016.1.00284.S, PI: J. Bernard-Salas), and SMA (340 GHz, Bussmann et al. 2012; and 880 GHz, Cox et al. 2011). No *HST* counterpart is found after subtracting the lens.

HERMESJ142826 + 345547 (HBootes02; S_62): the foreground lens at $z_1^{\rm spec} = 0.41$ (Wardlow et al. 2013) is a type 1 edge-on galaxy which we model with ISOFIT. The background lensed source at $z_s^{\rm spec} = 2.41$ (Wardlow et al. 2013) was detected by SMA (340 GHz, Bussmann et al. 2013) and JVLA (7 GHz, Wardlow et al. 2013). It forms an arc that splits into two knots and is located on the SE side of the lens, and a fainter secondary image on the NW side of the lens. No *HST* counterpart is found after subtracting the lens.

HATLASJ230815.5 − 343801 (HerBS28; S_63): we model this type 1 foreground lens at $z_1^{\rm phot} = 0.72$ (Ward et al. 2022) with two Sérsic components using GASP2D. The background lensed source at $z_s^{\rm phot} = 4.03$ (Manjón-García et al. 2019) is detected by ALMA (Band 6, Prop. ID 2018.1.00526.S, PI: I. Oteo). It forms an arc that splits into two knots and is located on the N side of the lens and a secondary image on the W side of the lens. No *HST* counterpart is found after subtracting the lens.

HELMSJ232439.5 − 043936 (HELMS7; S_64): we model this type 1 foreground lens with two Sérsic components using GASP2D. The background lensed source at $z_s^{\rm spec} = 2.47$ (Nayyeri et al. 2016) is detected by ALMA (Band 6, Amvrosiadis et al. 2018; and 7, Prop. ID 2017.1.00027.S, PI: S. Eales). It forms three arcs, two of them are located close to the lens on its W and E sides, whereas the third arc is near an *HST* clump on the E side of the lens. This kind of morphology is indicative of the presence of multiple lenses, which possibly are the *HST* clump and a further clump one on the NW side of the main lens. This system was studied in detail by Maresca et al. (2022), who adopted two lenses and measured their Einstein radii to be $\theta_{\rm E} = 0.54 \pm 0.01$ and 0.40 ± 0.01 arcsec, respectively. At the position of the second lens, there is no *HST* detection.

HELMSJ233620.8 − 060828 (HELMS6; S_65): we model this type 1 foreground lens at $z_1^{\rm spec} = 0.40$ (Nayyeri et al. 2016) with two Sérsic components using GASP2D. The lens is also part of the cluster that hosts other strong lensing events (see Carrasco et al. 2017 for details). The background lensed source at $z_s^{\rm spec} = 3.43$ (Nayyeri et al. 2016) was detected by ALMA (Band 6, Prop. ID 2021.1.01116.S, PI: D. Riechers and Amvrosiadis et al. 2018; and Band 8, Prop. ID 2013.1.00749.S, PI: D. Riechers). It forms four images: two of them are on the S side of the lens and are connected by an arc, a third one is on the W side, and a fourth one is on the NE side. Near-IR counterparts of the background lensed source are visible only for the S images.

4.3.4 Uncertain lenses

HATLASJ013840.5 − 281855 (HerBS14; S_81): it is unclear whether this source at $z^{\rm spec} = 3.78$ (Urquhart et al. 2022) is strongly lensed. It was detected by ALMA (Band 6, Prop. ID 2018.1.00526.S, PI: I. Oteo) and shows one elongated component. Due to the ∼0.6 arcsec resolution, it is not possible to exclude the presence of background lensed sources with very low angular separation. The candidate lens is an edge-on spiral galaxy at $z^{\rm phot} = 0.61 \pm 0.28$ (Ward et al. 2022).

HERMESJ022017 − 060143$_{1,2}$ (HXMM01; S_85): this system is confirmed to be a DSFG pair that is weakly lensed by a pair of foreground galaxies. This type 3 foreground system is formed by an edge-on disc galaxy (labelled as '1' in Fig. A1) at $z_1^{\rm phot} = 0.87$ (Nayyeri et al. 2016) and a second rounder and ringed galaxy (labelled as '2'). The sources at $z_s^{\rm phot} = 0.87$ (Fu et al. 2012) were detected by ALMA (Band 6, Bussmann et al. 2015 and Prop. ID 2015.1.00723.S, PI: I. Oteo; Band 7, Prop. ID 2011.0.00539.S, PI: D. Riechers), SMA (340 GHz, Fu et al. 2012), and JVLA (30 GHz, Fu et al. 2012) in the sub-mm/mm and by Keck/NIRC2 AO (K_s, Fu et al. 2012) in the near-IR. The background sources are located between the two lenses, one on the S side of them and the other on the N side.

HERMESJ022135 − 062617 (HXMM03; S_88): it is unclear whether this background source at $z_s^{\rm spec} = 2.72$ (Bussmann et al. 2015) is strongly lensed. We model the brightest cluster galaxy of a candidate lensing cluster at $z_1^{\rm spec} = 0.31$ (Albareti et al. 2017) with two Sérsic components using GASP2D. The source was detected by ALMA (Band 7, Bussmann et al. 2015). It forms a bright arc and is located on the E side of the lens. No secondary image was picked up by ALMA. Unfortunately, the W side of the candidate lens, where the counter image is expected to be found, is outside the ALMA Band 7 FOV. A near-IR counterpart of the ALMA arc is clearly visible and shows a complex morphology with multiple knots, while the secondary image is not found even after subtracting the potential lens. One possibility is that the source is only weakly lensed by the foreground structure.

HERMESJ045058 − 531654 (HADFS03; S_91): this system was proposed to be a group of three weakly lensed DSFGs by a foreground edge-on disc galaxy (Bussmann et al. 2015). It was detected by ALMA (Band 7, Bussmann et al. 2015) and forms three compact clumps near the candidate lens. All the ALMA clumps are on the S on the candidate lens and, as such, are not consistent with the usual strong lensing morphology.

HERMESJ143331 + 345440 (HBootes01; S_116): it is unclear whether this background source at $z^{\rm spec} = 3.27$ (Wardlow et al. 2013) is strongly lensed. It was detected by SMA (340 GHz, Bussmann et al. 2013), and shows one elongated component. Due to the ∼0.6 arcsec resolution, it is not possible to exclude the presence of background lensed sources with very low angular separation. We model the candidate lensing system at $z^{\rm phot} = 0.59$ with one Sérsic component.

HELMSJ235331.7 + 031717 (HELMS40; S_139): it is unclear whether this source located at $z_s^{\rm spec} = $ (Cox et al. 2023) is strongly lensed. The source was detected by ALMA (Band 7, Amvrosiadis et al. 2018). It forms two pairs of compact sources. The first pair (on the SE side of the cutout) shows a possible near-IR detection but no foreground lens candidate. The members of the second pair are located on the N and S sides of a possible lensing galaxy, respectively, and they do not show any *HST* counterpart. We model the candidate lensing system with two Sérsic components and a Gaussian using GALFIT to account for the different locations of their centres. This system was studied in detail by Maresca et al. (2022), who modelled the SE pair and measured an Einstein radius of $\theta_{\rm E} = 0.21 \pm 0.01$ arcsec. We note that the lens redshift adopted by Maresca et al. (2022) is likely associated with a close-by spiral galaxy on these sides of the SE pair.

HATLASJ011014.5 − 314813 (HerBS160; S_153): it is unclear whether this background source at $z^{\rm spec} = 3.96$ (Urquhart et al. 2022) is strongly lensed. It is detected by ALMA (Band 6, Prop. ID 2018.1.00526.S, PI: I. Oteo) and forms an elongated, arc-like structure near a faint *HST* counterpart. We find no secondary image.

HERMESJ023006 − 034153 (HXMM12; S_170): this system was proposed to be a weakly lensed DSFG by a group of foreground galaxies (Bussmann et al. 2015). It was detected by ALMA (Band 7, Bussmann et al. 2015) and forms an arc-like structure near a faint *HST* counterpart. We find no secondary image.

HERMESJ043341 − 540338 (HADFS04; S_175): this system was proposed to be a system of three DSFGs that is weakly lensed by a foreground group of galaxies (Bussmann et al. 2015). It was detected by ALMA in Band 7 (Bussmann et al. 2015), the two DSFGs are located on the SE and NE sides of the foreground galaxy. This system was studied in detail by Bussmann et al. (2015), who assumed an Einstein radius of 0.5 arcsec. A near-IR counterpart of the ALMA southernmost source is visible.

HATLASJ144556.1 − 004853 (HERBS46; S_249): it is unclear whether this background source is strongly lensed. It was detected by SMA (340 GHz, Bussmann et al. 2013), and shows one elongated component near a faint *HST* counterpart. Due to the ∼0.6 arcsec resolution, it is not possible to exclude the presence of background lensed sources with very low angular separation.

HATLASJ224207.2 − 324159 (HerBS67; S_262): it is unclear whether this background source at $z^{phot} = 3.57$ (Bakx et al. 2018) is strongly lensed. It was detected by ALMA (Band 6, Prop. ID 2018.1.00526.S, PI: I. Oteo) and shows one elongated component. Due to the ∼0.6 arcsec resolution, it is not possible to exclude the presence of background lensed sources with very low angular separation.

4.4 Properties of the lenses

Since ∼ 47 per cent of the modelled lensing galaxies are composed of multiple components, it is necessary to use a set of parameters that describes the global properties of the surface brightness distribution and does not depend on the number and type of components used to model the galaxy. We therefore use the total effective radius R_{50} (i.e. the radius and surface brightness of the circularized isophote that contains half of the light of the galaxy), total effective surface brightness μ_{50}, and total magnitude m_{F110W}. For each galaxy, we sampled 10^4 different combinations of its components to take into account the uncertainties of the best-fitting model of the surface brightness distribution. This is done through a set of truncated normal distributions (one for each component parameter) with central value being the best-fitting value from the surface brightness model, standard deviation the uncertainty of the best-fitting value, and ranges $[0, \infty)$ ADU pixel^{-1}, $[0, \infty)$ pixel, [0.3,10], [0,1], and [0,360] deg for μ_e, R_e, n, q, and PA, respectively. For all the combinations, we estimate R_{50} by computing the curve of growth (COG) and retrieving the radius within which half of the total flux is encircled. The μ_{50} value is derived from the surface brightness profile at R_{50}, while the m_{F110W} value is obtained by summing the luminosities of all the components. For each parameter, we calculate the median and the 16 per cent and 84 per cent percentiles from the cumulative distribution function. Additionally, we estimate the $C_{31} = R_{75}/R_{25}$ concentration index (e.g. Watkins et al. 2022) in order to compare our results with the literature. To derive the distributions of R_{25} and R_{75}, which correspond to the radii containing 25 per cent and 75 per cent of the total luminosity, respectively, we apply the same procedure as done for R_{50}.

For the edge-on lenses of S_5, S_46, S_53, and S_62, we run ISOFIT on the model image (Fig. 8) after having deconvolved it with the PSF, and then we use the result to produce the COG. We also measure the surface brightness radial profile. We use the COG to estimate the values of R_{25}, R_{50}, and R_{75} and to assess their uncertainties,

we build a set of 10^4 COGs for each galaxy. We sample the flux within each circularized radius with a Gaussian distribution centred on the measured flux value and with standard deviation being the flux Poisson uncertainty. The circularized radius is sampled with a Gaussian distribution centred on the measured radius value and with standard deviation being the uncertainty on the ellipticity as measured by ISOFIT. We use the surface radial profile to estimate the values of μ_{50}, and to assess its uncertainty, we build a set of 10^4 surface brightness radial profiles. At each radius, we adopt a Gaussian distribution centred on the measured value of surface brightness, with standard deviation being the uncertainty measured by ISOFIT.

In Fig. 9, we show the C_{31} distribution of our lenses. The peak at $C_{31} \simeq 7$ is due to the systems that we model with a de Vaucouleurs profile and have all the same concentration. We measure a median $\langle C_{31} \rangle = 6.8 \pm 0.4$, which is slightly higher than the median value $\langle C_{31} \rangle = 5.2 \pm 0.1$ measured by Watkins et al. (2022) for a sample of nearby ETGs observed with *Spitzer* at 3.6 μm. This finding and the observed morphology of smooth and featureless elliptical systems provide further evidence that our lenses are mostly ETGs. Lastly, we measure the flux densities at 1.1 μm $S_{1.1}$ of the background sources by taking the aperture photometry in the regions dominated by the lensing features on the lens-subtracted residuals. The uncertainties $\sigma_{S_{1.1}}$ are computed with $\sigma_{S_{1.1}}^2 = \sum_{i,j} \sigma_{i,j}^2$, where $\sigma_{i,j}$ is the noise map. The values of $S_{1.1}$ and their uncertainties are given in Table 6 and Table A2.

For the 68 lensing foreground galaxies with known photometric or spectroscopic redshift, we convert the size of the total effective radius from arcsec to kpc through the angular diameter distance and the total magnitude to absolute magnitude M_{F110W} through the luminosity distance. We also correct the total effective surface brightness for cosmological dimming by multiplying the *F110W* fluxes by a factor of $(1 + z)^4$. This is done for the parameter distributions as derived before. To take into account the uncertainties on the photometric redshifts, we sample a truncated normal distribution centred on the redshift measurement, with standard deviation being the uncertainty and range $[0, \infty)$. When more than one potential lens is present (i.e. for type 2 and 3 systems), we correct for the redshift only if the secondary potential lens has a spectroscopic redshift (S_8, S_11, S_15, and S_36) or none of the lenses dominates the available photometric redshift (S_23, S_28, and S_33). To denote the parameters corrected for the lens redshifts, we add a subscript '0'. In Table 6, we list the measured values of m_{F110W}, M_{F110W}, R_{50}, $R_{50,0}$, μ_{50}, $\mu_{50,0}$, and C_{31} for the five representative systems shown in Fig. 8, while in Table A2 we show the parameters for the rest of the sample.

Fig. 9 shows the distribution of $R_{50,0}$ in kpc, $\mu_{50,0}$ in mag arcsec^{-2}, C_{31}, M_{F110W} in mag, z_l, and z_s. For each parameter, we stack all the single-system parameter distributions to take into account the varying uncertainties between different systems. We bin them together and normalized for the total number of realizations (i.e. 10^4 for each system).

5 LENS MODELLING

For the 34 systems for which we can confidently identify a galaxy acting as the main lens and the background source in the *HST* images, we proceed to estimate the Einstein radius θ_E from the residual images. Depending on the morphology of the lensing features, we define θ_E as either the radius of the circle centred on the lens that best fits the Einstein ring (e.g. S_4), or as half of the separation between the multiple images (e.g. S_2) following the approach of
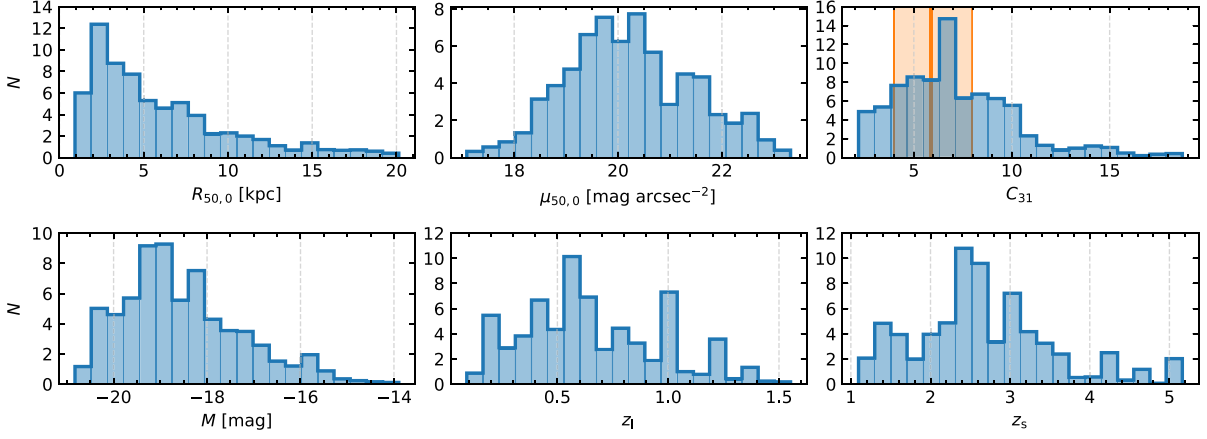
Figure 9. Distribution of the total effective radii $R_{50,0}$ (top left panel), total effective surface brightnesses $\mu_{50,0}$ (top central panel), concentrations C_{31} (top right panel), total absolute magnitudes M_{F110W} (bottom left panel), redshifts z_l of the foreground lenses (bottom central panel), and redshifts z_s of the background sources (bottom right panel). All the foreground lenses and background sources with a measured redshift are included. The thick vertical line corresponds to the median of the values of C_{31} of the ETGs sample of Watkins et al. (2022), while the shaded region marks the corresponding $\pm 1\sigma$ confidence interval.

Table 6. Derived properties of five representative lensing systems.

No.	IAU name	m_{F110W} [mag] M_{F110W} [mag]	μ_{50} [mag arcsec^{-2}] $\mu_{50,0}$ [mag kpc^{-2}]	R_{50} [arcsec] $R_{50,0}$ [kcp]	C_{31}	$\mu S_{1.1}$ [μJy]
(1)	(2)	(3)	(4)	(5)	(6)	(7)
S_12	HERMESJ100144 + 025709	$19.17^{+0.08}_{-0.08}$	$21.74^{+0.05}_{-0.05}$	$0.64^{+0.02}_{-0.02}$	$9.37^{+0.20}_{-0.20}$	$10.14^{+0.17}_{-0.17}$
		$-20.17^{+0.08}_{-0.08}$	$18.96^{+0.05}_{-0.05}$	$5.10^{+0.13}_{-0.13}$		
S_11	HATLASJ083051 + 013225$_1$	$21.54^{+0.18}_{-0.18}$	$22.60^{+0.13}_{-0.12}$	$0.33^{+0.02}_{-0.02}$	$8.47^{+0.66}_{-0.64}$	$6.79^{+0.11}_{-0.11}$
		$-16.86^{+0.18}_{-0.18}$	$20.48^{+0.13}_{-0.12}$	$2.30^{+0.13}_{-0.13}$		
	HATLASJ083051 + 013225$_2$	$22.05^{+0.21}_{-0.19}$	$23.28^{+0.15}_{-0.13}$	$0.48^{+0.03}_{-0.03}$	$3.21^{+0.16}_{-0.15}$	
		$-17.59^{+0.21}_{-0.20}$	$20.27^{+0.15}_{-0.13}$	$3.94^{+0.26}_{-0.25}$		
S_8	HERSJ020941.2 + 001558$_1$	$16.15^{+0.18}_{-0.17}$	$21.27^{+0.19}_{-0.17}$	$2.47^{+0.13}_{-0.12}$	$5.35^{+0.45}_{-0.47}$	$18.72^{+0.34}_{-0.34}$
		$-19.38^{+0.18}_{-0.17}$	$20.47^{+0.19}_{-0.17}$	$8.48^{+0.46}_{-0.40}$		
	HERSJ020941.2 + 001558$_2$	$19.82^{+0.09}_{-0.09}$	$20.49^{+0.06}_{-0.06}$	$0.310^{+0.010}_{-0.009}$	$5.24^{+0.10}_{-0.10}$	
		$-15.71^{+0.09}_{-0.09}$	$19.69^{+0.06}_{-0.06}$	$1.06^{+0.03}_{-0.03}$		
S_5	HELMSJ005841.2 − 011149	$18.910^{+0.001}_{-0.001}$	$20.26^{+0.02}_{-0.02}$	$0.478^{+0.005}_{-0.006}$	$3.05^{+0.04}_{-0.04}$	$14.55^{+0.10}_{-0.10}$
		$-18.15^{+0.57}_{-0.48}$	$18.88^{+0.25}_{-0.24}$	$2.54^{+0.31}_{-0.35}$		
S_50	HERMESJ021831 − 053131	$21.55^{+0.19}_{-0.18}$	$23.60^{+0.13}_{-0.12}$	$0.51^{+0.03}_{-0.03}$	$8.95^{+0.71}_{-0.69}$	<0.04
		$-18.89^{+0.19}_{-0.18}$	$19.89^{+0.13}_{-0.12}$	$4.40^{+0.27}_{-0.26}$		

Notes. Column (1): source reference number. Column (2): IAU name of the *Herschel* detection. Indices 1 and 2 refer to the two components of the lens candidate. Column (3): apparent magnitude of the model (first row), absolute magnitude of the model (second row). Column (4): total effective radius in arcsec (first row) and in kpc (second row). Column (5): total effective surface brightness before (first row) and after correcting for cosmological dimming (second row). Column (6): concentration index of the model.

Amvrosiadis et al. (2018). For the uncertainty on θ_E, we adopt the value corresponding to one-third of the observed width of the lensing feature. We use these rough estimates as priors for proper lens modelling.

The lens modelling is performed with PYAUTOLENS[11] (Nightingale, Dye & Massey 2018; Nightingale et al. 2021), by using a non-linear search trough DYNESTY (Speagle 2020).[12] In order to reduce

the complexity of the lens model, we adopt a singular isothermal ellipsoid (SIE) for the mass model (see Nightingale et al. 2018 for details). It has five free parameters, the differences δx_{SIE} and δy_{SIE} of the centre coordinates of the mass distribution relative to the centre coordinates of the lens surface brightness, Einstein radius θ_E, and elliptical components $\epsilon_{SIE,1} = f_{SIE}\sin(2PA_{SIE})$, $\epsilon_{SIE,2} = f_{SIE}\cos(2PA_{SIE})$, where $f_{SIE} = (1 - q_{SIE})/(1 + q_{SIE})$, PA_{SIE} is the position angle of the mass profile, and q_{SIE} is its flattening.

From the lens-subtracted images and noise maps as obtained in Section 4, we set up the inputs for the lens modelling. We crop the images and we mask the regions that do not include lensing features

---

[11]PYAUTOLENS is available from https://github.com/Jammy2211/PyAutoLens
[12]DYNESTY is available from https://dynesty.readthedocs.io/en/stable/

in order to reduce the computation time. To this aim, we also crop the PSF to ∼ 5 FWHM × 5 FWHM cutouts. We then mask any residual from the lens subtraction and non-modelled nearby contaminants. We estimate the position of the lensing features by locating the brightest pixel in 5 pixel × 5 pixel boxes encompassing the lensing features. These estimates are used by PYAUTOLENS to constrain the location of the background source in the source plane (see Nightingale et al. 2018 for details).

We proceed with the lens modelling with the following approach. First, we perform a parametric fit by fitting both the mass model and background source with parametric functions. We use a single Sérsic component for the parametric background source. This fit has a total of twelve free parameters: five for the mass model and seven for the background source. The priors for the mass model are a Gaussian distribution centred on the cutout centre with $\sigma = 0.1$ arcsec for $\delta x_{\rm SIE}$ and $\delta y_{\rm SIE}$; a Gaussian distribution centred on the estimated $\theta_{\rm E}$ with σ three times its error; a Gaussian distribution centred on 0 with $\sigma = 0.3$ for $\epsilon_{\rm SIE, 1}$ and $\epsilon_{\rm SIE, 2}$, respectively. The priors for the background source are Gaussian distribution centred on the cutout centre with $\sigma = 0.3$ arcsec for $x_{\rm s}$ and $y_{\rm s}$; a log-uniform distribution between 10^{-6} and 10^{6} ADU for $I_{\rm s, eff}$; a uniform distribution between 0 and 30 arcsec for $R_{\rm s, eff}$; a uniform distribution between 0.8 and 5.0 for $n_{\rm s}$; a Gaussian distribution centred on 0 with $\sigma = 0.3$ for $\epsilon_{\rm s, 1}$ and $\epsilon_{\rm s, 2}$ (defined in a similar way as $\epsilon_{\rm SIE, 1}$ and $\epsilon_{\rm SIE, 2}$), respectively. As position threshold, we use a Gaussian distribution centred on the previously identified position with $\sigma = 0.5$ arcsec for all the systems, except for S_41. For the latter, we adopt $\sigma = 0.1$ due to the small angular separation of the lensed images. We then use the posteriors of the mass model obtained in this parametric fit and the priors on the position of the background sources on the image plane to initialize a Voronoi pixelization with a constant regularization coefficient λ (see Nightingale et al. 2018 for details). For the pixelization, we use as priors a uniform distribution between 20 and 45 pixels for the shape of the pixelization and a log-uniform distribution between 10^{-6} and 10^{6} for λ. We do this pixelized initialization fit by marginalizing the lens model over the mass model and only fitting the pixelization. In a similar fashion, we marginalize over the resulting pixelization to fit the mass model with priors defined by the parametric fit posteriors. We consider this fit as the best guess for the lens model and source reconstruction.

In the cases of S_6, S_11, S_22, S_24, S_27, and S_31, the SNR of the background lensed sources is not high enough to produce reliable results. S_2, S_5, S_25, and S_41 show very complex and/or clumpy lensed background source morphologies that needed additional information on what is part of the background source or additional multiple images. Whereas, S_26 shows residuals related to the lens subtraction that prevent us from building the model. For S_3, S_19, and S_40, the SIE mass model is not sufficient to correctly reproduce the observations, so we add a shear component, defined, as for the mass model, through the elliptical components $\epsilon_{\rm shear, 1}$ and $\epsilon_{\rm shear, 2}$. This is done to improve the mass model and not to model an actual external shear (see Etherington et al. 2023 for details). The priors for the shear elliptical components are uniform distributions between -0.2 and 0.2.

For each modelled lens, we extract 500 fits from the lens modelling parameters posteriors, and, for each fit, we compute the regions of the source plane with SNR > 3. We compute the magnification by taking the ratio between the fluxes of the regions on the source plane and the image plane after mapping them back. We measure the sizes of the source plane by computing the radii of the circularized regions that we used to compute the magnifications. The distribution of the physical sizes of our systems is shown in Fig. 10. As before, the
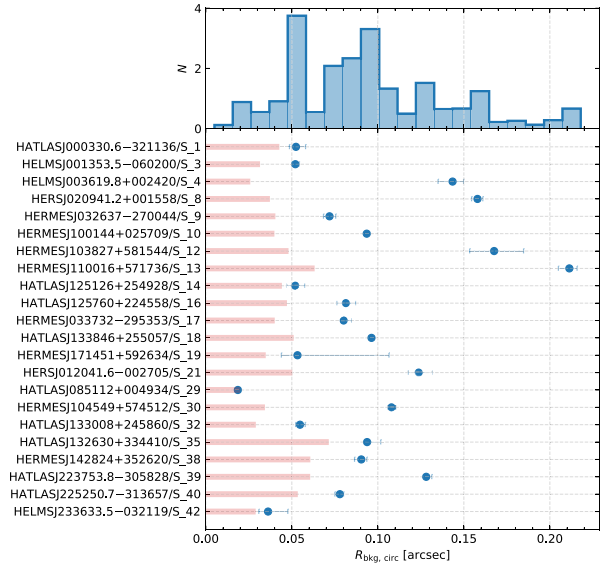
Figure 10. Top panel: distribution of the circularized radius of the background sources from the lens modelling and taking into account the uncertainties on the radii. Bottom panel: circularized radius of the background sources (circles) and HWHM of the PSF of the image corrected for the lensing magnification (thick horizontal segments).

results of the lens modelling for S_7 are shown in Fig. 11, while the results for the remaining lenses are reported in Table 7 and Fig. C1.

A comparison between our Einstein radii and those available in the literature (Bussmann et al. 2013, 2015; Calanog et al. 2014; Geach et al. 2015; Enia et al. 2018; Dye et al. 2022; Maresca et al. 2022; Kamieneski et al. 2023a) is shown in Table 8 and Fig. 12. Our values are comparable with what is found in the literature, with only two exceptions: S_38 which Bussmann et al. (2013) did not resolve with SMA, due to the very low angular separation of the multiple images and assumed to have Einstein radius of 0.1 ± 0.3 arcsec; and S_10 for which Calanog et al. (2014) fixed the flattening and position angle of the mass model to be circular and aligned with the lens.

6 DISCUSSION

Consistent with expectations (Perrotta et al. 2002; Lapi et al. 2012; Negrello et al. 2017) our 65 confirmed lenses mostly comprise systems where the lens is a single galaxy (51). Only four are made of spectroscopically confirmed groups or clusters (S_36, S_48, S_60, and S_61), and nine systems have a morphology consistent with a group (S_6, S_15, S_23, S_25, S_28, S_33, S_34, S_54, and S_63). The lensing galaxies are nearly all ETGs, with the only exceptions of S_47 and one of the galaxies in the lensing cluster of S_48. Both of them show a clear spiral structure. The ETG nature of the lensing galaxies is further confirmed by their concentrations, with 92 per cent of our sample lenses being more concentrated than expected for an exponential disc.

The mass within the Einstein radii of the foreground lenses ranges between 9.9×10^{10} M$_\odot$ (1st percentile) and 6.4×10^{11} M$_\odot$ (99th percentile). The mass-to-light ratios in the *F110W* filter within the Einstein radius range between 1.25 and 8.86 M$_\odot$ L$_\odot^{-1}$. The background sources host a variety of morphologies, including single compact sources (e.g. S_12), more diffuse sources (e.g. S_18), and multiple clumps (S_17). We find that 14 out of 22 reconstructed background sources are single sources, whereas the remaining 8
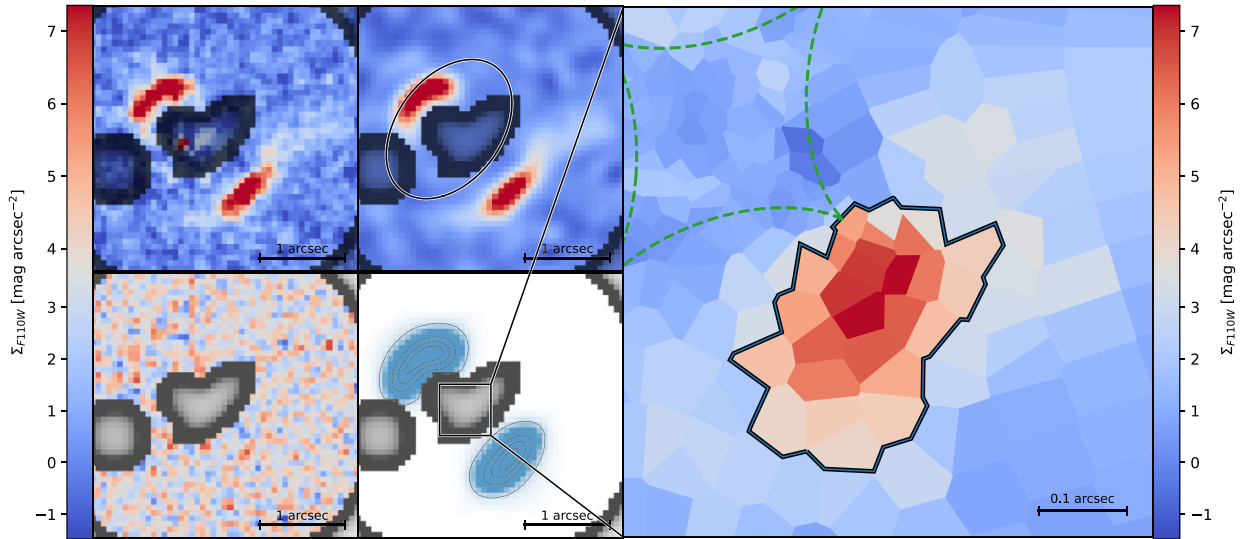
Figure 11. Left panels: lens-subtracted image (top left panel), best-fitting background lensed source (top right panel), SNR residual map (bottom left panel), and SNR > 3 regions of the source plane lensed back to the image plane of S_7. Each panel shows the pixel mask (corresponding to the black-shaded regions) adopted for the lens modelling. The top right panel shows the critical curves (continous line). The bottom right panel show the region of the source plane displayed in the right panel. Right panel: source plane reconstruction of the background source and caustics curves (dashed line). We highlight with a thicker contour the SNR > 3 region adopted for computing the lensing magnification and source size.

are multiple sources. The present analysis alone is not enough to determine whether these morphologies indicate different populations of DSFGs or variations in the stellar and/or dust distributions. The physical sizes of the background sources, measured as the circularized radii of the circles equivalent to the regions of the source plane with SNR > 3, range between 0.34 kpc (1st percentile) and 1.30 kpc (99th percentile). We compare our stellar sizes with the dust ones by Enia et al. (2018), who modelled the SMA sub-mm/mm emission of a sample of 12 lenses similarly selected and partially included in our sample. They found dust sizes between 1.52 kpc (1st percentile) and 4.07 kpc (99th percentile). We can understand this result by considering that the *HST* observations, by sampling the optical/near-UV rest-frame emission, are expected to pick up only the intrinsically brightest and more compact regions of the background sources whose light can pass through the dust. This is consistent with an inside-out growth and later inside-out quenching, a scenario where the central regions of these DSFGs begin to clear out the dust first, causing the more compact stellar emission to shine through. Interestingly, the *HST* sizes are comparable to bright nuclei and off-nuclear knots in local ultra-luminous infrared galaxies (ULIRGs; Surace et al. 1998; Farrah et al. 2001). This is somewhat in contrast with previous literature (e.g. Pantoni et al. 2021) that argued for the dust emission to be more compact than the stellar one. Although, recently, Kamieneski et al. (2023b) studied a $z \sim$ 2.3 lensed galaxies with properties similar to those of the lensed DSFGs in our sample and found rest frame near-UV/optical/near-IR emitting regions comparable or even slightly smaller in size than the ones measured in the sub-mm, thus providing evidence for an inside-out quenching scenario. It is worth noticing that Kamieneski et al. (2023b) has also considered another possible, but less likely, explanation related to inclination effects and uneven dust distribution. We also want to point out that the difference in sizes we observe between the stellar emitting region, as sampled by *HST*, and the dust-emitting region, as probed by SMA, may be affected by the lower angular resolution of the SMA observations compared to *HST* data. In fact, by projecting the half width at half maximum (HWHM)

of the SMA beam to the redshift of the source and then dividing it by the square root of the total magnification within the $>3\sigma$ regions, we get a physical resolution (once averaged over the whole sample) of 0.85 kpc, which is larger than what we get for near-IR size for about 50 per cent of our sample. While Enia et al. (2018) sources are resolved ($R_{\text{bkg, circ}}/\text{PSF}_{\text{HWHM}} \gtrsim 1$), any emission coming from regions smaller than the projected HWHM would inevitably be broadened. Moreover, the depth of our observations does not allow us to exclude that other, more obscured and undetected, star-forming knots are present throughout the disc, implying that mass buildup could happen disc-wide.

Finally, it is worth mentioning that the optical/near-IR sizes quoted in the literature are often measured through the effective radius obtained by fitting a Sérsic profile to the surface brightness distribution of the background sources. For lensed galaxies, this is usually done directly during the lens modelling by including a parametric background source (e.g. Calanog et al. 2014). Such an estimate of size takes into account the concentration of the source and averages out the surface brightness distribution in the case of clumpy emission. In comparison, our measure is SNR-dependent and is not affected by the smoothness of the surface brightness distribution. We remark that the relation between the observed-frame near-IR sizes and sub-mm ones is still up to debate and could depend on additional factors we do not discuss here, like the stellar mass of the galaxy (see Liu, Morishita & Kodama 2023, for details) or its evolutionary stage. At the same time, we find magnifications ranging between 2.4 (1st percentile) and 15.8 (99th percentile), with a median of 5.5 for our sample. The magnifications by Enia et al. (2018) range between 3.20 (1st percentile) and 8.35 (99th percentile) with a median of 5.7. This comparison suggests a minor, or even negligible, differential magnification.

We compare the properties of our lenses (i.e. total effective radii, Einstein radii, and total effective surface brightnesses) to those of the SLACS sample of confirmed lenses (Bolton et al. 2008). This is the largest available sample of strong lenses followed up by *HST* and with lens modelling. The SLACS lensing candidates were identified

Table 7. Results of the lens modelling.

No. (1)	IAU name (2)	δx [arcsec] / δx_0 [kpc] (3)	δy [arcsec] / δy_0 [kpc] (4)	θ_E [arcsec] / $\theta_{E,0}$ [kpc] (5)	q (6)	PA (7)	$\epsilon_{shear,1}$ (8)	$\epsilon_{shear,2}$ (9)	x_{pix} (10)	y_{pix} (11)	λ (12)	μ (13)	$R_{bkg,circ}$ [arcsec] / $R_{bkg,circ,0}$ [kpc] (14)	κ_0 [] / M [$10^{11}\,M_\odot$] (15)	M/L (16)
S.1	HATLASJ000330.6 − 321136	$-0.13^{+0.03}_{-0.02}$ / $-0.65^{+0.19}_{-0.16}$	$-0.05^{+0.01}_{-0.02}$ / $-0.24^{+0.08}_{-0.12}$	$0.733^{+0.006}_{-0.009}$ / $3.85^{+0.61}_{-0.85}$	0.85 ± 0.03	$80.11^{+3.78}_{-10.85}$	–	–	39^{+3}_{-9}	33^{+8}_{-7}	$0.0101^{+0.0011}_{-0.0009}$	$5.48^{+0.62}_{-0.48}$	$0.052^{+0.006}_{-0.004}$ / $0.41^{+0.04}_{-0.03}$	$1.68^{+0.03}_{-0.04}$ / $0.92^{+0.23}_{-0.28}$	– / $2.93^{+1.65}_{-0.98}$
S.3	HELMSJ001353.5 − 060200	$-0.038^{+0.004}_{-0.004}$ / $-0.26^{+0.05}_{-0.08}$	$0.066^{+0.004}_{-0.006}$ / $0.45^{+0.07}_{-0.08}$	$0.658^{+0.004}_{-0.003}$ / $4.56^{+0.50}_{-0.74}$	$0.85^{+0.03}_{-0.04}$	$-49.56^{+8.51}_{-8.32}$	$0.017^{+0.008}_{-0.010}$	0.191 ± 0.009	40 ± 4	31 ± 9	0.0084 ± 0.0006	$10.37^{+0.47}_{-0.56}$	0.052 ± 0.002 / 0.45 ± 0.02	$1.49^{+0.02}_{-0.01}$ / $1.48^{+0.52}_{-0.44}$	– / $4.19^{+3.00}_{-1.48}$
S.4	HELMSJ003619.8 + 002420	$-0.015^{+0.002}_{-0.001}$	$0.122^{+0.001}_{-0.002}$	$1.9349^{+0.0017}_{-0.0008}$	$0.813^{+0.001}_{-0.003}$	$-79.38^{+0.23}_{-0.21}$	–	–	36	40	$0.0164^{+0.0009}_{-0.0008}$	$15.82^{+1.23}_{-0.72}$	$0.143^{+0.006}_{-0.008}$	12.16 ± 0.3	–
S.7	HERSJ012620.5 + 012950	$-0.063^{+0.007}_{-0.005}$ / $-0.006^{+0.015}_{-0.007}$	$0.504^{+0.006}_{-0.008}$ / $0.14^{+0.01}_{-0.02}$	$7.97^{+0.007}_{-0.004}$ / 0.766 ± 0.004	$0.60^{+0.07}_{-0.03}$	$52.13^{+0.85}_{-0.58}$	–	–	31^{+4}_{-0}	40^{+4}_{-7}	$1.25^{+0.06}_{-0.07}$ / 0.0114 ± 0.0006	5.234 ± 0.001 / $5.19^{+0.56}_{-0.20}$	$3.40^{+0.68}_{-0.54}$ / $0.142^{+0.003}_{-0.010}$	$1.73^{+0.02}_{-0.01}$ / $1.32^{+0.18}_{-0.17}$	– / $2.36^{+0.73}_{-0.54}$
S.8	HERSJ020941.2 + 001558	$-0.259^{+0.005}_{-0.010}$ / $-0.89^{+0.02}_{-0.03}$	$0.046^{+0.008}_{-0.002}$ / $0.159^{+0.028}_{-0.006}$	$2.579^{+0.002}_{-0.003}$ / $8.844^{+0.007}_{-0.011}$	$0.704^{+0.003}_{-0.004}$	$-10.81^{+0.55}_{-0.21}$	–	–	43	43	0.0093 ± 0.0004	$7.29^{+0.30}_{-0.10}$	0.158 ± 0.003 / 1.30 ± 0.03	$18.61^{+0.08}_{-0.19}$ / $5.99^{+0.03}_{-0.06}$	– / $4.96^{+0.95}_{-0.77}$
S.9	HERMESJ032637 − 270044	$0.024^{+0.009}_{-0.013}$ / –	-0.12 ± 0.01 / –	$0.981^{+0.005}_{-0.006}$ / –	0.87 ± 0.01	$-40.54^{+1.64}_{-2.25}$	–	–	42^{+0}_{-9}	28^{+11}_{-5}	$0.0110^{+0.0010}_{-0.0009}$	$6.15^{+0.32}_{-0.38}$	0.072 ± 0.004	$3.01^{+0.03}_{-0.04}$	–
S.10	HERMESJ033732 − 295353	$0.1754^{+0.0007}_{-0.0005}$ / $0.57^{+0.11}_{-0.12}$	$0.0576^{+0.0012}_{-0.0008}$ / $0.18^{+0.04}_{-0.05}$	$1.9718^{+0.0003}_{-0.0006}$ / $6.40^{+1.18}_{-1.30}$	$0.6495^{+0.0003}_{-0.0006}$	$-80.49^{+0.04}_{-0.15}$	–	–	41	38	$0.0057^{+0.0002}_{-0.0003}$	$6.27^{+0.50}_{-0.05}$	$0.0801^{+0.0045}_{-0.0002}$	$11.662^{+0.004}_{-0.007}$	–
S.12	HERMESJ100144 + 025709	$-0.033^{+0.003}_{-0.004}$ / $-0.26^{+0.02}_{-0.03}$	$0.042^{+0.009}_{-0.003}$ / $0.34^{+0.08}_{-0.02}$	0.930 ± 0.002 / $7.94^{+0.50}_{-0.66}$	$0.686^{+0.006}_{-0.008}$	$-16.66^{+0.39}_{-0.56}$	–	–	33^{+11}_{-10}	30^{+9}_{-0}	$0.0076^{+0.0004}_{-0.0003}$	$6.33^{+0.15}_{-0.17}$	$0.094^{+0.002}_{-0.001}$	2.63 ± 0.02	–
S.13	HERMESJ103827 + 581544	$0.228^{+0.016}_{-0.006}$	0.27 ± 0.01	2.408 ± 0.010 / 16.47 ± 0.07	0.582 ± 0.007	$-70.47^{+0.76}_{-0.47}$	–	–	44	44	0.025 ± 0.002	$4.29^{+0.15}_{-0.25}$	$0.17^{+0.02}_{-0.01}$	15.68 ± 0.4	–
S.14	HERMESJ110016 + 571736	$1.56^{+0.11}_{-0.10}$ / $-0.324^{+0.007}_{-0.009}$ / $-2.48^{+0.05}_{-0.07}$	$1.84^{+0.09}_{-0.10}$ / $-0.251^{+0.007}_{-0.011}$ / $-1.92^{+0.02}_{-0.08}$	1.081 ± 0.003 / $8.28^{+0.02}_{-0.03}$	0.71 ± 0.01	$11.63^{+1.13}_{-0.88}$	–	–	32^{+5}_{-7}	42^{+1}_{-0}	$0.0151^{+0.0008}_{-0.0009}$	$2.43^{+0.03}_{-0.04}$	$0.211^{+0.004}_{-0.006}$ / $1.84^{+0.04}_{-0.06}$	3.56 ± 0.02 / $5.39^{+0.03}_{-0.04}$	– / $1.95^{+0.10}_{-0.09}$
S.16	HATLASJ125126 + 254928	-0.40 ± 0.02 / $-2.75^{+0.24}_{-0.23}$	$0.056^{+0.009}_{-0.014}$ / $0.38^{+0.08}_{-0.09}$	$1.133^{+0.016}_{-0.007}$ / $7.94^{+0.50}_{-0.66}$	$0.58^{+0.01}_{-0.02}$	$20.05^{+2.41}_{-3.88}$	–	–	39 ± 3	37^{+5}_{-9}	0.015 ± 0.002	$5.10^{+0.37}_{-0.67}$	$0.052^{+0.006}_{-0.005}$ / 0.39 ± 0.04	$3.73^{+0.13}_{-0.04}$ / $3.20^{+0.45}_{-0.46}$	– / $3.29^{+1.07}_{-0.72}$
S.17	HATLASJ125760 + 224558	$0.104^{+0.012}_{-0.007}$ / $0.69^{+0.08}_{-0.04}$	$-0.06^{+0.01}_{-0.04}$ / $-0.40^{+0.08}_{-0.30}$	$0.681^{+0.005}_{-0.006}$ / $4.52^{+0.03}_{-0.04}$	$0.70^{+0.07}_{-0.02}$	$60.10^{+1.21}_{-2.50}$	–	–	38	43	0.0059 ± 0.0004	$4.46^{+0.56}_{-0.52}$	$0.081^{+0.006}_{-0.005}$ / $0.70^{+0.05}_{-0.04}$	$1.41^{+0.04}_{-0.03}$ / $1.43^{+0.22}_{-0.13}$	– / $1.74^{+0.28}_{-0.17}$
S.18	HATLASJ133008 + 245860	$0.037^{+0.003}_{-0.010}$ / –	$-0.287^{+0.010}_{-0.005}$ / –	$1.037^{+0.001}_{-0.002}$ / –	$0.616^{+0.009}_{-0.007}$	$-14.02^{+0.61}_{-0.43}$	–	–	39^{+2}_{-5}	36^{+7}_{-5}	0.0084 ± 0.0006	$12.31^{+1.10}_{-0.72}$	0.055 ± 0.003	$3.184^{+0.009}_{-0.008}$	–

Table 7 – *continued*

No.	IAU name	δx [arcsec] / δx_0 [kpc]	δy [arcsec] / δy_0 [kpc]	θ_E [arcsec] / $\theta_{E,0}$ [kpc]	q	PA	$\epsilon_{shear,1}$	$\epsilon_{shear,2}$	x_{pix}	y_{pix}	λ	μ	$R_{bkg,circ}$ [arcsec] / $R_{bkg,circ,0}$ [kpc]	κ_0 [] / M [$10^{11}\,M_\odot$]	M/L
(1)	(2)	(3)	(4)	(5)	(6)	(7)	(8)	(9)	(10)	(11)	(12)	(13)	(14)	(15)	(16)
S.19	HATLASJ133846 + 255057	$0.21^{+0.02}_{-0.06}$	$-1.65^{+0.06}_{-0.03}$	$5.974^{+0.009}_{-0.011}$	$0.895^{+0.002}_{-0.011}$	$79.56^{+0.59}_{-0.58}$	$0.281^{+0.008}_{-0.001}$	$-0.0560^{+0.0024}_{-0.0002}$	42	41	$0.0046^{+0.0003}_{-0.0002}$	$3.78^{+0.04}_{-0.02}$	0.43 ± 0.02	$1.990^{+0.006}_{-0.005}$	$3.47^{+1.14}_{-0.80}$
		$0.0905^{+0.0005}_{-0.0028}$	$-0.1092^{+0.0001}_{-0.0008}$	$0.6697^{+0.0004}_{-0.0002}$									$0.0963^{+0.0006}_{-0.0008}$	$1.706^{+0.012}_{-0.002}$	—
S.21	HERMESJ171451 + 592634	$0.51^{+0.07}_{-0.08}$	$-0.63^{+0.10}_{-0.08}$	$3.83^{+0.48}_{-0.62}$	0.72 ± 0.02	$-76.63^{+1.34}_{-0.90}$	—	—	42^{+1}_{-6}	35^{+5}_{-2}	0.012 ± 0.001	$8.40^{+5.93}_{-6.00}$	0.80 ± 0.03	1.12 ± 0.26	$7.95^{+3.82}_{-2.14}$
		$-0.23^{+0.05}_{-0.01}$	$0.21^{+0.03}_{-0.01}$	$0.976^{+0.006}_{-0.007}$									$0.053^{+0.053}_{-0.009}$	$2.46^{+0.02}_{-0.01}$	$2.83^{+0.18}_{-0.17}$
		$-2.01^{+0.39}_{-0.09}$	$1.80^{+0.27}_{-0.02}$	$8.35^{+0.05}_{-0.06}$									$0.41^{+0.41}_{-0.07}$	4.1435 ± 0.0008	—
S.29	HERSJ012041.6 − 002705	-0.07 ± 0.01	$-0.095^{+0.005}_{-0.011}$	$0.928^{+0.005}_{-0.006}$	$0.76^{+0.02}_{-0.01}$	$-41.77^{+2.16}_{-2.17}$	—	—	38^{+5}_{-6}	35 ± 6	0.022 ± 0.002	$3.91^{+0.43}_{-0.34}$	$0.124^{+0.008}_{-0.006}$	2.65 ± 0.03	—
		$-0.55^{+0.08}_{-0.09}$	$-0.71^{+0.08}$	6.94 ± 0.15											
S.30	HATLASJ085112 + 004934	$0.03406^{+0.00009}_{-0.00014}$	$0.1967^{+0.0010}_{-0.0002}$	$1.24359^{+0.00004}_{-0.00003}$	$0.34221^{+0.00034}_{-0.00007}$	$-41.033^{+0.008}_{-0.033}$	$-0.29461^{+0.00011}_{-0.00006}$	$0.28098^{+0.00005}_{-0.00043}$	44	44	$0.00112^{+0.00004}_{-0.00005}$	$27.80^{+0.50}_{-0.59}$	$0.01863^{+0.00004}_{-0.00009}$	$4.0578^{+0.0014}_{-0.0003}$	—
S.32	HERMESJ104549 + 574512	$0.24^{+0.03}_{-0.07}$	$1.41^{+0.20}_{-0.39}$	$8.90^{+1.26}_{-2.45}$	$0.677^{+0.005}_{-0.003}$	$18.85^{+0.69}_{-0.23}$	—	—	41	40 ± 4	0.014 ± 0.001	$8.63^{+0.37}_{-0.21}$	$0.161^{+0.001}_{-0.004}$	$4.60^{+3.73}_{-2.22}$	$1.86^{+2.07}_{-0.72}$
		$-0.47^{+0.03}_{-0.04}$	$-0.129^{+0.006}_{-0.009}$	$2.631^{+0.007}_{-0.012}$									0.108 ± 0.002	$17.23^{+0.21}_{-0.12}$	
		$-1.59^{+0.15}_{-0.17}$	-0.44 ± 0.04	$8.97^{+0.67}_{-0.73}$									0.85 ± 0.02	$5.45^{+0.50}_{-0.52}$	
S.35	HATLASJ132630 + 334410	$0.004^{+0.004}_{-0.006}$	$-0.057^{+0.009}_{-0.013}$	$1.684^{+0.005}_{-0.004}$	$0.577^{+0.008}_{-0.006}$	$-47.54^{+0.42}_{-0.40}$	—	—	42^{+2}_{-4}	34^{+8}_{-2}	0.0095 ± 0.0006	1.89 ± 0.02	$0.0938^{+0.0079}_{-0.0004}$	$8.26^{+0.03}_{-0.02}$	$63.80^{+12.97}_{-10.76}$
		$0.03^{+0.03}_{-0.05}$	$-0.44^{+0.07}_{-0.10}$	$12.92^{+0.04}_{-0.03}$									$0.743^{+0.063}_{-0.003}$	9.09 ± 0.03	$3.83^{+0.20}_{-0.19}$
S.38	HERMESJ142824 + 352620	$-0.0008^{+0.0065}_{-0.0074}$	$0.016^{+0.005}_{-0.006}$	$0.215^{+0.006}_{-0.003}$	$0.66^{+0.06}_{-0.05}$	$-5.44^{+5.95}_{-8.75}$	—	—	42^{+1}_{-8}	25^{+5}_{-4}	$0.0064^{+0.0006}_{-0.0004}$	$2.64^{+0.15}_{-0.14}$	$0.090^{+0.003}_{-0.004}$	$0.137^{+0.010}_{-0.005}$	$0.98^{+0.11}_{-0.09}$
		$-0.007^{+0.054}_{-0.061}$	$0.13^{+0.04}_{-0.05}$	$1.78^{+0.05}_{-0.03}$									0.78 ± 0.03	$0.58^{+0.04}_{-0.02}$	
S.39	HATLASJ223753.8 − 305828	$0.19^{+0.02}_{-0.01}$	$-0.091^{+0.010}_{-0.017}$	$1.26^{+0.02}_{-0.01}$	$0.54^{+0.01}_{-0.03}$	$65.49^{+0.77}_{-0.62}$	—	—	44	20	$0.0098^{+0.0006}_{-0.0005}$	$2.65^{+0.04}_{-0.10}$	$0.1281^{+0.0032}_{-0.0010}$	$4.53^{+0.07}_{-0.05}$	$4.00^{+2.08}_{-1.12}$
		$1.24^{+0.18}_{-0.20}$	$-0.60^{+0.11}_{-0.13}$	$8.28^{+1.90}_{-1.31}$									1.10 ± 0.03	$3.88^{+1.15}_{-1.02}$	
S.40	HATLASJ225250.7 − 313657	$0.182^{+0.012}_{-0.005}$	$0.08^{+0.01}_{-0.02}$	$0.605^{+0.008}_{-0.004}$	$0.633^{+0.020}_{-0.009}$	$-73.84^{+2.35}_{-0.69}$	—	—	41^{+3}_{-9}	40^{+4}_{-14}	$0.0031^{+0.0002}_{-0.0003}$	$3.44^{+0.18}_{-0.11}$	$0.078^{+0.002}_{-0.003}$	$1.09^{+0.03}_{-0.01}$	—
		$1.33^{+0.17}_{-0.27}$	$0.54^{+0.14}_{-0.18}$	$4.41^{+0.51}_{-0.89}$									0.65 ± 0.02		
S.41	HELMSJ233633.5 − 032119	$0.051^{+0.001}_{-0.005}$	$-0.0851^{+0.0106}_{-0.0004}$	$1.7281^{+0.0130}_{-0.0007}$	$0.7347^{+0.0008}_{-0.0196}$	$-48.44^{+1.47}_{-0.11}$	—	—	39	43	$0.0084^{+0.0005}_{-0.0004}$	$12.39^{+2.16}_{-2.48}$	$0.036^{+0.011}_{-0.005}$	$1.12^{+0.47}_{-0.40}$	$4.89^{+4.71}_{-1.81}$
		—	—	—									$0.30^{+0.10}_{-0.05}$	$9.161^{+0.105}_{-0.006}$	—

Notes. Column (1): source reference number. Column (2): IAU name of the *Herschel* detection. Columns (3) and (4): RA and Dec. offsets in arcsec (first row) and kpc (second row). Column (5): Einstein radius in arcsec (first row) and kpc (second row). Column (6): axis ratio of the mass profile. Column (7): position angle of the mass profile. Columns (8) and (9): shear elliptical components of the mass profile. Columns (10) and (11): size of the source plane pixelization. Column (12): regularization coefficient. Column (13): magnification computed on the regions of the source plane with SNR > 3. Column (14): circularized radius equivalent to the regions of the source plane with SNR > 3. Column (15): mass within the Einstein radius. Column (16): mass-to-light ratio in *F*110W within the Einstein radius.

Table 8. Comparison between our Einstein radii and those available in the literature in the near-IR and in the sub-mm/mm if available.

No.	IAU name	θ_E [arcsec]	$\theta_{E, near-IRlit.}$ [arcsec]	Ref.	$\theta_{E, sub-mm/mm.lit.}$ [arcsec]	Ref.	Multiw.	Ref
(1)	(2)	(3)	(4)	(5)	(6)	(7)	(8)	(9)
S_8	HERSJ020941.2 + 001558	$2.579^{+0.002}_{-0.003}$	$2.48^{+0.02}_{-0.01}$	Ge15	$2.55^{+0.14}_{-0.20}$	Ka23	ALMA band 6	Li22
S_9	HERMESJ032637 − 270044	$0.981^{+0.005}_{-0.006}$	$0.96^{+0.02}_{-0.03}$	Ca14	–	–	–	–
S_10	HERMESJ033732 − 295353	$1.9718^{+0.0004}_{-0.0005}$	$1.65^{+0.03}_{-0.054}$	Ca14	–	–	–	–
S_12	HERMESJ100144 − 025709	0.930 ± 0.002	0.91 ± 0.01	Ca14	0.956 ± 0.005	Bu15	ALMA band 7	Bu15
S_13	HERMESJ103827 + 581544	2.408 ± 0.010	$2.40^{+0.01}_{-0.05}$	Ca14	2.0 ± 0.2	Bu13	SMA 340 GHz	Bu13
S_14	HERMESJ110016 + 571736	1.081 ± 0.003	$1.14^{+0.04}_{-0.07}$	Ca14	–	–	–	–
S_18	HATLASJ133008 + 24586	1.037 ± 0.002	$0.944^{+0.002}_{-0.001}$	Ca14	0.88 ± 0.02	Bu13	SMA 340 GHz	Bu13
S_21	HERMESJ171451 + 592634	$0.976^{+0.006}_{-0.007}$	$0.87^{+0.02}_{-0.05}$	Ca14	–	–	–	–
S_32	HERMESJ104549 + 574512	$2.631^{+0.008}_{-0.012}$	2.46 ± 0.01	Ca14	–	–	–	–
S_35	HATLASJ132630 + 334410	$1.684^{+0.005}_{-0.004}$	–	–	1.80 ± 0.02	Bu13	SMA 340 GHz	Bu13
S_38	HERMESJ142824 + 35262	0.37 ± 0.02	–	–	0.10 ± 0.03	Bu13	SMA 340 GHz	Bu13

Notes. Column (1): source reference number. Column (2): IAU name of the *Herschel* detection. Column (3): value of the Einstein radii measured in this work. Columns (4) and (5): value of the Einstein radii measured in the literature from the near-IR observations and reference. Columns (6) and (7): value of the Einstein radii measured in the literature from the sub-mm/mm observations and reference. Columns (8) and (9): multiwavelength observations and reference.
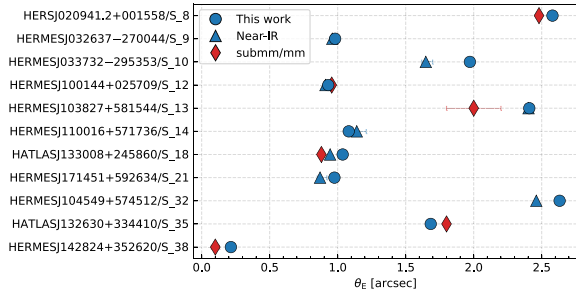
Figure 12. Comparison between our estimated Einstein radii (circles) and the ones from literature measured either in near-IR (triangles) or sub-mm/mm (diamonds).

from archival SDSS spectroscopic data as all the systems that show the presence of two separate redshift estimates in the same spectrum: a lower absorption-line redshift for the foreground lens and a higher emission-line redshift for the background source. These candidates were then followed up and confirmed by means of *HST ACS/F814W* imaging. We consider the 63 confirmed lenses out of 131 candidates, for which Bolton et al. (2008) were able to subtract the surface brightness distribution of the foreground lens and perform the lens modelling. They modelled the surface brightness distribution of the lens, adopting the de Vaucouleurs profile. We perform a *K*-correction of the total effective surface brightness of all the galaxies of our and SLACS samples with available redshifts. As a template for the ETG SED, we use the 17 local elliptical galaxies available in the Brown Atlas (Brown et al. 2014). To estimate the *F110W* magnitude of the SLACS lenses, we redshift and normalize the template to match the *F814W* magnitude using PYSYNPHOT package.[13] Then, we compute the *F110W* magnitude of each template at $z = 0$ and at the redshift of the foreground lenses of both samples. Finally, we adopt the *F110W* magnitude difference as the *K*-correction term. This correction does not take into account possible differences between the SEDs of the templates and the ones of the lenses. The median *K*-correction terms for our sample and SLACS are 0.04

[13] https://pysynphot.readthedocs.io/en/latest/
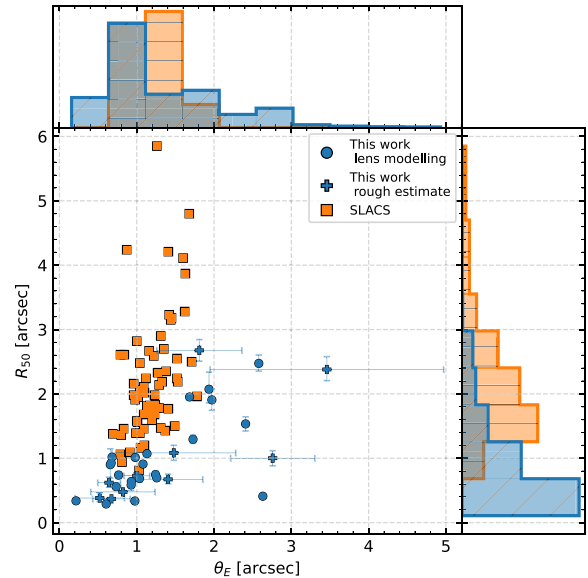
Figure 13. Top panel: normalized distribution of the values of the Einstein radius of the lenses in our (diagonally hatched histogram) and in the SLACS samples (horizontally hatched histogram). Bottom left panel: total effective radius as a function of Einstein radius of the lenses in our (circles) and in the SLACS sample (squares). The circles and crosses correspond to systems for which we derived the Einstein radius from the lens modelling or the separation between multiple images, respectively. Bottom right panel: normalized distribution of the values of the total effective radius of the lenses.

and 0.03 mag, respectively. From Fig. 13, it is possible to see that our sample shows different R_{50} and θ_E distributions than SLACS. Our selection is able to pick up more systems with both smaller or larger values of θ_E. Moreover, at similar Einstein radii, the effective radii of our lenses are significantly smaller than the SLACS, making our background sources less contaminated by the emission of the lenses. Fig. 14 shows that the two samples have similar $R_{50,0}$ and absolute magnitude distributions, although our lenses show a tail for smaller and fainter galaxies. At the same time, our lenses have lower $\mu_{50,0,Kcorr}$ for the same radii, which implies that our lenses either are
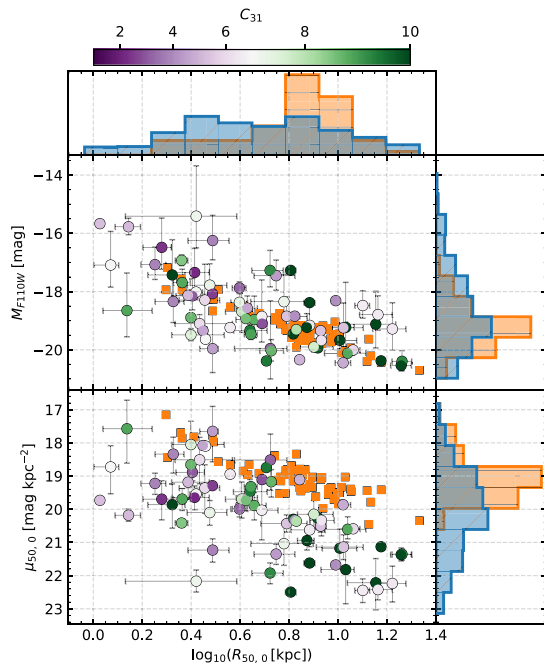
Figure 14. Top panel: normalized distribution of the total effective radii in kpc of our (diagonally hatched histogram) and SLACS samples (horizontally hatched histogram). Central left panel: absolute magnitude corrected for K-correction against the total effective radii in kpc of the two samples. Central right panel: normalized distribution of the absolute magnitude of the two samples with the K-correction applied. Our lensing galaxies are colour-coded according to their concentration. The colourbar is normalised such that the concentration of a de Vaucouleurs profile falls in the middle. Bottom left panel: Kormendy relation of the two samples. Our lensing galaxies are colour-coded according to their concentration. Bottom right panel: normalized distribution of the total effective surface brightness of the two samples with the K-correction applied.

fainter or more concentrated than the de Vaucouleurs profiles. The increased scatter we find in both the $R_{50,0}$ and M_{F110W}, and $R_{50,0}$ and $\mu_{50,0,\mathrm{K_{corr}}}$ distributions can be accounted for by considering the variation in concentration and the wide range of foreground lens redshifts we observed. We can try to further explain these differences by considering the different selections of the two samples. The SLACS sample, being constructed from SDSS spectroscopic data and needing a robust detection of both the foreground lens and background source, is limited in magnitude to brighter lenses at lower redshift. In particular, the SLACS spectroscopic selection was done through 3 arcsec diameter fibres and comprises either local galaxies or massive ETGs at $z \lesssim 0.6$.

7 CONCLUSIONS

We have carried out a snapshot *HST* F110W observing campaign to follow-up 281 *Herschel*-selected candidate strongly lensed galaxies. We visually inspect them and classify them according to the presence of the background sources, confirming 25 candidates as strong lenses. We model all the systems where we identify a suitable lens candidate exploiting three different surface brightness modelling algorithms, namely GASP2D, GALFIT, and ISOFIT + CMODEL, based on the morphology of the foreground lensing galaxies. By combining the visual inspection, available multiwavelength follow-ups, and results of the lens subtraction, we are able to confirm as lensed a

total of 65 systems. Lastly, we perform lens modelling and source reconstruction of all the systems for which we can confidently identify both a galaxy acting as the main lens and the background source in the *HST* images (34 systems). We obtain successful results for 23 galaxies. The main results of our analysis are the following:

(i) the overall surface brightness distribution of the lenses and their morphology follows the relations expected for ETGs; however, the foreground lensing galaxies often needed multiple surface brightness components, with properties significantly varying from galaxy to galaxy;

(ii) most of the lensing systems are consistent with single galaxy lenses, with only ~ 7 per cent of them being confirmed as a group or cluster lenses;

(iii) the estimated magnifications and Einstein radii are consistent with previous analysis conducted on data at different wavelengths; however, the inferred size of the background sources is about three times smaller than the ones measured in the sub-mm/mm with SMA by Enia et al. ([2018](#)) for a similarly selected, and partially overlapping sample. This difference in size between the stellar and the dust-emitting regions is suggestive of an inside-out quenching scenario;

(iv) the sub-mm selection used to build our sample revealed lensing systems with fainter lenses and larger Einstein radii than the SLACS survey.

To conclude, we point out that the *HST* snapshots alone, even after carefully identifying and subtracting the candidate lenses, might miss some of the fainter lensed background sources. We argue that this is due to their dust obscuration and high redshift. This underlines the importance of dedicated, deeper near-IR observations (e.g. with *HST*, Keck, *Euclid* or *JWST*) and high-resolution sub-mm observations (e.g. with ALMA and NOEMA) to effectively determine the nature of the majority of *Herschel*-selected strong lensing candidates. This work provides the basis for further detailed analysis of the background sources by allowing not only more complex lens modelling but also providing constraints on the stellar content through SED-fitting techniques.

DATA AVAILABILITY

The reduced images, models, residuals, and PSF cutouts are available on Zenodo at the following link https://doi.org/10.5281/zenodo.100 07041 (Borsato et al. 2023). Future versions will be available at https://zenodo.org/doi/10.5281/zenodo.10007040.

REFERENCES

Aguirre P. et al., 2018, ApJ, 855, 26
Albareti F. D. et al., 2017, ApJS, 233, 25
Amvrosiadis A. et al., 2018, MNRAS, 475, 4939
Asboth V. et al., 2016, MNRAS, 462, 1989
Astropy Collaboration, 2018, AJ, 156, 123
Astropy Collaboration, 2013, A&A, 558, A33
Auger M. W., Treu T., Bolton A. S., Gavazzi R., Koopmans L. V. E., Marshall P. J., Bundy K., Moustakas L. A., 2009, ApJ, 705, 1099
Bakx T. J. L. C. et al., 2018, MNRAS, 473, 1751
Bakx T. J. L. C. et al., 2020, MNRAS, 496, 2372
Beers T. C., Flynn K., Gebhardt K., 1990, AJ, 100, 32
Berman D. A. et al., 2022, MNRAS, 515, 3911
Berta S. et al., 2021, A&A, 646, A122
Bolton A. S., Burles S., Koopmans L. V. E., Treu T., Gavazzi R., Moustakas L. A., Wayth R., Schlegel D. J., 2008, ApJ, 682, 964
Borsato, E., Corsini E. M., Marchetti, L., Negrello, M., 2023, Data products of the surface brightness modelling of the confirmed and candidates lenses in Borsato et al. 2023. (1.0 as presented in the paper) [Data set], Zenodo, doi:
Borys C. et al., 2006, ApJ, 636, 134
Bradley L. et al., 2021, astropy/photutils: 1.1.0, doi: (accessed June 2021)
Brown M. J. I. et al., 2014, ApJS, 212, 18
Bussmann R. S. et al., 2012, ApJ, 756, 134
Bussmann R. S. et al., 2013, ApJ, 779, 25
Bussmann R. S. et al., 2015, ApJ, 812, 43
Butler K. M. et al., 2021, ApJ, 919, 5
Cai Z.-Y. et al., 2013, ApJ, 768, 21
Cai Z.-Y., Negrello M., De Zotti G., 2022, ApJ, 932, 13
Calanog J. A. et al., 2014, ApJ, 797, 138
Cañameras R. et al., 2015, A&A, 581, A105
Cañameras R. et al., 2017, A&A, 604, A117
Carlstrom J. E. et al., 2011, PASP, 123, 568
Carrasco M. et al., 2017, ApJ, 834, 210
Champagne J. B. et al., 2021, ApJ, 913, 110
Ciambur B. C., 2015, ApJ, 810, 120
Cox P. et al., 2011, ApJ, 740, 63
Cox P. et al., 2023, A&A, 678, A26
Dalla Bontà E., Davies R. L., Houghton R. C. W., D'Eugenio F., Méndez-Abreu J., 2018, MNRAS, 474, 339
Díaz-Santos T. et al., 2021, A&A, 654, A37
Dressel L., 2022, WFC3 Instrument Handbook for Cycle 30 v. 14. STScI, Baltimore, MD
Dye S. et al., 2018, MNRAS, 476, 4383
Dye S. et al., 2022, MNRAS, 510, 3734
Eales S. et al., 2010, PASP, 122, 499
Enia A. et al., 2018, MNRAS, 475, 3467
Etherington A. et al., 2023, preprint (arXiv:2301.05244)
Everett W. B. et al., 2020, ApJ, 900, 55
Falgarone E. et al., 2017, Nature, 548, 430
Farrah D. et al., 2001, MNRAS, 326, 1333
Fu H. et al., 2012, ApJ, 753, 134
Gaia Collaboration, 2021, A&A, 649, A1
Gavazzi R. et al., 2011, ApJ, 738, 125
Geach J. E. et al., 2015, MNRAS, 452, 502
Giulietti M. et al., 2022, MNRAS, 511, 1408
Giulietti M. et al., 2023, ApJ, 943, 151
Gómez-Guijarro C. et al., 2019, ApJ, 872, 117
González-Nuevo J. et al., 2012, ApJ, 749, 65
González-Nuevo J. et al., 2019, A&A, 627, A31
Harrington K. C. et al., 2016, MNRAS, 458, 4383
Harris A. I. et al., 2012, ApJ, 752, 152
Hernán-Caballero A., Spoon H. W. W., Lebouteiller V., Rupke D. S. N., Barry D. P., 2016, MNRAS, 455, 1796
Hoffmann S. L., Mack J., Avila R., Martlin C., Cohen Y., Bajaj V., 2021, in American Astronomical Society Meeting Abstracts. p. 216.02
Ikarashi S. et al., 2011, MNRAS, 415, 3081
Ivison R. J. et al., 2013, ApJ, 772, 137
Jarugula S. et al., 2021, ApJ, 921, 97
Jedrzejewski R. I., 1987, MNRAS, 226, 747
Kamieneski P. S. et al., 2023a, preprint (arXiv:2301.09746)
Kamieneski P. S. et al., 2023b, ApJ, 955, 91
Lapi A., Negrello M., González-Nuevo J., Cai Z. Y., De Zotti G., Danese L., 2012, ApJ, 755, 46
Leung T. K. D. et al., 2019, ApJ, 871, 85
Lewis A. J. R. et al., 2018, ApJ, 862, 96
Liu B. et al., 2022, ApJ, 929, 41
Liu Z., Morishita T., Kodama T., 2023, ApJ, 955, 29
Ma J. et al., 2019, ApJS, 244, 30
Maddox S. J. et al., 2018, ApJS, 236, 30
Manjón-García A., Herranz D., Diego J. M., Bonavera L., González-Nuevo J., 2019, A&A, 622, A106
Maresca J. et al., 2022, MNRAS, 512, 2426
Méndez-Abreu J. et al., 2017, A&A, 598, A32
Méndez-Abreu J., Aguerri J. A. L., Corsini E. M., Simonneau E., 2008, A&A, 478, 353
Messias H. et al., 2014, A&A, 568, A92
Mocanu L. M. et al., 2013, ApJ, 779, 61
Nadadur D., Haralick R. M., 2000, IEEE Trans. Image Process., 9, 749
Nayyeri H. et al., 2016, ApJ, 823, 17
Nayyeri H. et al., 2017, ApJ, 844, 82
Negrello M. et al., 2010, Science, 330, 800
Negrello M. et al., 2014, MNRAS, 440, 1999
Negrello M. et al., 2017, MNRAS, 465, 3558
Negrello M., Perrotta F., González-Nuevo J., Silva L., de Zotti G., Granato G. L., Baccigalupi C., Danese L., 2007, MNRAS, 377, 1557
Neri R. et al., 2020, A&A, 635, A7

Nightingale J. et al., 2021, J. Open Source Softw, 6, 2825

Nightingale J. W., Dye S., Massey R. J., 2018, MNRAS, 478, 4738

Okido D. H., Furlanetto C., Trevisan M., Tergolina M., 2021, in Storchi Bergmann T., Forman W., Overzier R., Riffel R.eds, Proc. IAU Symp. 359, Galaxy Evolution and Feedback across Different Environments. Cambridge University Press, Cambridge, p. 188

Oliver S. J. et al., 2012, MNRAS, 424, 1614

Omont A. et al., 2013, A&A, 551, A115

Pantoni L. et al., 2021, MNRAS, 507, 3998

Peng C. Y., Ho L. C., Impey C. D., Rix H.-W., 2002, AJ, 124, 266

Peng C. Y., Ho L. C., Impey C. D., Rix H.-W., 2010, AJ, 139, 2097

Penney J. I. et al., 2020, MNRAS, 496, 1565

Perrotta F., Baccigalupi C., Bartelmann M., De Zotti G., Granato G. L., 2002, MNRAS, 329, 445

Pilbratt G. L. et al., 2010, A&A, 518, L1

Planck Collaboration VI, 2020, A&A, 641, A6

Ratzlaff K. L., Johnson J. T., 1989, Anal. Chem., 61, 1303

Renzini A., 2009, MNRAS, 398, L58

Reuter C. et al., 2020, ApJ, 902, 78

Rowan-Robinson M. et al., 2018, A&A, 619, A169

Shirley R. et al., 2021, MNRAS, 507, 129

Speagle J. S., 2020, MNRAS, 493, 3132

Spilker J. S. et al., 2016, ApJ, 826, 112

Stanford S. A., Gonzalez A. H., Brodwin M., Gettings D. P., Eisenhardt P. R. M., Stern D., Wylezalek D., 2014, ApJS, 213, 25

Su T. et al., 2017, MNRAS, 464, 968

Sun F. et al., 2021, ApJ, 908, 192

Surace J. A., Sanders D. B., Vacca W. D., Veilleux S., Mazzarella J. M., 1998, ApJ, 492, 116

Urquhart S. A. et al., 2022, MNRAS, 511, 3017

Valiante E. et al., 2016, MNRAS, 462, 3146

Vieira J. D. et al., 2010, ApJ, 719, 763

Vieira J. D. et al., 2013, Nature, 495, 344

Viero M. P. et al., 2014, ApJS, 210, 22

Wang T. et al., 2018, ApJ, 867, L29

Ward B. A. et al., 2022, MNRAS, 510, 2261

Wardlow J. L. et al., 2013, ApJ, 762, 59

Watkins A. E. et al., 2022, A&A, 660, A69

Yang C. et al., 2016, A&A, 595, A80

Yang C. et al., 2017, A&A, 608, A144

Yang C. et al., 2019, A&A, 624, A138

Zhang Z.-Y. et al., 2018, MNRAS, 481, 59

APPENDIX A: THE FULL 'A' SAMPLE
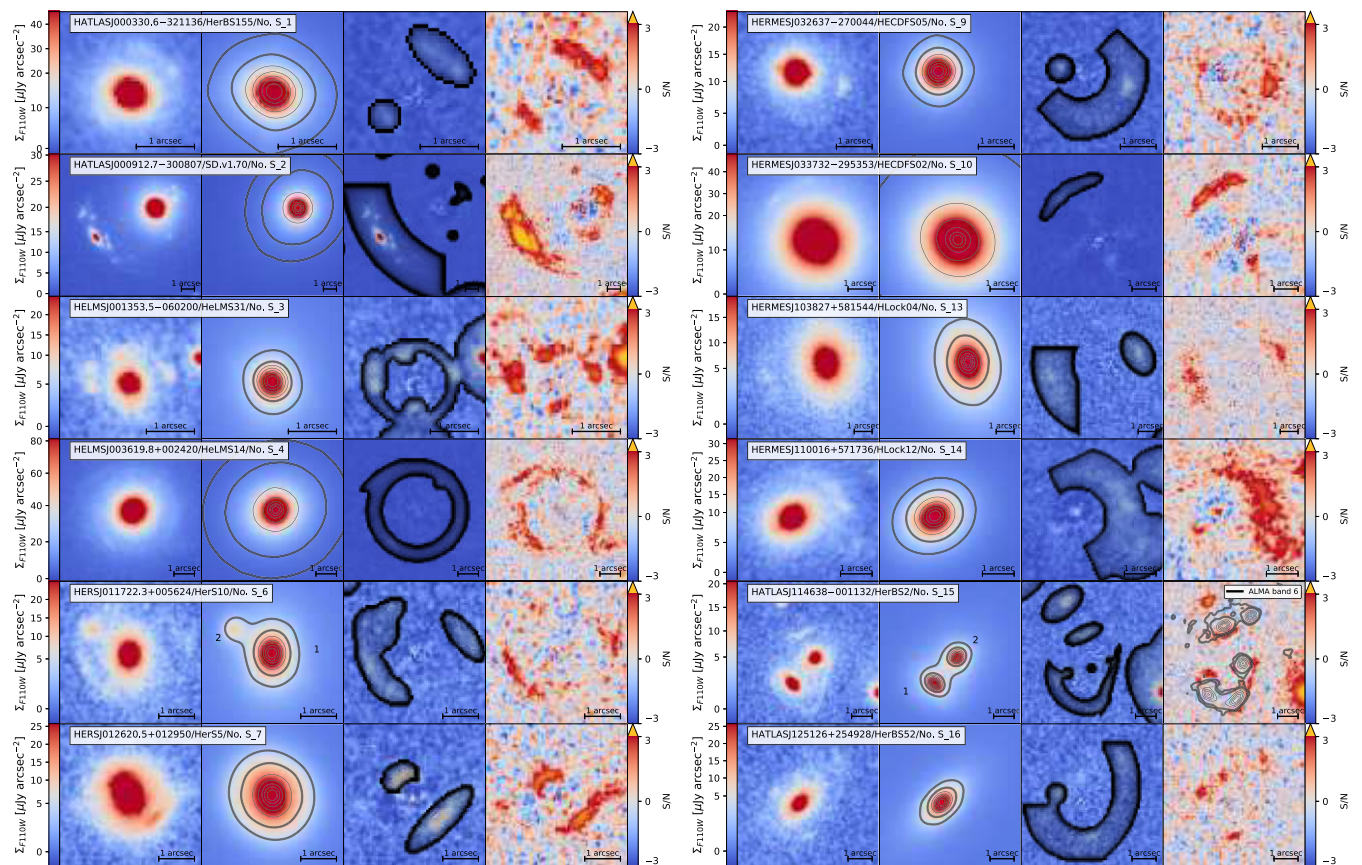
Figure A1. From left to right panels: observed *HST F110W* image, best-fitting surface brightness model of the lens, residual obtained after the subtraction of the lens model from the image, and SNR map of the residuals for the A class candidates. The contours in the model images are taken at two levels corresponding to SNR = 5 and 10 (thick curves), and five uniformly spaced levels between the SNR = 10 and the maximum SNR in the model image (thin curves). The residual map shows the pixel mask (corresponding to the black-shaded regions) adopted for the surface brightness modelling. The residual maps show the contours of available high-resolution multiwavelength data taken at two levels corresponding to SNR = 5 and 10 (thick curves), and five uniformly spaced levels between the SNR = 10 and the maximum SNR in the multiwavelength image (thin black curves). The images are oriented such that N is up and E is to the left. For S_55, we show the image and SNR map panels alone since we do not model the lensing galaxy that is undetected in the *HST* snapshot.
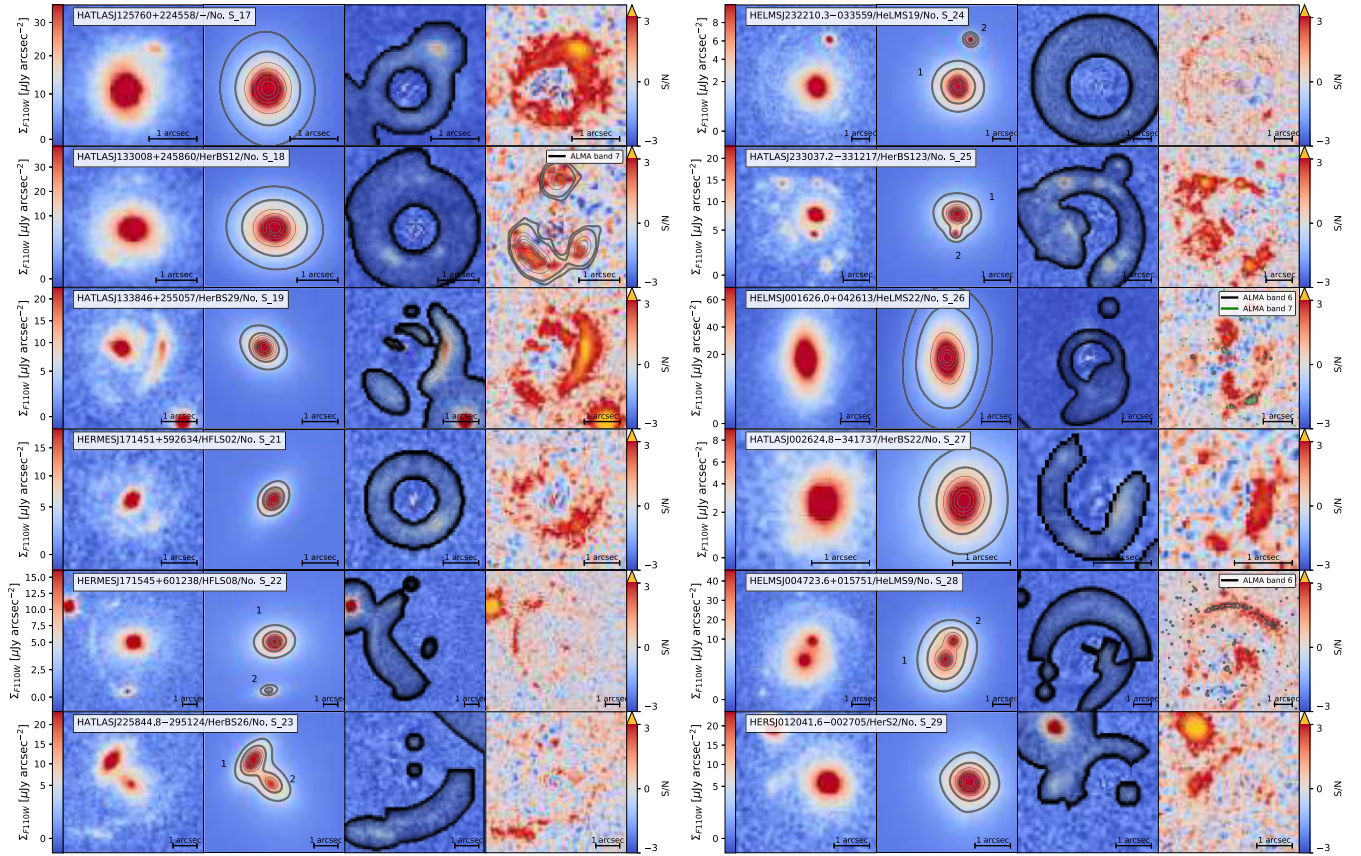
Figure A1. Continued.
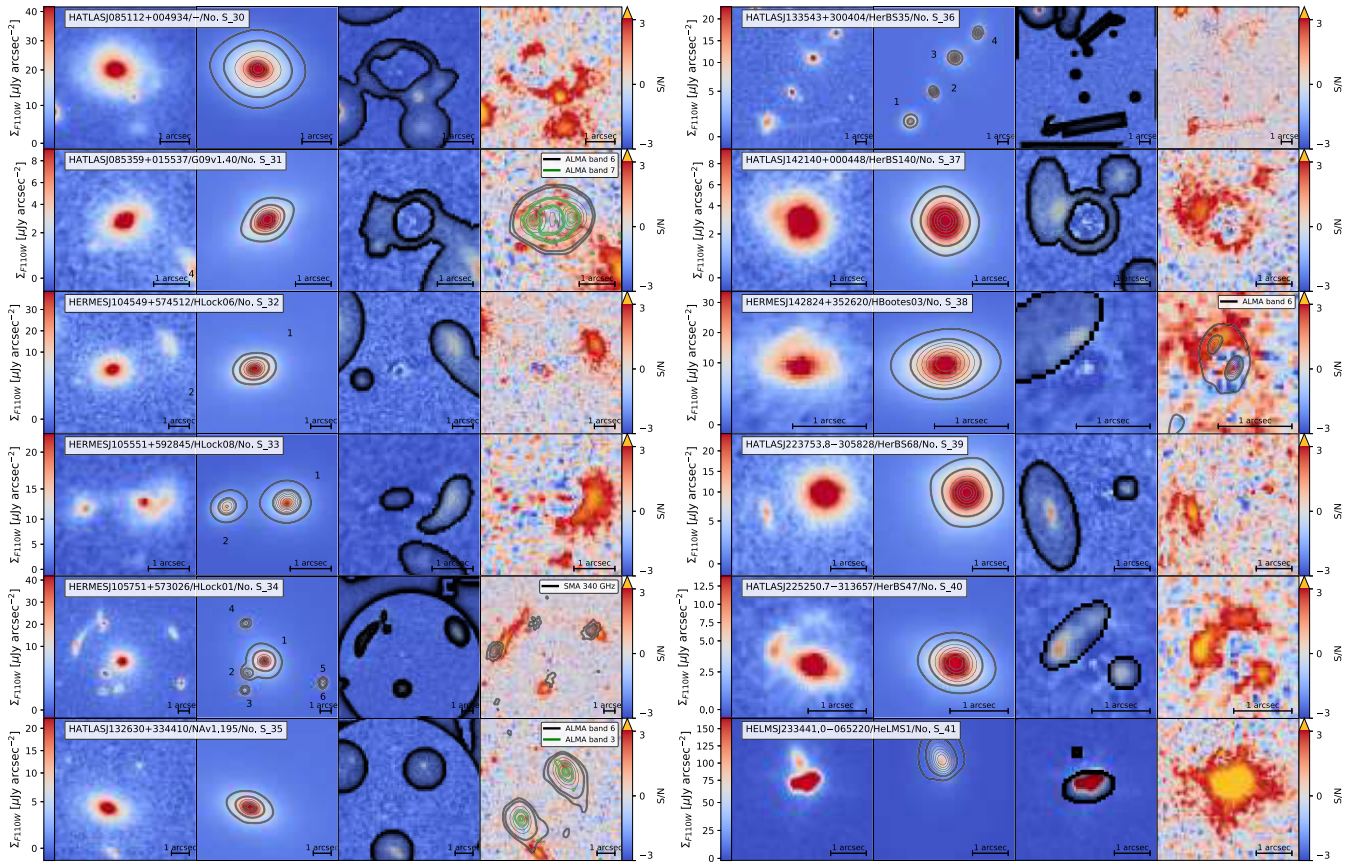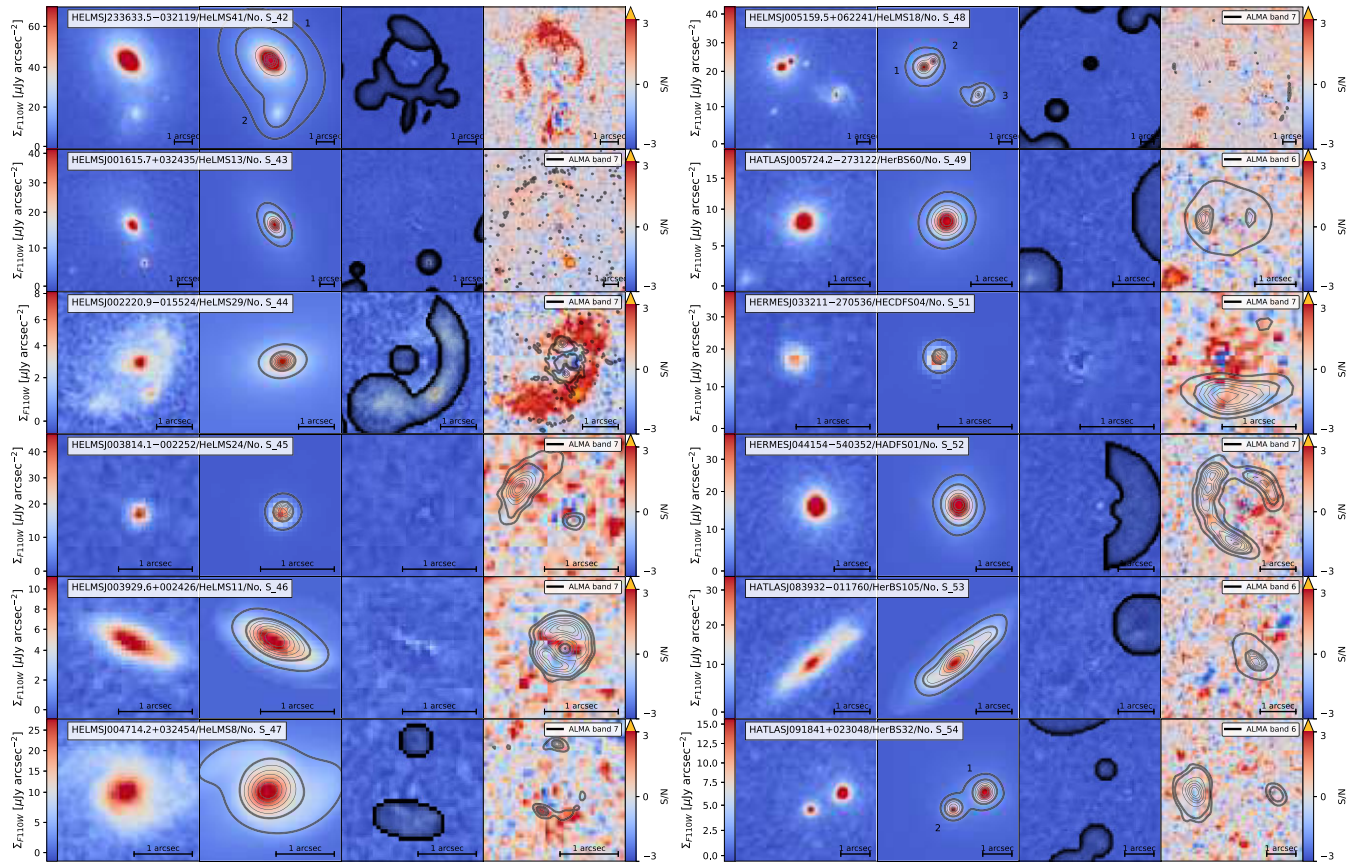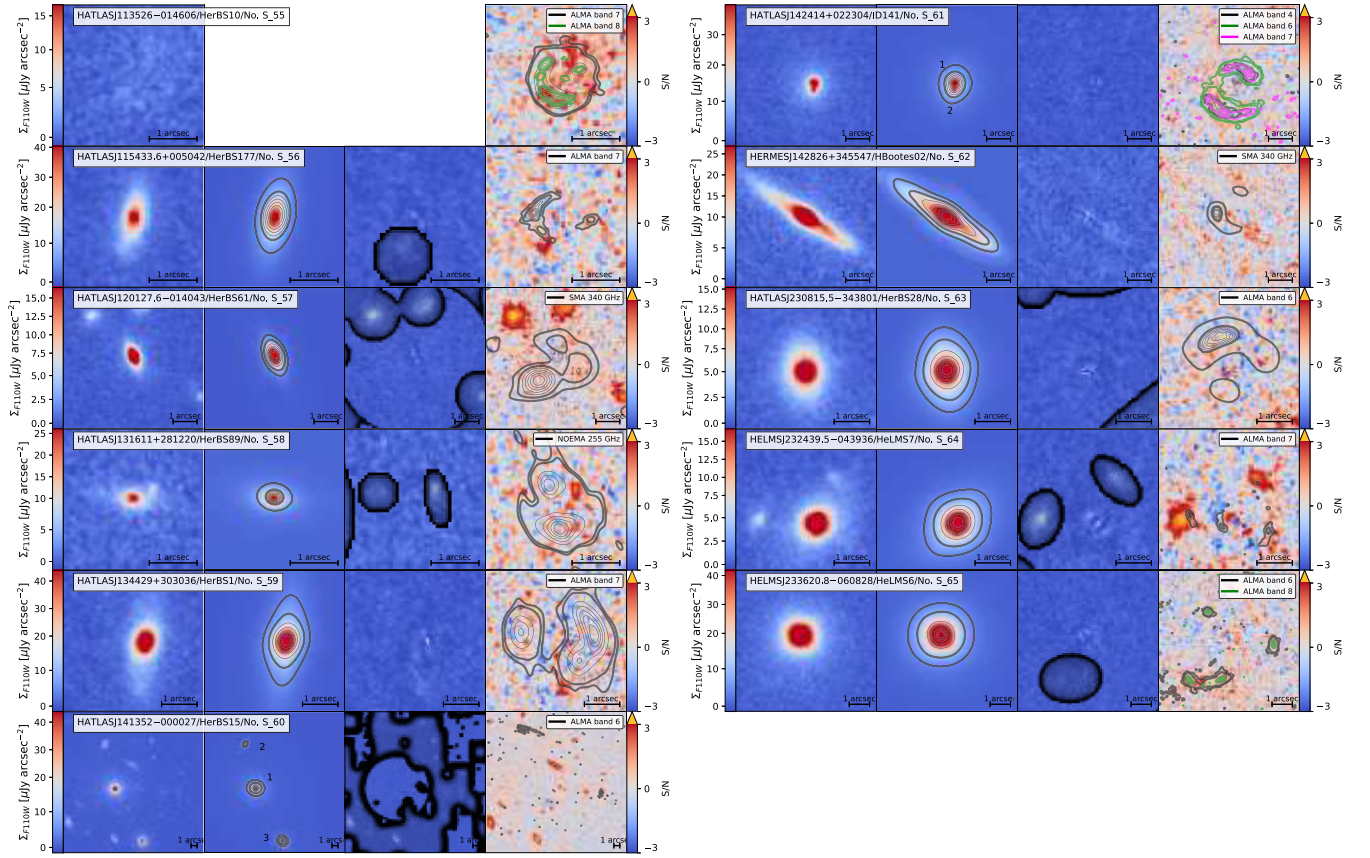
Figure A1. Continued.

Figure A1. Continued.

Figure A1. Continued.

Table A1. Structural parameters of the systems classified as A obtained from a parametric fit of their surface brightness distributions.

(1) No.	(2) IAU name	(3) Type	(4) Components	(5) μ_e [mag arcsec^{-2}]	(6) R_e [arcsec]	(7) n	(8) q	(9) PA [deg]	(10) m_{PSF} [mag]	(11) C/T	(12) χ^2	(13) N_{dof}
S.1	HATLASJ000330.6 − 321136	1	Sérsic	$20.69^{+0.12}_{-0.11}$	0.36 ± 0.02	$4.52^{+0.28}_{-0.27}$	0.803 ± 0.009	$73.05^{+0.96}_{-0.95}$	−	0.71 ± 0.05	1.03	35501
S.2	HATLASJ000912.7 − 300807	1	Sérsic	$23.39^{+0.15}_{-0.13}$	1.17 ± 0.06	0.57 ± 0.05	0.96 ± 0.02	$0.003^{+1.933}_{-1.884}$	−	0.29 ± 0.05	1.03	135697
			Sérsic	$21.63^{+0.23}_{-0.20}$	$1.16^{+0.17}_{-0.18}$	3.96 ± 0.27	0.929 ± 0.006	$34.92^{+1.39}_{-1.42}$	−	$0.42^{+0.09}_{-0.10}$		
S.3	HELMSJ001353.5 − 060200	1	Sérsic	$26.24^{+0.14}_{-0.12}$	$5.24^{+0.19}_{-0.18}$	0.80 ± 0.07	0.27 ± 0.03	$121.76^{+6.00}_{-6.17}$	−	$0.018^{+0.005}_{-0.004}$	1.03	61093
			Sérsic	$23.31^{+0.14}_{-0.12}$	3.93 ± 0.11	1.54 ± 0.13	0.78 ± 0.02	$139.43^{+3.96}_{-3.97}$	−	$0.56^{+0.10}_{-0.09}$		
			Sérsic	$21.21^{+0.28}_{-0.22}$	$0.26^{+0.04}_{-0.03}$	4.03 ± 0.60	0.90 ± 0.02	$20.44^{+3.85}_{-3.82}$	−	0.45 ± 0.11		
S.4	HELMSJ003619.8 + 002420	1	Exp. disc	$24.41^{+0.22}_{-0.18}$	2.02 ± 0.19	[1]	0.66 ± 0.05	$2.58^{+4.59}_{-4.42}$	−	0.55 ± 0.11	1.01	171928
			Sérsic	$20.59^{+0.23}_{-0.19}$	1.35 ± 0.17	1.26 ± 0.07	0.905 ± 0.005	$109.96^{+1.05}_{-1.06}$	−	$0.46^{+0.08}_{-0.09}$		
S.6	HERSJ011722.3 + 0056241	3	Sérsic	$17.78^{+0.16}_{-0.14}$	$0.177^{+0.006}_{-0.005}$	1.54 ± 0.15	0.90 ± 0.02	$159.86^{+2.55}_{-2.57}$	−	$0.11^{+0.03}_{-0.02}$	1.01	55924
			Sérsic	$23.65^{+0.14}_{-0.13}$	5.68 ± 0.17	$0.88^{+0.08}_{-0.07}$	0.92 ± 0.02	$128.85^{+4.37}_{-4.42}$	−	$0.42^{+0.08}_{-0.07}$		
			Sérsic	$21.64^{+0.29}_{-0.23}$	$0.60^{+0.08}_{-0.07}$	$5.19^{+0.42}_{-0.41}$	0.70 ± 0.02	$2.90^{+1.96}_{-1.91}$	−	$0.85^{+0.05}_{-0.07}$		
			Gauss	$24.97^{+0.21}_{-0.17}$	1.79 ± 0.16	[0.5]	$0.83^{+0.10}_{-0.11}$	$180.53^{+36.51}_{-36.53}$	−	$0.15^{+0.07}_{-0.05}$		
	HERSJ011722.3 + 0056242		Sérsic	$22.52^{+0.17}_{-0.15}$	0.25 ± 0.02	1.12 ± 0.15	0.93 ± 0.03	$-0.001^{+3.108}_{-3.000}$	−	[1]	1.01	56315
S.7	HERSJ012620.5 + 012950	1	Sérsic	$22.23^{+0.31}_{-0.24}$	0.89 ± 0.12	$5.86^{+0.48}_{-0.47}$	0.70 ± 0.02	$13.18^{+1.91}_{-1.92}$	−	$0.66^{+0.08}_{-0.11}$	1.04	66653
			Gauss	$21.72^{+0.09}_{-0.08}$	0.76 ± 0.05	[0.5]	0.88 ± 0.05	74.75 ± 3.74	−	$0.34^{+0.11}_{-0.08}$		
S.9	HERMESJ032637 − 270044	1	Sérsic	22.70 ± 0.05	$1.01^{+0.02}_{-0.03}$	5.73 ± 0.11	$0.997^{+0.002}_{-0.003}$	$46.45^{+0.69}_{-0.70}$	−	[1]	1.04	58583
S.10	HERMESJ033732 − 295353	1	Sérsic	$20.23^{+0.25}_{-0.21}$	0.50 ± 0.09	$4.51^{+0.37}_{-0.38}$	0.804 ± 0.009	$53.64^{+1.65}_{-1.68}$	−	$0.15^{+0.06}_{-0.05}$	1.05	177156
			Sérsic	$22.12^{+0.13}_{-0.11}$	$2.96^{+0.08}_{-0.07}$	$1.73^{+0.15}_{-0.14}$	0.96 ± 0.02	$149.69^{+1.32}_{-1.33}$	−	$0.71^{+0.05}_{-0.06}$		
			Sérsic	$20.61^{+0.14}_{-0.16}$	0.83 ± 0.03	0.69 ± 0.06	0.90 ± 0.02	$54.94^{+2.84}_{-2.94}$	−	$0.14^{+0.03}_{-0.02}$		
S.13	HERMESJ103827 + 581544	1	Sérsic	$20.25^{+0.10}_{-0.09}$	0.47 ± 0.03	1.56 ± 0.07	0.762 ± 0.008	6.07 ± 0.82	−	0.27 ± 0.03	1.02	107445
			Sérsic	$22.65^{+0.07}_{-0.06}$	$2.56^{+0.07}_{-0.08}$	1.07 ± 0.05	0.74 ± 0.01	$12.31^{+1.06}_{-1.07}$	−	0.73 ± 0.03		
S.14	HERMESJ110016 + 571736	1	Sérsic	21.76 ± 0.04	1.01 ± 0.02	2.68 ± 0.04	0.807 ± 0.004	$120.78^{+0.60}_{-0.59}$	−	[1]	1.06	46997
S.15	HATLASJ114638 − 0011321	2	Sérsic	$20.30^{+0.24}_{-0.20}$	0.19 ± 0.02	1.36 ± 0.17	0.53 ± 0.03	$50.27^{+1.72}_{-1.69}$	−	$0.58^{+0.08}_{-0.09}$	1.03	44201
			Sérsic	$24.52^{+0.16}_{-0.13}$	1.14 ± 0.07	$0.45^{+0.07}_{-0.08}$	$0.81^{+0.05}_{-0.04}$	$53.88^{+2.83}_{-2.87}$	−	$0.42^{+0.09}_{-0.08}$		
	HATLASJ114638 − 0011322		Sérsic	$21.17^{+0.25}_{-0.21}$	0.18 ± 0.02	3.26 ± 0.43	0.81 ± 0.03	$128.86^{+1.77}_{-1.75}$	−	$0.29^{+0.08}_{-0.07}$		
			Sérsic	$25.49^{+0.14}_{-0.12}$	2.29 ± 0.10	$1.73^{+0.15}_{-0.14}$	0.86 ± 0.03	$132.15^{+1.64}_{-1.66}$	−	$0.71^{+0.07}_{-0.08}$		
S.16	HATLASJ125126 + 254928	1	Sérsic	$23.11^{+0.08}_{-0.05}$	1.50 ± 0.04	7.96 ± 0.16	0.504 ± 0.005	135.36 ± 0.77	−	[1]	1.07	50036
S.17	HATLASJ125760 + 224558	1	Sérsic	22.33 ± 0.04	1.13 ± 0.02	4.63 ± 0.08	0.814 ± 0.004	$6.39^{+0.58}_{-0.61}$	−	[1]	1.07	50512
S.18	HATLASJ133008 + 245860	1	Sérsic	$21.81^{+0.30}_{-0.24}$	0.69 ± 0.09	$6.34^{+0.49}_{-0.50}$	0.80 ± 0.01	$81.56^{+1.97}_{-1.95}$	−	$0.83^{+0.05}_{-0.07}$	1.04	44862
			Gauss	$22.85^{+0.11}_{-0.10}$	0.83 ± 0.05	[0.5]	$0.91^{+0.05}_{-0.06}$	$96.76^{+10.85}_{-11.16}$	−	$0.17^{+0.05}_{-0.07}$		
S.19	HATLASJ133846 + 255057	1	Sérsic	$23.46^{+0.07}_{-0.06}$	1.11 ± 0.04	$5.25^{+0.15}_{-0.16}$	0.696 ± 0.007	$50.61^{+0.87}_{-0.90}$	−	[1]	1.04	57037
S.21	HERMESJ171451 + 592634	1	de Vauc.	$22.05^{+0.05}_{-0.04}$	0.45 ± 0.01	[4]	0.55 ± 0.01	$144.39^{+1.69}_{-1.64}$	−	[1]	1.10	31356

Table A1 – *continued*

No.	IAU name	Type	Components	μ_e [mag arcsec^{-2}]	R_e [arcsec]	n	q	PA [deg]	$m_{\rm PSF}$ [mag]	C/T	χ^2	$N_{\rm dof}$
(1)	(2)	(3)	(4)	(5)	(6)	(7)	(8)	(9)	(10)	(11)	(12)	(13)
S.22	HERMESJ171545 + 601238$_1$	3	Sérsic	$22.47^{+0.17}_{-0.15}$	0.56 ± 0.04	$4.43^{+0.33}_{-0.34}$	$0.992^{+0.006}_{-0.009}$	$180.00^{+1.08}_{-1.07}$	–	$0.17^{+0.04}_{-0.03}$	1.05	55119
			PSF	–					[24.97]	0.0023 ± 0.0002		
	HERMESJ171545 + 601238$_2$		Sérsic	24.43 ± 0.08	$4.10^{+0.14}_{-0.13}$	2.72 ± 0.16	0.69 ± 0.01	$96.24^{+1.29}_{-1.27}$	–	$0.83^{+0.03}_{-0.04}$	1.05	54970
S.23	HATLASJ225844.8 − 295124$_1$	2	Sérsic	$23.87^{+0.10}_{-0.09}$	1.23 ± 0.06	3.76 ± 0.20	0.39 ± 0.01	$99.53^{+1.02}_{-0.99}$	–	[1]	1.05	
	HATLASJ225844.8 − 295124$_2$		Sérsic	$20.69^{+0.07}_{-0.06}$	$0.44^{+0.01}_{-0.02}$	1.84 ± 0.06	0.448 ± 0.008	$145.47^{+0.87}_{-0.83}$	–	[1]	1.05	15053
S.24	HELMSJ232210.3 − 033559$_1$	3	Sérsic	$22.59^{+0.24}_{-0.20}$	0.61 ± 0.07	1.12 ± 0.15	0.39 ± 0.03	58.30 ± 1.77	–	0.10 ± 0.03	1.08	54469
			Sérsic	$24.93^{+0.09}_{-0.10}$	$3.29^{+0.15}_{-0.14}$	$2.83^{+0.27}_{-0.28}$	$0.69^{+0.03}_{-0.02}$	$26.28^{+3.28}_{-3.25}$	–	0.90 ± 0.03		
			Sérsic	$23.38^{+0.10}_{-0.09}$	1.42 ± 0.08	2.25 ± 0.14	$0.963^{+0.008}_{-0.009}$	$80.29^{+0.86}_{-0.89}$	–	0.81 ± 0.03		
	HELMSJ232210.3 − 033559$_2$		de Vauc.	$19.99^{+0.13}_{-0.12}$	0.214 ± 0.008	[4]	0.57 ± 0.03	$7.88^{+1.32}_{-1.33}$	–	0.19 ± 0.03	1.07	50334
			de Vauc.	21.44 ± 0.06	0.134 ± 0.006		0.74 ± 0.03	$64.64^{+4.21}_{-4.33}$	–	[1]		
S.25	HATLASJ233037.2 − 331217$_1$	3	Sérsic	$20.79^{+0.23}_{-0.19}$	0.25 ± 0.02	$7.05^{+0.58}_{-0.57}$	0.58 ± 0.02	$75.25^{+1.03}_{-1.05}$	–	$0.32^{+0.07}_{-0.06}$	1.05	47114
	HATLASJ233037.2 − 331217$_2$		Sérsic	$23.71^{+0.12}_{-0.10}$	1.66 ± 0.06	1.44 ± 0.14	0.89 ± 0.03	$139.93^{+3.41}_{-3.29}$	–	$0.68^{+0.06}_{-0.07}$		
			PSF	–					[23.14]	[1]		
Confirmed after the lens subtraction												
S.26	HELMSJ001626.0 + 042613	1	Sérsic	19.39 ± 0.05	0.52 ± 0.01	4.23 ± 0.09	0.467 ± 0.004	$7.10^{+0.26}_{-0.25}$	–	0.59 ± 0.03	1.05	55249
			Sérsic	$22.22^{+0.09}_{-0.08}$	1.83 ± 0.06	1.27 ± 0.08	0.63 ± 0.01	$162.98^{+1.24}_{-1.26}$	–	0.41 ± 0.03		
S.27	HATLASJ002624.8 − 341737	1	Sérsic	$21.92^{+0.25}_{-0.20}$	0.31 ± 0.03	$4.94^{+0.51}_{-0.52}$	0.63 ± 0.02	$172.06^{+1.73}_{-1.74}$	–	$0.54^{+0.08}_{-0.09}$	1.05	52636
			Sérsic	$24.33^{+0.13}_{-0.12}$	1.08 ± 0.04	$0.69^{+0.09}_{-0.08}$	$0.97^{+0.02}_{-0.03}$	180.01 ± 1.36	–	$0.46^{+0.09}_{-0.08}$		
S.28	HELMSJ004723.6 + 015751$_1$	2	de Vauc.	$18.60^{+0.30}_{-0.23}$	0.09 ± 0.01	[4]	$0.84^{+0.04}_{-0.03}$	$43.47^{+4.28}_{-4.38}$	–	$0.11^{+0.04}_{-0.03}$	1.03	58679
			Sérsic	21.92 ± 0.02	1.57 ± 0.02	$1.37^{+0.08}_{-0.07}$	0.851 ± 0.004	$165.60^{+1.09}_{-1.13}$	–	$0.89^{+0.03}_{-0.04}$		
	HELMSJ004723.6 + 015751$_2$		Sérsic	22.17 ± 0.06	0.80 ± 0.02	3.14 ± 0.07	$0.856^{+0.006}_{-0.007}$	$79.44^{+0.83}_{-0.82}$	–	[1]		
S.29	HERSJ012041.6 − 002705	1	Sérsic	$19.91^{+0.20}_{-0.17}$	0.19 ± 0.02	4.39 ± 0.34	0.71 ± 0.01	86.79 ± 1.04	–	0.44 ± 0.07	1.03	50744
S.30	HATLASJ085112 + 004934	1	Sérsic	$23.67^{+0.05}_{-0.06}$	$1.37^{+0.05}_{-0.06}$	1.98 ± 0.18	0.79 ± 0.02	$3.03^{+2.85}_{-2.88}$	–	0.56 ± 0.07	1.06	40914
			Sérsic	$20.24^{+0.41}_{-0.30}$	$0.27^{+0.07}_{-0.06}$	$4.45^{+0.72}_{-0.71}$	0.61 ± 0.02	$81.52^{+1.84}_{-1.83}$	–	$0.25^{+0.12}_{-0.10}$		
S.31	HATLASJ085359 + 015537	1	Sérsic	$21.51^{+0.17}_{-0.14}$	0.78 ± 0.02	0.44 ± 0.04	0.94 ± 0.03	$158.68^{+6.02}_{-6.11}$	–	0.37 ± 0.07	1.13	22254
			Sérsic	$22.35^{+0.14}_{-0.12}$	1.39 ± 0.04	0.72 ± 0.07	0.55 ± 0.02	$81.26^{+1.71}_{-1.71}$	–	0.38 ± 0.07		
			Sérsic	$22.69^{+0.26}_{-0.20}$	0.45 ± 0.05	6.78 ± 0.96	0.30 ± 0.03	$117.52^{+1.82}_{-1.81}$	–	$0.30^{+0.08}_{-0.07}$		
S.32	HERMESJ104549 + 574512	1	Sérsic	$26.34^{+0.14}_{-0.12}$	2.34 ± 0.09	5.14 ± 0.48	0.85 ± 0.03	$156.50^{+1.28}_{-1.29}$	–	$0.70^{+0.07}_{-0.08}$	1.04	60465
			Sérsic	$19.59^{+0.23}_{-0.19}$	0.16 ± 0.02	$3.86^{+0.40}_{-0.39}$	0.37 ± 0.02	$121.59^{+1.47}_{-1.38}$	–	$0.22^{+0.06}_{-0.05}$		
S.33	HERMESJ105551 + 592845$_1$	2	Sérsic	$21.54^{+0.12}_{-0.11}$	0.64 ± 0.03	1.74 ± 0.17	0.68 ± 0.03	$89.59^{+3.16}_{-3.13}$	–	$0.78^{+0.05}_{-0.06}$	1.15	6328
	HERMESJ105551 + 592845$_2$		Sérsic	22.62 ± 0.08	0.66 ± 0.03	1.82 ± 0.08	0.762 ± 0.009	92.59 ± 0.85	–	[1]		
S.34	HERMESJ105751 + 573026$_1$	2	Sérsic	$21.85^{+0.15}_{-0.13}$	0.28 ± 0.02	1.25 ± 0.12	0.79 ± 0.02	$123.08^{+1.84}_{-1.82}$	–	[1]	1.11	31547
			Sérsic	$20.36^{+0.49}_{-0.09}$	0.41 ± 0.02	3.90 ± 0.18	0.752 ± 0.008	$91.89^{+0.83}_{-0.84}$	–	0.27 ± 0.03		
			Sérsic	24.58 ± 0.07	5.16 ± 0.15	$2.63^{+0.13}_{-0.12}$	0.74 ± 0.01	$30.55^{+1.03}_{-1.05}$	–	0.73 ± 0.03		

Table A1 – *continued*

No. (1)	IAU name (2)	Type (3)	Components (4)	μ_e [mag arcsec^{-2}] (5)	R_e [arcsec] (6)	n (7)	q (8)	PA [deg] (9)	m_{PSF} [mag] (10)	C/T (11)	χ^2 (12)	N_{dof} (13)
	HERMESJ105751+573026$_2$		de Vauc.	$19.30^{+0.27}_{-0.22}$	0.10 ± 0.02	[4]	0.37 ± 0.04	$32.23^{+4.35}_{-4.53}$	–	$0.42^{+0.36}_{-0.24}$		
			Sérsic	$22.80^{+0.67}_{-0.42}$	$0.43^{+0.23}_{-0.21}$	$5.95^{+2.42}_{-2.72}$	$0.76^{+0.12}_{-0.13}$	$94.68^{+7.37}_{-7.46}$	–	$0.58^{+0.24}_{-0.36}$		
	HERMESJ105751+573026$_3$		Sérsic	$20.72^{+0.15}_{-0.13}$	0.137 ± 0.009	$3.63^{+0.31}_{-0.32}$	0.82 ± 0.02	74.54 ± 1.84	–	[1]		
	HERMESJ105751+573026$_4$		de Vauc.	21.16 ± 0.05	0.220 ± 0.007	[4]	0.61 ± 0.02	$100.13^{+2.05}_{-2.07}$	–	[1]		
	HERMESJ105751+573026$_5$		Sérsic	$20.30^{+0.13}_{-0.12}$	$0.131^{+0.008}_{-0.007}$	3.11 ± 0.23	0.89 ± 0.01	$175.89^{+1.42}_{-1.45}$	–	[1]		
	HERMESJ105751+573026$_6$		PSF	–	–	–	–	–	[23.60]	[1]		
S.35	HATLASJ132630+334410	1	Sérsic	23.80 ± 0.04	2.53 ± 0.05	5.73 ± 0.09	0.595 ± 0.004	$72.04^{+0.57}_{-0.59}$	–	[1]	1.05	39273
S.36	HATLASJ133543+300404$_1$	2	Sérsic	22.42 ± 0.08	0.65 ± 0.03	0.88 ± 0.04	0.902 ± 0.009	127.84 ± 0.89	–	0.954 ± 0.005	1.03	41523
			PSF	–	–	–	–	–	[24.11]	0.046 ± 0.005		
	HATLASJ133543+300404$_2$		Sérsic	$21.90^{+0.09}_{-0.08}$	0.41 ± 0.02	$4.97^{+0.23}_{-0.24}$	0.567 ± 0.010	$24.77^{+0.94}_{-0.95}$	–	[1]		
	HATLASJ133543+300404$_3$		Sérsic	23.50 ± 0.06	1.10 ± 0.03	5.58 ± 0.15	0.844 ± 0.007	$64.17^{+0.92}_{-0.92}$	–	[1]		
	HATLASJ133543+300404$_4$		Sérsic	$23.58^{+0.07}_{-0.06}$	1.02 ± 0.04	6.21 ± 0.21	0.609 ± 0.008	$165.10^{+0.80}_{-0.84}$	–	[1]		
S.37	HATLASJ142140+000448	1	Sérsic	$21.27^{+0.07}_{-0.06}$	0.38 ± 0.01	2.28 ± 0.05	0.925 ± 0.005	0.67 ± 0.77	–	[1]	1.11	44658
S.38	HERMESJ142824+352620		Sérsic	$21.47^{+0.08}_{-0.07}$	0.49 ± 0.02	$2.43^{+0.10}_{-0.09}$	0.487 ± 0.008	$92.76^{+0.89}_{-0.91}$	–	[1]	1.17	7204
S.39	HATLASJ223753.8−305828	1	Sérsic	21.81 ± 0.05	0.72 ± 0.02	$5.03^{+0.10}_{-0.09}$	0.940 ± 0.005	$87.28^{+0.70}_{-0.71}$	–	[1]	1.03	34943
S.40	HATLASJ225250.7−313657	1	Sérsic	$22.23^{+0.12}_{-0.10}$	0.40 ± 0.02	6.21 ± 0.40	0.53 ± 0.01	$75.70^{+1.21}_{-1.25}$	–	[1]	1.04	35357
S.41	HELMSJ233441.0−065220	1	Sérsic	$19.47^{+0.08}_{-0.17}$	0.28 ± 0.02	1.14 ± 0.09	0.38 ± 0.01	$22.16^{+1.00}_{-1.01}$	–	$0.49^{+0.07}_{-0.08}$	1.57	
S.42	HELMSJ233633.5−032119$_1$	2	Sérsic	$22.59^{+0.15}_{-0.13}$	1.00 ± 0.06	0.62 ± 0.06	0.68 ± 0.03	$167.72^{+2.29}_{-2.37}$	–	$0.51^{+0.08}_{-0.07}$	1.06	58206
			Sérsic	18.38 ± 0.05	0.332 ± 0.009	2.82 ± 0.06	$0.577^{+0.004}_{-0.003}$	$42.72^{+0.24}_{-0.25}$	–	0.34 ± 0.02		
	HELMSJ233633.5−032119$_2$		Sérsic	$21.94^{+0.06}_{-0.04}$	$2.55^{+0.03}_{-0.04}$	1.25 ± 0.04	0.738 ± 0.006	46.04 ± 0.84	–	0.66 ± 0.02		
			Sérsic	$23.16^{+0.06}_{-0.05}$	1.79 ± 0.04	2.21 ± 0.04	0.723 ± 0.005	$160.63^{+0.74}_{-0.75}$	–	[1]		

Confirmed through sub-mm/mm follow-up

No. (1)	IAU name (2)	Type (3)	Components (4)	μ_e [mag arcsec^{-2}] (5)	R_e [arcsec] (6)	n (7)	q (8)	PA [deg] (9)	m_{PSF} [mag] (10)	C/T (11)	χ^2 (12)	N_{dof} (13)
S.43	HELMSJ001615.7+032435	1	Sérsic	$24.18^{+0.31}_{-0.25}$	$3.46^{+0.45}_{-0.44}$	$7.32^{+0.38}_{-0.39}$	$0.579^{+0.007}_{-0.006}$	$31.91^{+0.67}_{-0.65}$	–	$0.86^{+0.04}_{-0.06}$	1.09	57290
S.44	HELMSJ002220.9−015524	1	Gauss	24.61 ± 0.09	3.25 ± 0.21	[0.5]	0.50 ± 0.07	$17.05^{+3.68}_{-3.72}$	–	$0.14^{+0.06}_{-0.04}$	1.13	37251
			Sérsic	$25.43^{+0.10}_{-0.09}$	2.09 ± 0.10	$3.77^{+0.19}_{-0.20}$	0.58 ± 0.01	98.62 ± 0.99	–	[1]		
S.45	HELMSJ003814.1−002252	1	PSF	–	–	–	–	–	[22.45]	[1]	1.04	18416
S.47	HELMSJ004714.2+032454	1	Sérsic	$20.79^{+0.18}_{-0.15}$	0.20 ± 0.02	0.60 ± 0.10	0.75 ± 0.03	$103.11^{+4.11}_{-4.17}$	–	$0.17^{+0.06}_{-0.05}$	1.01	26442
			Exp. disc	$23.42^{+0.19}_{-0.17}$	$1.47^{+0.14}_{-0.13}$	[1]	$0.60^{+0.04}_{-0.05}$	$111.21^{+4.52}_{-4.42}$	–	$0.83^{+0.05}_{-0.06}$		
S.48	HELMSJ005159.5+062241$_1$	2	Sérsic	$18.59^{+0.18}_{-0.17}$	$0.113^{+0.009}_{-0.010}$	2.28 ± 0.18	0.77 ± 0.01	119.44 ± 1.05	–	0.14 ± 0.03	1.03	48792
			de Vauc.	$23.10^{+0.08}_{-0.07}$	2.10 ± 0.06	[4]	0.96 ± 0.01	$9.11^{+1.24}_{-1.22}$	–	0.86 ± 0.03		
	HELMSJ005159.5+062241$_2$		Sérsic	20.48 ± 0.03	0.201 ± 0.004	$1.95^{+0.10}_{-0.09}$	0.76 ± 0.01	$173.86^{+1.76}_{-1.70}$	–	[1]		
	HELMSJ005159.5+062241$_3$		Sérsic	$24.00^{+0.07}_{-0.06}$	1.92 ± 0.06	1.33 ± 0.04	$0.703^{+0.007}_{-0.008}$	$37.42^{+0.90}_{-0.87}$	–	$0.899^{+0.008}_{-0.009}$		
			PSF	–	–	–	–	–	[22.52]	$0.101^{+0.009}_{-0.008}$		
S.49	HATLASJ005724.2−273122	1	Sérsic	$24.83^{+0.07}_{-0.06}$	1.46 ± 0.05	9.11 ± 0.30	0.858 ± 0.008	$126.93^{+0.84}_{-0.83}$	–	[1]	1.05	37643
S.51	HERMESJ033211−270536	1	PSF	–	–	–	–	–	[23.01]	[1]	1.07	9735

Table A1 – *continued*

No.	IAU name	Type	Components	μ_e [mag arcsec^{-2}]	R_e [arcsec]	n	q	PA [deg]	m_{PSF} [mag]	C/T	χ^2	N_{dof}
(1)	(2)	(3)	(4)	(5)	(6)	(7)	(8)	(9)	(10)	(11)	(12)	(13)
S.52	HERMESJ044154−540352	1	Sérsic	21.75 ± 0.06	0.54 ± 0.02	7.49 ± 0.17	0.783 ± 0.007	9.27 ± 0.86	–	[1]	1.03	44932
S.54	HATLASJ091841+023048$_1$	2	Sérsic	$20.11^{+0.34}_{-0.27}$	0.11 ± 0.02	$1.83^{+0.30}_{-0.31}$	0.69 ± 0.03	$152.52^{+1.94}_{-1.93}$	–	$0.19^{+0.07}_{-0.06}$	1.07	43760
			Sérsic	$25.92^{+0.14}_{-0.12}$	2.99 ± 0.14	2.44 ± 0.20	0.76 ± 0.02	$70.78^{+1.87}_{-1.88}$	–	$0.81^{+0.06}_{-0.07}$		
	HATLASJ091841+023048$_2$		de Vauc.	21.80 ± 0.06	0.155 ± 0.006	[4]	0.91 ± 0.03	$115.92^{+4.12}_{-4.11}$	–	[1]		
S.56	HATLASJ115433.6+005042	1	Sérsic	$21.10^{+0.08}_{-0.07}$	0.48 ± 0.02	1.83 ± 0.08	0.337 ± 0.009	$169.27^{+0.85}_{-0.87}$	–	[1]	1.01	34603
S.57	HATLASJ120127.6−014043	1	Sérsic	$25.61^{+0.35}_{-0.26}$	1.51 ± 0.23	1.00 ± 0.18	0.74 ± 0.03	$42.98^{+1.91}_{-1.83}$	–	$0.25^{+0.09}_{-0.08}$	1.06	28398
			Sérsic	$19.56^{+0.14}_{-0.12}$	0.225 ± 0.009	2.12 ± 0.20	0.27 ± 0.03	$20.79^{+1.31}_{-1.29}$	–	$0.75^{+0.08}_{-0.09}$		
S.58	HATLASJ131611+281220	1	Sérsic	$22.68^{+0.15}_{-0.13}$	0.45 ± 0.03	$5.08^{+0.44}_{-0.43}$	0.40 ± 0.02	$1.47^{+1.77}_{-1.73}$	–	[1]	1.02	28595
S.59	HATLASJ134429+303036	1	Sérsic	$19.44^{+0.37}_{-0.28}$	0.20 ± 0.03	2.50 ± 0.29	0.65 ± 0.01	$161.16^{+2.23}_{-2.21}$	–	$0.54^{+0.13}_{-0.14}$	1.04	48806
S.60	HATLASJ141352−000027$_1$	3	Exp. disc	$22.71^{+0.20}_{-0.16}$	1.64 ± 0.15	[1]	$0.26^{+0.04}_{-0.05}$	$173.10^{+4.55}_{-4.49}$	–	$0.46^{+0.14}_{-0.13}$	1.01	73852
			Sérsic	$20.47^{+0.18}_{-0.15}$	0.51 ± 0.05	$3.36^{+0.21}_{-0.22}$	0.825 ± 0.006	83.00 ± 1.08	–	$0.55^{+0.07}_{-0.08}$		
	HATLASJ141352−000027$_2$		Exp. disc	23.99 ± 0.11	2.87 ± 0.17	[1]	0.96 ± 0.03	$-0.01^{+4.33}_{-4.12}$	–	$0.45^{+0.07}_{-0.07}$	1.01	63073
	HATLASJ141352−000027$_3$		Sérsic	21.05 ± 0.08	0.31 ± 0.01	$3.64^{+0.17}_{-0.16}$	0.536 ± 0.010	$148.77^{+0.88}_{-0.89}$	–	[1]	1.01	64764
S.61	HATLASJ142414+022304$_1$	2	Sérsic	21.69 ± 0.05	0.68 ± 0.02	4.91 ± 0.10	0.866 ± 0.005	$41.57^{+0.79}_{-0.75}$	–	[1]	1.04	22914
			Sérsic	$24.20^{+0.07}_{-0.06}$	1.49 ± 0.05	3.76 ± 0.11	0.910 ± 0.007	$15.97^{+0.94}_{-0.89}$	–	$0.880^{+0.009}_{-0.010}$		
			PSF	–	–	–	–	–	[22.25]	$0.120^{+0.010}_{-0.009}$		
	HATLASJ142414+022304$_2$		Sérsic	$24.59^{+0.10}_{-0.08}$	1.13 ± 0.06	7.02 ± 0.36	0.68 ± 0.01	$149.22^{+1.02}_{-0.98}$	–	[1]		
S.62	HATLASJ230815.5−343801	1	Sérsic	$22.86^{+0.21}_{-0.17}$	0.56 ± 0.05	$8.73^{+0.65}_{-0.69}$	0.89 ± 0.01	157.26 ± 1.05	–	$0.76^{+0.05}_{-0.06}$	1.13	21244
			Sérsic	$22.89^{+0.14}_{-0.13}$	0.75 ± 0.03	0.52 ± 0.07	$0.56^{+0.03}_{-0.04}$	$7.75^{+1.49}_{-1.48}$	–	$0.24^{+0.06}_{-0.05}$		
S.63	HELMSJ232439.5−043936	1	Sérsic	$21.14^{+0.22}_{-0.18}$	$0.27^{+0.02}_{-0.03}$	3.26 ± 0.24	0.98 ± 0.01	$89.07^{+1.07}_{-1.03}$	–	$0.67^{+0.06}_{-0.08}$	1.06	53698
			Sérsic	$23.95^{+0.13}_{-0.12}$	1.10 ± 0.04	1.61 ± 0.18	0.52 ± 0.03	$129.07^{+1.13}_{-1.16}$	–	$0.33^{+0.08}_{-0.06}$		
S.64	HELMSJ233620.8−060828	1	Sérsic	20.53 ± 0.05	0.64 ± 0.02	$4.76^{+0.10}_{-0.09}$	0.878 ± 0.004	52.62 ± 0.24	–	0.85 ± 0.02	1.04	27656
			Sérsic	$22.22^{+0.12}_{-0.10}$	0.96 ± 0.04	0.87 ± 0.08	0.73 ± 0.03	$127.25^{+3.16}_{-3.17}$	–	0.15 ± 0.02		

Notes. Column (1): source reference number. Column (2): IAU name of the *Herschel* detection. Indices 1 and 2 refer to the two components of the lens candidate. Column (3): type of the system. Column (4): adopted model light for the lens components. Column (5): effective surface brightness, that is, the surface brightness at the effective radius. Column (6): effective radius, that is, the semimajor axis of the isophote containing half of the light of the component. Column (7): Sérsic index. Values fixed in the fit are bracketed. Column (8): axial ratio. Column (9): position angle. Column (10): magnitude of the unresolved component. Column (11): relative flux of the component C/T. Column (12): reduced χ^2 of the fit. Column (13): number of degrees of freedom of the fit.

Table A2. Derived properties of the lensing systems.

No.	IAU name	m_{F110W} [mag] M_{F110W} [mag]	μ_{50} [mag arcsec^{-2}] $\mu_{50,0}$ [mag kpc^{-2}]	R_{50} [arcsec] $R_{50,0}$ [kpc]	C_{31}	$\mu S_{1.1}$ [μJy]
(1)	(2)	(3)	(4)	(5)	(6)	(7)
S_1	HATLASJ000330.6 − 321136	19.30 ± 0.14	$21.49^{+0.21}_{-0.20}$	0.56 ± 0.05	$7.24^{+0.43}_{-0.40}$	1.81 ± 0.06
		$-17.78^{+0.73}_{-0.59}$	$20.10^{+0.37}_{-0.35}$	$2.99^{+0.52}_{-0.55}$		
S_2	HATLASJ000912.7 − 300807	17.09 ± 0.19	22.18 ± 0.26	$2.38^{+0.20}_{-0.17}$	$5.34^{+0.38}_{-0.40}$	45.35 ± 0.12
		$-19.26^{+0.83}_{-0.68}$	$21.10^{+0.38}_{-0.37}$	$10.49^{+2.19}_{-2.36}$		
S_3	HELMSJ001353.5 − 060200	19.99 ± 0.24	$23.16^{+0.41}_{-0.50}$	$0.90^{+0.25}_{-0.21}$	$7.26^{+1.15}_{-1.34}$	3.00 ± 0.10
		$-18.29^{+0.92}_{-0.72}$	$21.09^{+0.67}_{-0.64}$	$5.98^{+1.98}_{-1.57}$		
S_4	HELMSJ003619.8 + 002420	16.41 ± 0.18	$21.29^{+0.46}_{-0.36}$	$2.07^{+0.26}_{-0.20}$	$6.38^{+1.30}_{-0.97}$	13.58 ± 0.25
		$-19.72^{+0.18}_{-0.17}$	$20.29^{+0.46}_{-0.36}$	$8.55^{+1.06}_{-0.84}$		
S_6	HERSJ011722.3 + 005624$_1$	$19.45^{+0.34}_{-0.31}$	$22.10^{+0.47}_{-0.34}$	$0.67^{+0.08}_{-0.07}$	$8.68^{+0.74}_{-0.68}$	2.23 ± 0.10
		$-19.82^{+0.37}_{-0.36}$	$19.38^{+0.47}_{-0.37}$	$5.33^{+0.66}_{-0.55}$		
	HERSJ011722.3 + 005624$_2$	$22.87^{+0.23}_{-0.22}$	$22.52^{+0.17}_{-0.15}$	0.24 ± 0.02	2.95 ± 0.18	
		$-$	$-$	$-$		
S_7	HERSJ012620.5 + 012950	$18.86^{+0.29}_{-0.28}$	$21.22^{+0.13}_{-0.11}$	0.74 ± 0.05	$4.64^{+1.03}_{-0.76}$	5.72 ± 0.09
		$-18.55^{+0.42}_{-0.40}$	$19.67^{+0.20}_{-0.19}$	$4.27^{+0.43}_{-0.42}$		
S_9	HERMESJ032637 − 270044	19.10 ± 0.07	22.70 ± 0.05	$1.01^{+0.02}_{-0.03}$	10.12 ± 0.22	3.81 ± 0.13
		$-$	$-$	$-$		
S_10	HERMESJ033732 − 295353	$16.47^{+0.13}_{-0.12}$	$21.15^{+0.19}_{-0.20}$	1.91 ± 0.16	$5.36^{+0.33}_{-0.32}$	2.93 ± 0.07
		$-18.89^{+0.68}_{-0.55}$	$20.40^{+0.25}_{-0.27}$	6.15 ± 1.32		
S_13	HERMESJ103827 + 581544	$17.86^{+0.09}_{-0.08}$	$21.95^{+0.12}_{-0.13}$	1.53 ± 0.11	$4.75^{+0.19}_{-0.20}$	10.12 ± 0.23
		$-20.38^{+0.09}_{-0.08}$	$19.93^{+0.12}_{-0.13}$	$10.48^{+0.76}_{-0.72}$		
S_14	HERMESJ110016 + 571736	18.78 ± 0.06	21.76 ± 0.04	0.91 ± 0.02	4.99 ± 0.06	12.71 ± 0.19
		-20.19 ± 0.06	19.25 ± 0.04	6.97 ± 0.15		
S_15	HATLASJ114638 − 001132$_1$	$21.15^{+0.21}_{-0.20}$	$21.97^{+1.01}_{-0.70}$	$0.29^{+0.10}_{-0.05}$	$7.50^{+0.98}_{-1.17}$	6.33 ± 0.14
		$-19.03^{+0.21}_{-0.20}$	$18.50^{+1.01}_{-0.70}$	$2.51^{+0.86}_{-0.42}$		
	HATLASJ114638 − 001132$_2$	$20.52^{+0.16}_{-0.15}$	$24.52^{+0.29}_{-0.37}$	1.28 ± 0.24	$8.90^{+1.82}_{-1.84}$	
		$-19.66^{+0.16}_{-0.15}$	$21.05^{+0.29}_{-0.37}$	$10.90^{+2.06}_{-2.09}$		
S_16	HATLASJ125126 + 254928	19.21 ± 0.08	$23.11^{+0.06}_{-0.05}$	1.07 ± 0.03	$15.14^{+0.42}_{-0.41}$	4.18 ± 0.15
		$-19.16^{+0.46}_{-0.40}$	$21.02^{+0.27}_{-0.26}$	$7.46^{+0.52}_{-0.61}$		
S_17	HATLASJ125760 + 224558	18.83 ± 0.06	22.33 ± 0.04	1.02 ± 0.02	8.05 ± 0.13	10.13 ± 0.12
		-19.25 ± 0.06	20.42 ± 0.04	6.76 ± 0.15		
S_18	HATLASJ133008 + 245860	$19.05^{+0.35}_{-0.32}$	$21.55^{+0.23}_{-0.20}$	0.68 ± 0.05	$7.33^{+1.09}_{-1.03}$	3.54 ± 0.11
		$-18.36^{+0.35}_{-0.32}$	$20.01^{+0.23}_{-0.20}$	3.95 ± 0.31		
S_19	HATLASJ133846 + 255057	$20.09^{+0.10}_{-0.09}$	$23.46^{+0.07}_{-0.06}$	0.93 ± 0.03	9.19 ± 0.29	12.23 ± 0.12
		$-17.25^{+0.70}_{-0.55}$	$21.94^{+0.32}_{-0.30}$	$5.27^{+0.68}_{-0.84}$		
S_21	HERMESJ171451 + 592634	21.03 ± 0.08	$22.05^{+0.05}_{-0.04}$	$0.336^{+0.010}_{-0.009}$	$6.9887^{+0.0005}_{-0.0003}$	7.00 ± 0.13
		-19.17 ± 0.08	$18.56^{+0.05}_{-0.04}$	2.87 ± 0.08		
S_22	HERMESJ171545 + 601238$_1$	$18.38^{+0.11}_{-0.10}$	23.86 ± 0.12	2.68 ± 0.17	$6.51^{+0.37}_{-0.35}$	6.65 ± 0.14
		$-18.78^{+0.64}_{-0.53}$	$22.43^{+0.30}_{-0.29}$	$14.54^{+2.11}_{-2.40}$		
	HERMESJ171545 + 601238$_2$	$21.09^{+0.15}_{-0.14}$	$23.87^{+0.10}_{-0.09}$	0.77 ± 0.04	6.60 ± 0.32	
		$-$	$-$	$-$		
S_23	HATLASJ225844.8 − 295124$_1$	20.37 ± 0.10	$20.69^{+0.07}_{-0.06}$	0.29 ± 0.01	3.86 ± 0.08	1.41 ± 0.08
		$-18.28^{+0.93}_{-0.69}$	$18.41^{+0.57}_{-0.49}$	$2.13^{+0.22}_{-0.33}$		
	HATLASJ225844.8 − 295124$_2$	19.43 ± 0.14	$24.60^{+0.12}_{-0.14}$	$2.32^{+0.19}_{-0.20}$	$6.47^{+0.56}_{-0.53}$	
		$-19.18^{+0.92}_{-0.73}$	$22.33^{+0.56}_{-0.52}$	$16.60^{+2.34}_{-2.76}$		
S_24	HELMSJ232210.3 − 033559$_1$	$19.33^{+0.14}_{-0.13}$	$22.74^{+0.13}_{-0.14}$	$1.00^{+0.11}_{-0.12}$	$7.18^{+0.50}_{-0.53}$	3.47 ± 0.08

Table A2 – *continued*

No.	IAU name	m_{F110W} [mag] M_{F110W} [mag]	μ_{50} [mag arcsec^{-2}] $\mu_{50,0}$ [mag kpc^{-2}]	R_{50} [arcsec] $R_{50,0}$ [kpc]	C_{31}	$\mu S_{1.1}$ [μJy]
(1)	(2)	(3)	(4)	(5)	(6)	(7)
		$-15.46^{+1.76}_{-1.08}$	22.13 ± 0.33	$2.64^{+1.20}_{-1.30}$		
	HELMSJ232210.3 − 033559$_2$	22.74 ± 0.12	21.44 ± 0.06	$0.116^{+0.006}_{-0.005}$	$6.982^{+0.004}_{-0.001}$	
		−	−	−		
S_25	HATLASJ233037.2 − 331217$_1$	$19.45^{+0.14}_{-0.13}$	$22.91^{+0.19}_{-0.21}$	1.08 ± 0.12	$6.58^{+1.32}_{-1.03}$	19.93 ± 0.21
		$-19.07^{+0.82}_{-0.63}$	$20.71^{+0.52}_{-0.47}$	$7.66^{+1.16}_{-1.32}$		
	HATLASJ233037.2 − 331217$_2$	[23.14]	−	−	−	
		$-15.40^{+0.80}_{-0.60}$	−	−		
Confirmed after the lens subtraction						
S_26	HELMSJ001626.0 + 042613	17.63 ± 0.07	20.35 ± 0.11	0.73 ± 0.04	7.11 ± 0.17	1.46 ± 0.08
		-18.06 ± 0.07	19.50 ± 0.11	$2.63^{+0.16}_{-0.15}$		
S_27	HATLASJ002624.8 − 341737	$20.82^{+0.20}_{-0.19}$	$23.13^{+0.30}_{-0.31}$	$0.62^{+0.08}_{-0.07}$	$6.69^{+0.86}_{-0.94}$	0.90 ± 0.03
		$-18.61^{+1.20}_{-0.88}$	$20.28^{+0.88}_{-0.78}$	$4.88^{+0.81}_{-0.85}$		
S_28	HELMSJ004723.6 + 015751$_1$	18.14 ± 0.06	$21.67^{+0.09}_{-0.11}$	$1.27^{+0.06}_{-0.07}$	$4.10^{+0.49}_{-0.35}$	10.99 ± 0.18
		-18.86 ± 0.06	$20.32^{+0.09}_{-0.11}$	$6.65^{+0.33}_{-0.38}$		
	HELMSJ004723.6 + 015751$_2$	$19.58^{+0.09}_{-0.08}$	22.17 ± 0.06	0.74 ± 0.02	5.65 ± 0.10	
		−	−			
S_29	HERSJ012041.6 − 002705	19.59 ± 0.15	$21.97^{+0.34}_{-0.37}$	$0.58^{+0.10}_{-0.09}$	$9.37^{+0.72}_{-0.85}$	2.57 ± 0.10
		$-19.21^{+0.21}_{-0.20}$	$19.59^{+0.35}_{-0.38}$	$4.36^{+0.75}_{-0.66}$		
S_30	HATLASJ085112 + 004934	$18.68^{+0.17}_{-0.19}$	$20.81^{+0.18}_{-0.20}$	0.75 ± 0.06	$3.25^{+0.66}_{-0.47}$	9.37 ± 0.15
		$-19.86^{+1.58}_{-1.07}$	$18.60^{+0.88}_{-0.79}$	$5.27^{+0.91}_{-1.47}$		
S_31	HATLASJ085359 + 015537	$20.77^{+0.16}_{-0.15}$	$24.92^{+0.36}_{-0.38}$	$1.22^{+0.20}_{-0.18}$	$14.19^{+1.47}_{-1.44}$	0.87 ± 0.03
		$-19.26^{+0.58}_{-0.49}$	21.58 ± 0.57	$10.17^{+1.76}_{-1.54}$		
S_32	HERMESJ104549 + 574512	19.69 ± 0.14	$20.94^{+0.17}_{-0.18}$	0.41 ± 0.04	$5.16^{+0.46}_{-0.43}$	7.20 ± 0.10
		$-15.81^{+0.29}_{-0.28}$	$20.15^{+0.18}_{-0.19}$	$1.39^{+0.17}_{-0.16}$		
S_33	HERMESJ105551 + 592845$_1$	20.84 ± 0.12	22.62 ± 0.08	0.58 ± 0.02	3.83 ± 0.10	5.60 ± 0.08
		$-16.26^{+0.85}_{-0.66}$	$21.22^{+0.37}_{-0.33}$	$3.09^{+0.51}_{-0.63}$		
	HERMESJ105551 + 592845$_2$	$22.06^{+0.21}_{-0.20}$	$21.86^{+0.15}_{-0.13}$	0.25 ± 0.02	3.10 ± 0.14	
		−	−	−		
S_34	HERMESJ105751 + 573026$_1$	17.82 ± 0.08	$23.48^{+0.15}_{-0.17}$	2.64 ± 0.24	$9.89^{+0.72}_{-0.71}$	43.86 ± 0.21
		$-20.47^{+0.20}_{-0.19}$	$21.43^{+0.19}_{-0.20}$	$18.16^{+1.76}_{-1.72}$		
	HERMESJ105751 + 573026$_2$	$20.98^{+0.70}_{-0.81}$	$20.67^{+0.99}_{-1.12}$	$0.16^{+0.19}_{-0.08}$	$11.33^{+4.02}_{-2.77}$	
		−	−	−		
	HERMESJ105751 + 573026$_3$	$21.93^{+0.22}_{-0.20}$	$20.72^{+0.15}_{-0.13}$	0.124 ± 0.008	6.39 ± 0.49	
		−	−	−		
	HERMESJ105751 + 573026$_4$	$21.59^{+0.10}_{-0.09}$	21.16 ± 0.05	0.172 ± 0.006	$6.987^{+0.002}_{-0.001}$	
		−	−	−		
	HERMESJ105751 + 573026$_5$	$21.58^{+0.19}_{-0.18}$	$20.30^{+0.13}_{-0.12}$	0.124 ± 0.007	5.60 ± 0.34	
		−	−	−		
	HERMESJ105751 + 573026$_6$	[23.60]	−	−	−	
		−	−	−		
S_35	HATLASJ132630 + 334410	18.76 ± 0.06	23.80 ± 0.04	1.95 ± 0.04	$10.11^{+0.19}_{-0.18}$	1.34 ± 0.06
		-20.23 ± 0.06	21.28 ± 0.04	$15.00^{+0.32}_{-0.31}$		
S_36	HATLASJ133543 + 300404$_1$	$20.76^{+0.12}_{-0.11}$	$22.35^{+0.08}_{-0.07}$	0.60 ± 0.03	$2.88^{+0.06}_{-0.05}$	15.09 ± 0.23
		$-18.83^{+0.12}_{-0.11}$	$19.38^{+0.08}_{-0.07}$	4.90 ± 0.22		
	HATLASJ133543 + 300404$_2$	20.98 ± 0.13	$21.90^{+0.09}_{-0.08}$	0.31 ± 0.01	$8.66^{+0.43}_{-0.42}$	
		-18.62 ± 0.13	$18.92^{+0.09}_{-0.08}$	$2.50^{+0.12}_{-0.11}$		
	HATLASJ133543 + 300404$_3$	19.92 ± 0.09	23.50 ± 0.06	1.01 ± 0.03	9.81 ± 0.30	
		-19.67 ± 0.09	20.53 ± 0.06	$8.27^{+0.25}_{-0.26}$		
	HATLASJ133543 + 300404$_4$	$20.45^{+0.11}_{-0.10}$	$23.58^{+0.07}_{-0.06}$	0.80 ± 0.03	$11.10^{+0.45}_{-0.44}$	
		$-19.18^{+0.11}_{-0.10}$	$20.58^{+0.07}_{-0.06}$	6.56 ± 0.23		

Table A2 – *continued*

No.	IAU name	m_{F110W} [mag] M_{F110W} [mag]	μ_{50} [mag arcsec^{-2}] $\mu_{50,0}$ [mag kpc^{-2}]	R_{50} [arcsec] $R_{50,0}$ [kpc]	C_{31}	$\mu S_{1.1}$ [μJy]
(1)	(2)	(3)	(4)	(5)	(6)	(7)
S_37	HATLASJ142140 + 000448	20.34 ± 0.10	$21.27^{+0.07}_{-0.06}$	0.36 ± 0.01	4.44 ± 0.10	3.24 ± 0.05
		$-19.62^{+1.19}_{-0.80}$	$18.00^{+0.91}_{-0.73}$	$3.08^{+0.17}_{-0.34}$		
S_38	HERMESJ142824 + 352620	$20.69^{+0.12}_{-0.11}$	$21.47^{+0.08}_{-0.07}$	0.34 ± 0.01	4.64 ± 0.13	1.93 ± 0.05
		$-19.04^{+0.12}_{-0.11}$	$18.38^{+0.08}_{-0.07}$	2.81 ± 0.11		
S_39	HATLASJ223753.8 − 305828	$19.09^{+0.08}_{-0.07}$	21.81 ± 0.05	0.70 ± 0.02	$8.77^{+0.18}_{-0.17}$	3.56 ± 0.08
		$-18.92^{+0.79}_{-0.63}$	$19.93^{+0.43}_{-0.39}$	$4.55^{+0.53}_{-0.72}$		
S_40	HATLASJ225250.7 − 313657	$21.31^{+0.17}_{-0.16}$	$22.23^{+0.12}_{-0.10}$	0.29 ± 0.02	$11.10^{+0.86}_{-0.81}$	2.04 ± 0.03
		$-17.32^{+1.21}_{-0.86}$	$19.97^{+0.72}_{-0.63}$	$2.09^{+0.27}_{-0.43}$		
S_41	HELMSJ233441.0 − 065220	$19.79^{+0.17}_{-0.16}$	21.04 ± 0.51	$0.38^{+0.08}_{-0.05}$	$5.13^{+0.39}_{-0.40}$	172.09 ± 0.22
		$-18.09^{+0.17}_{-0.16}$	19.23 ± 0.51	$2.44^{+0.53}_{-0.35}$		
S_42	HELMSJ233633.5 − 032119$_1$	$16.99^{+0.05}_{-0.04}$	20.94 ± 0.08	1.29 ± 0.06	$7.24^{+0.28}_{-0.29}$	14.41 ± 0.21
		−	−	−		
	HELMSJ233633.5 − 032119$_2$	19.16 ± 0.08	$23.16^{+0.06}_{-0.05}$	1.53 ± 0.04	4.34 ± 0.06	
		−	−	−		
Confirmed through sub-mm/mm follow-up						
S_43	HELMSJ001615.7 + 032435	$18.24^{+0.36}_{-0.34}$	$23.64^{+0.18}_{-0.16}$	$2.54^{+0.24}_{-0.22}$	$9.16^{+1.47}_{-1.63}$	<0.04
		$-20.31^{+0.36}_{-0.34}$	$21.43^{+0.18}_{-0.16}$	$18.25^{+1.76}_{-1.62}$		
S_44	HELMSJ002220.9 − 015524	$21.07^{+0.15}_{-0.14}$	$25.43^{+0.10}_{-0.09}$	1.59 ± 0.08	6.62 ± 0.31	<0.04
		$-18.27^{+0.50}_{-0.44}$	$22.66^{+0.36}_{-0.34}$	$12.62^{+0.82}_{-0.90}$		
S_45	HELMSJ003814.1 − 002252	$[22.45]$	−	−	−	<0.04
		$-12.66^{+1.43}_{-0.95}$	−	−		
S_46	HELMSJ003929.6 + 002426	22.398 ± 0.003	$22.17^{+0.02}_{-0.01}$	0.256 ± 0.003	$2.38^{+0.08}_{-0.09}$	<0.04
		$-16.34^{+0.99}_{-0.73}$	$19.83^{+0.61}_{-0.53}$	$1.90^{+0.18}_{-0.31}$		
S_47	HELMSJ004714.2 + 032454	$20.25^{+0.24}_{-0.23}$	$23.07^{+0.17}_{-0.16}$	0.92 ± 0.14	$4.40^{+0.61}_{-0.60}$	<0.04
		$-17.43^{+0.54}_{-0.48}$	$21.38^{+0.31}_{-0.30}$	$5.57^{+1.05}_{-1.04}$		
S_48	HELMSJ005159.5 + 062241$_1$	18.36 ± 0.09	$22.71^{+0.10}_{-0.12}$	$1.67^{+0.11}_{-0.12}$	$5.95^{+0.91}_{-0.64}$	<0.04
		-19.94 ± 0.09	$20.66^{+0.10}_{-0.12}$	$11.54^{+0.74}_{-0.80}$		
	HELMSJ005159.5 + 062241$_2$	20.87 ± 0.06	20.48 ± 0.03	0.176 ± 0.004	$6.987^{+0.001}_{-0.002}$	
		−	−	−		
	HELMSJ005159.5 + 062241$_3$	20.03 ± 0.09	23.78 ± 0.05	1.42 ± 0.06	$4.08^{+0.13}_{-0.11}$	
		-18.24 ± 0.09	21.75 ± 0.05	$9.78^{+0.41}_{-0.42}$		
S_49	HATLASJ005724.2 − 273122	20.36 ± 0.10	$24.83^{+0.07}_{-0.06}$	1.35 ± 0.05	$18.23^{+0.86}_{-0.84}$	<0.05
		$-19.00^{+1.52}_{-0.99}$	$22.05^{+1.01}_{-0.83}$	$10.76^{+0.88}_{-2.22}$		
S_51	HERMESJ033211 − 270536	$[23.01]$	−	−	−	<0.03
		−	−	−		
S_52	HERMESJ044154 − 540352	$19.64^{+0.09}_{-0.08}$	21.75 ± 0.06	0.48 ± 0.01	$13.98^{+0.40}_{-0.41}$	<0.03
		−	−	−		
S_53	HATLASJ083932 − 011760	19.992 ± 0.002	21.16 ± 0.01	0.458 ± 0.005	2.18 ± 0.03	<0.03
		$-17.34^{+0.84}_{-0.65}$	$19.65^{+0.38}_{-0.35}$	$2.60^{+0.38}_{-0.50}$		
S_54	HATLASJ091841 + 023048$_1$	$20.48^{+0.17}_{-0.16}$	$25.27^{+0.24}_{-0.30}$	$1.85^{+0.30}_{-0.34}$	$9.93^{+5.55}_{-2.95}$	<0.04
		$-18.92^{+1.12}_{-0.80}$	$22.43^{+0.82}_{-0.71}$	$14.30^{+2.89}_{-3.32}$		
	HATLASJ091841 + 023048$_2$	22.56 ± 0.11	21.80 ± 0.06	0.148 ± 0.006	$6.9849^{+0.0029}_{-0.0010}$	
		$-16.84^{+1.12}_{-0.80}$	$18.97^{+0.78}_{-0.67}$	$1.18^{+0.09}_{-0.17}$		
S_56	HATLASJ115433.6 + 005042	20.89 ± 0.13	$21.10^{+0.08}_{-0.07}$	0.28 ± 0.01	$3.83^{+0.10}_{-0.11}$	<0.03
		$-17.03^{+0.62}_{-0.51}$	$19.28^{+0.33}_{-0.31}$	$1.79^{+0.19}_{-0.23}$		
S_57	HATLASJ120127.6 − 014043	20.85 ± 0.19	$20.44^{+0.60}_{-0.42}$	$0.18^{+0.04}_{-0.03}$	$8.27^{+3.41}_{-1.67}$	<0.04
		$-18.43^{+1.34}_{-0.91}$	$17.81^{+1.06}_{-0.91}$	$1.37^{+0.36}_{-0.29}$		
S_58	HATLASJ131611 + 281220	$21.87^{+0.22}_{-0.20}$	$22.68^{+0.15}_{-0.13}$	0.29 ± 0.02	$8.86^{+0.84}_{-0.78}$	<0.03
		$-17.48^{+0.46}_{-0.42}$	$19.91^{+0.34}_{-0.33}$	$2.31^{+0.18}_{-0.19}$		

Table A2 – *continued*

No.	IAU name	m_{F110W} [mag] M_{F110W} [mag]	μ_{50} [mag arcsec^{-2}] $\mu_{50,0}$ [mag kpc^{-2}]	R_{50} [arcsec] $R_{50,0}$ [kpc]	C_{31}	$\mu S_{1.1}$ [μJy]
(1)	(2)	(3)	(4)	(5)	(6)	(7)
S_59	HATLASJ134429 + 303036	$19.57^{+0.32}_{-0.30}$	$20.85^{+0.73}_{-0.69}$	$0.38^{+0.14}_{-0.08}$	$6.09^{+0.69}_{-0.68}$	<0.04
		$-19.01^{+0.32}_{-0.30}$	$18.61^{+0.73}_{-0.69}$	$2.74^{+1.00}_{-0.58}$		
S_60	HATLASJ141352 − 000027$_1$	$18.19^{+0.18}_{-0.17}$	$22.11^{+0.43}_{-0.42}$	$1.22^{+0.23}_{-0.18}$	7.67 ± 0.48	<0.04
		$-19.85^{+0.18}_{-0.17}$	$20.21^{+0.43}_{-0.42}$	$8.01^{+1.52}_{-1.17}$		
	HATLASJ141352-000027$_2$	$20.91^{+0.13}_{-0.12}$	21.05 ± 0.08	0.229 ± 0.010	$6.40^{+0.27}_{-0.26}$	
		−	−	−		
	HATLASJ141352 − 000027$_3$	19.18 ± 0.08	21.69 ± 0.05	0.64 ± 0.02	8.56 ± 0.18	
		-18.87 ± 0.08	19.79 ± 0.05	$4.20^{+0.10}_{-0.11}$		
S_61	HATLASJ142414 + 022304$_1$	$19.95^{+0.09}_{-0.08}$	23.04 ± 0.09	1.11 ± 0.06	$10.30^{+0.64}_{-0.53}$	<0.03
		-18.31 ± 0.09	21.68 ± 0.05	$7.65^{+0.39}_{-0.40}$		
	HATLASJ142414 + 022304$_2$	$21.05^{+0.15}_{-0.14}$	$24.59^{+0.10}_{-0.09}$	0.93 ± 0.05	$12.87^{+0.84}_{-0.80}$	
		$-17.21^{+0.15}_{-0.14}$	$22.56^{+0.10}_{-0.09}$	$6.41^{+0.31}_{-0.30}$		
S_62	HERMESJ142826 + 345547	19.254 ± 0.001	20.801 ± 0.007	0.542 ± 0.003	2.56 ± 0.03	<0.03
			19.297 ± 0.007	3.07 ± 0.02		
		-18.065 ± 0.001				
S_63	HATLASJ230815.5 − 343801	$20.18^{+0.21}_{-0.20}$	$22.15^{+0.13}_{-0.11}$	$0.55^{+0.02}_{-0.03}$	$7.71^{+1.59}_{-1.35}$	<0.04
		$-18.58^{+0.93}_{-0.72}$	$19.80^{+0.59}_{-0.52}$	$4.05^{+0.42}_{-0.60}$		
S_64	HELMSJ232439.5 − 043936	$20.34^{+0.21}_{-0.20}$	$21.64^{+0.31}_{-0.26}$	0.40 ± 0.03	$5.96^{+0.32}_{-0.29}$	<0.04
		$-18.21^{+1.27}_{-0.89}$	$19.44^{+0.77}_{-0.67}$	$2.86^{+0.43}_{-0.65}$		
S_65	HELMSJ233620.8 − 060828	17.97 ± 0.07	20.39 ± 0.05	0.66 ± 0.02	$6.58^{+0.20}_{-0.19}$	<0.04
		-19.24 ± 0.07	18.94 ± 0.05	3.62 ± 0.09		

Notes. Column (1): source reference number. Column (2): IAU name of the *Herschel* detection. Indices 1 and 2 refer to the two components of the lens candidate. Column (3): apparent magnitude of the model (first row), absolute magnitude of the model (second row). Column (4): total effective radius in arcsec (first row) and in kpc (second row). Column (5): total effective surface brightness before (first row) and after correcting for cosmological dimming (second row). Column (6): C_{31} of the model. Column (7): flux density of the background source uncorrected for the magnification.

APPENDIX B: FULL CANDIDATES TABLE

Below, we present the figures and tables that did not enter the full body of the paper for the sake of readability.

In Table B1, we summarize the properties for all the systems classified as B, C, and D after the inclusion of the multiwavelength follow-ups and the lens subtraction. Fig. B2 shows the candidates classified as C or D.
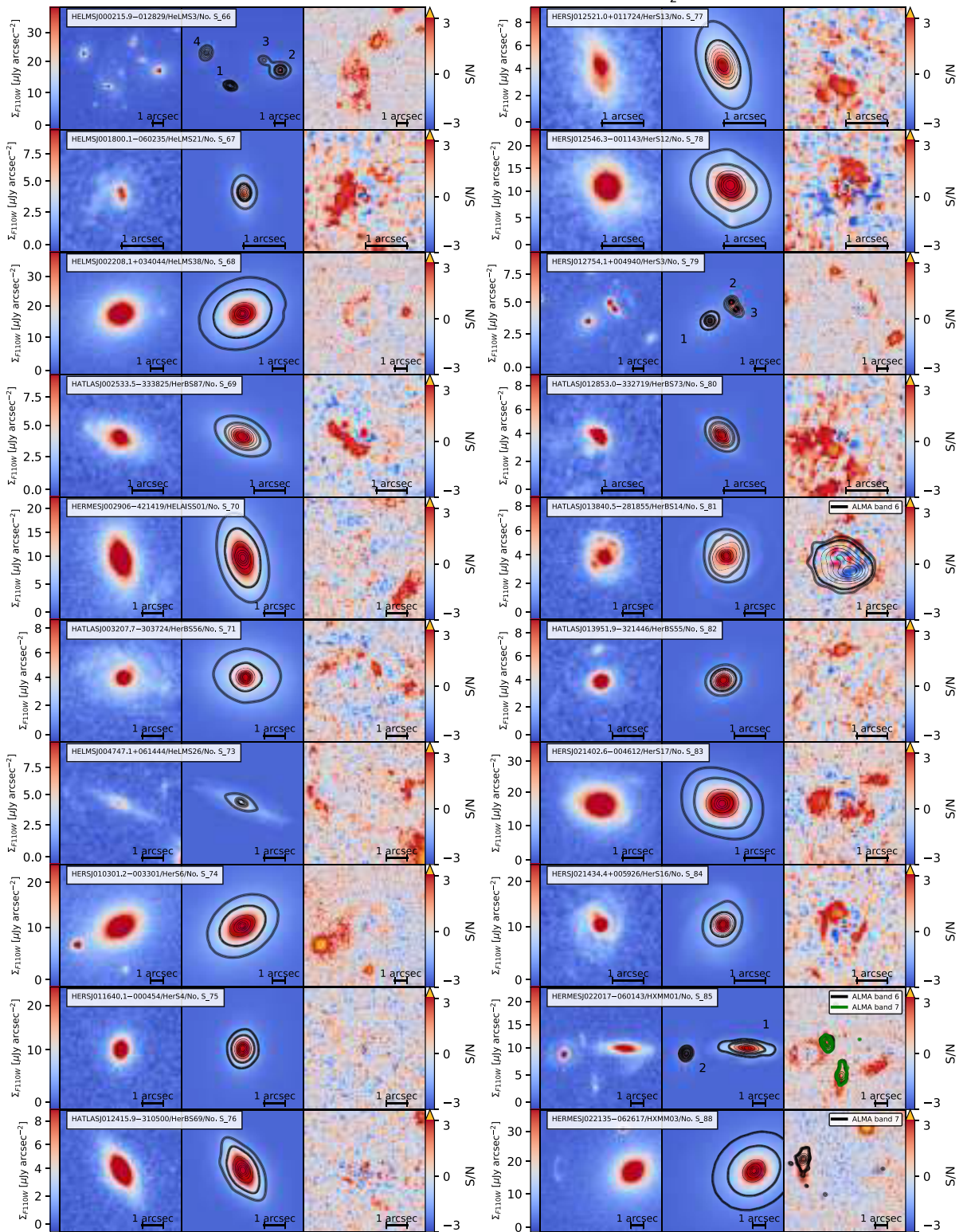
Figure B1. From left to right panels: observed *HST F110W* image, best-fitting surface brightness model of the lens and SNR map of the residuals for the B class candidates. The contours in the model images are taken at two levels corresponding to SNR = 5 and 10 (thick curves), and five uniformly spaced levels between the SNR = 10 and the maximum SNR in the model image (thin curves). The residual maps show the contours of available high-resolution multiwavelength data taken at two levels corresponding to SNR = 5 and 10 (thick curves), and five uniformly spaced levels between the SNR = 10 and the maximum SNR in the multiwavelength image (thin black curves). The images are oriented such that N is up and E is to the left.
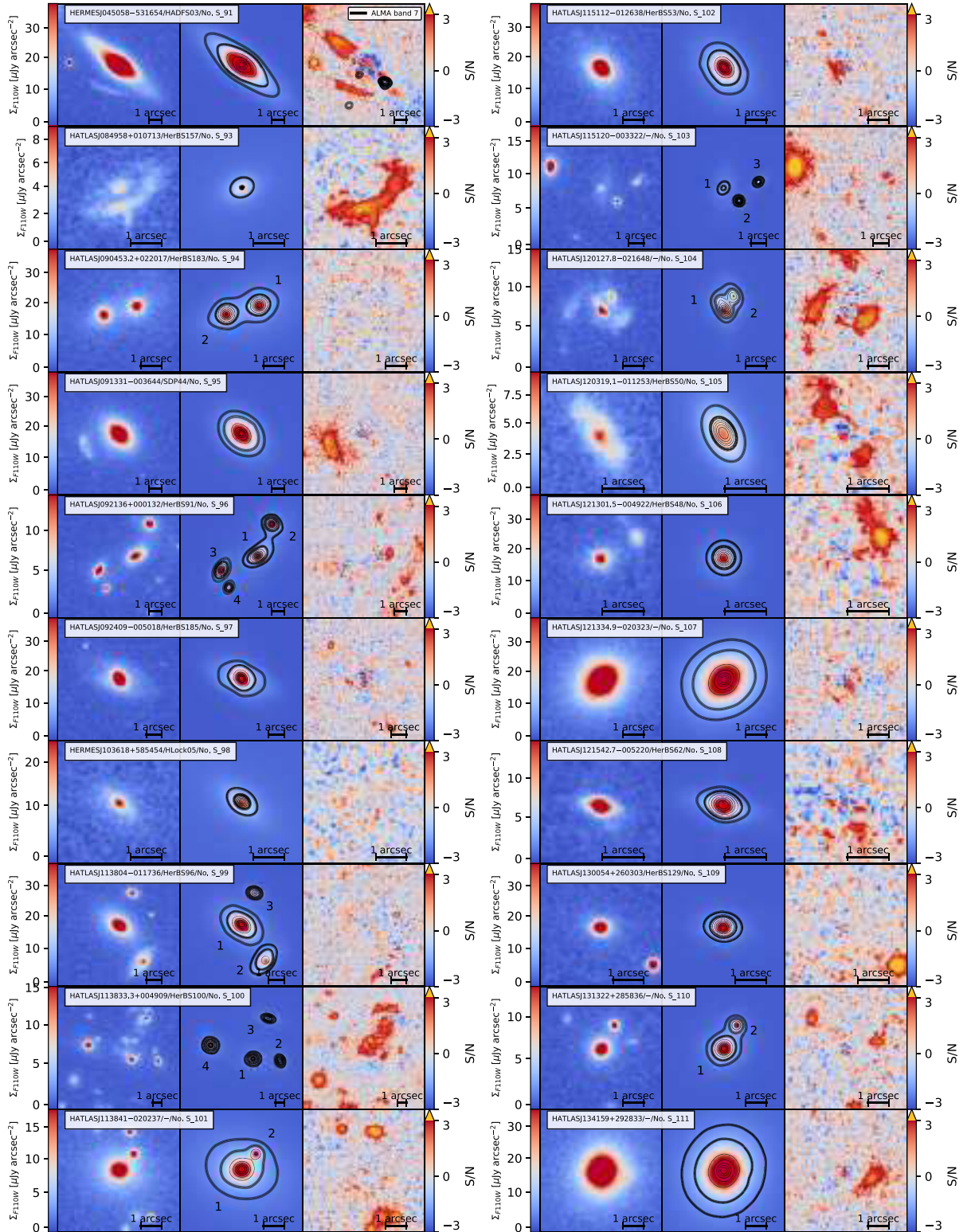
Figure B1. Continued.
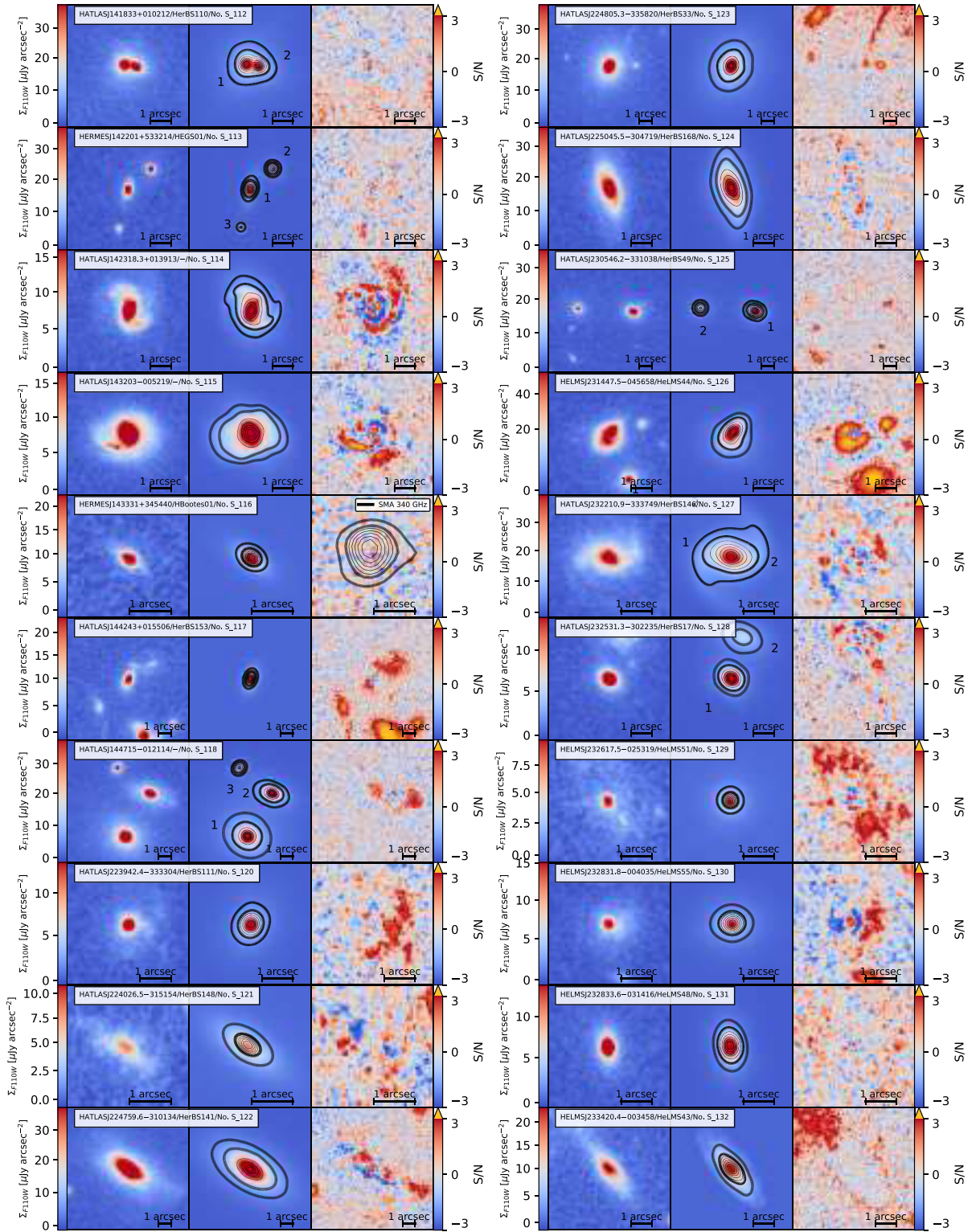
Figure B1. Continued.
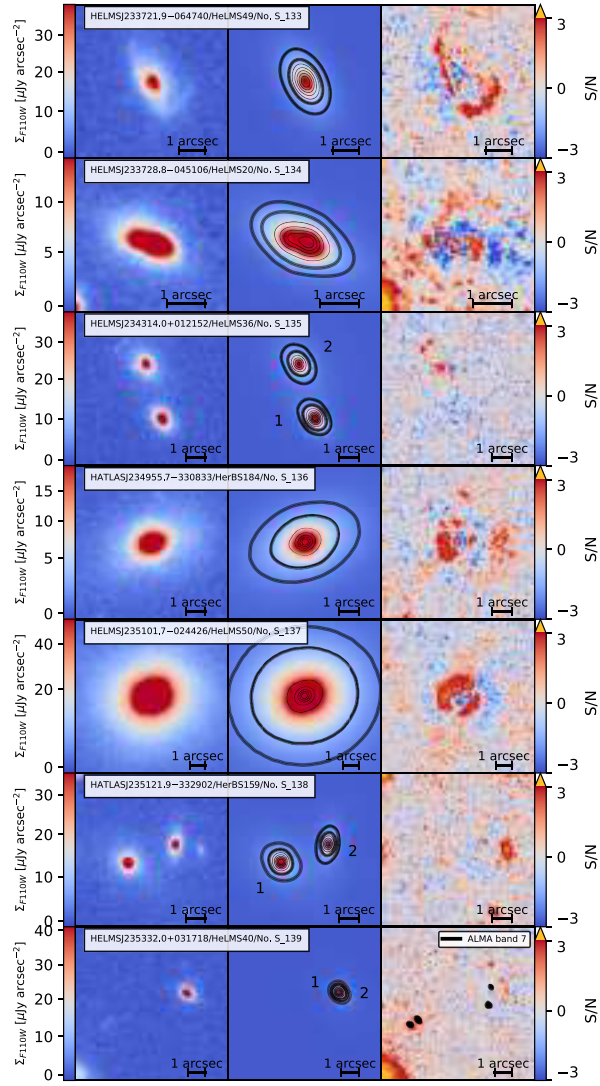
Figure B1. Continued.
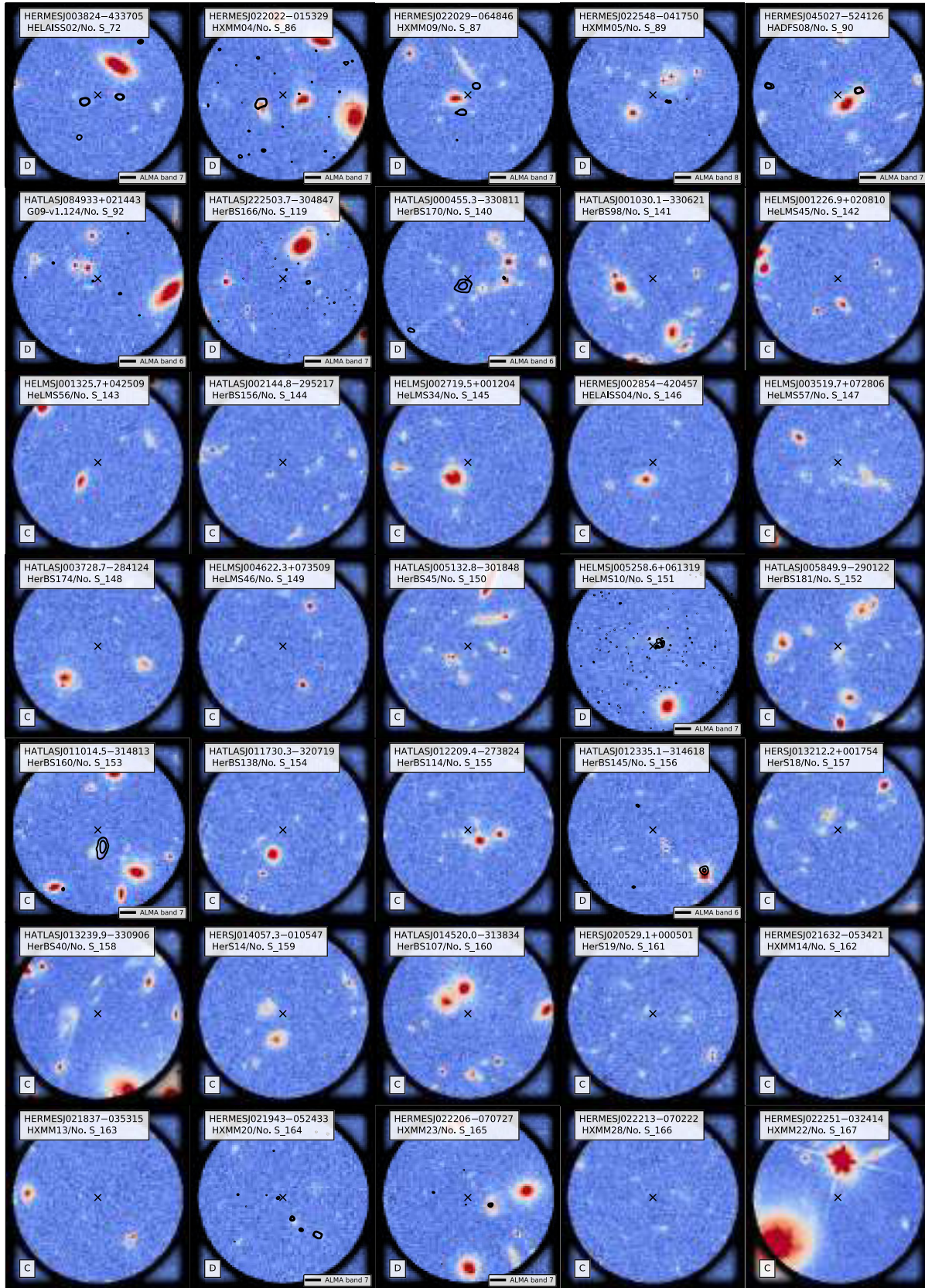
Figure B2. Systems classified as C or D. Each panel show a ∼ 20 arcsec × 20 arcsec cutout of the *HST* image, the black-shaded regions mark the *Herschel*/SPIRE beam at 250 μm. Lastly, we show the contours of available high-resolution multiwavelength data taken at two levels corresponding to SNR = 5 and 10.

Figure B2. Continued.

Figure B2. Continued.

Figure B2. Continued.

Figure B2. Continued.

Table B1. Properties of the 217 systems classified as B, C, and D by visual inspection.

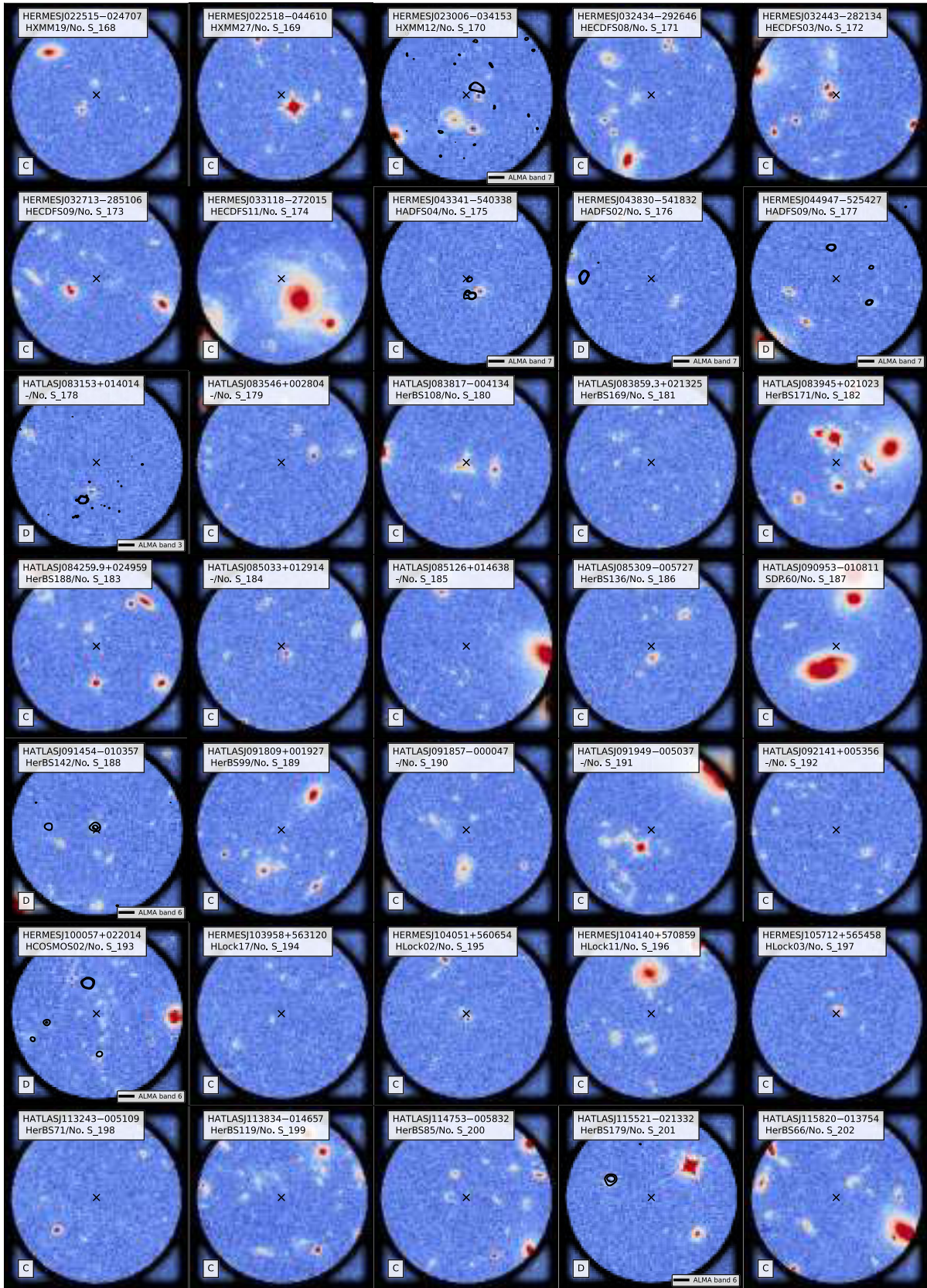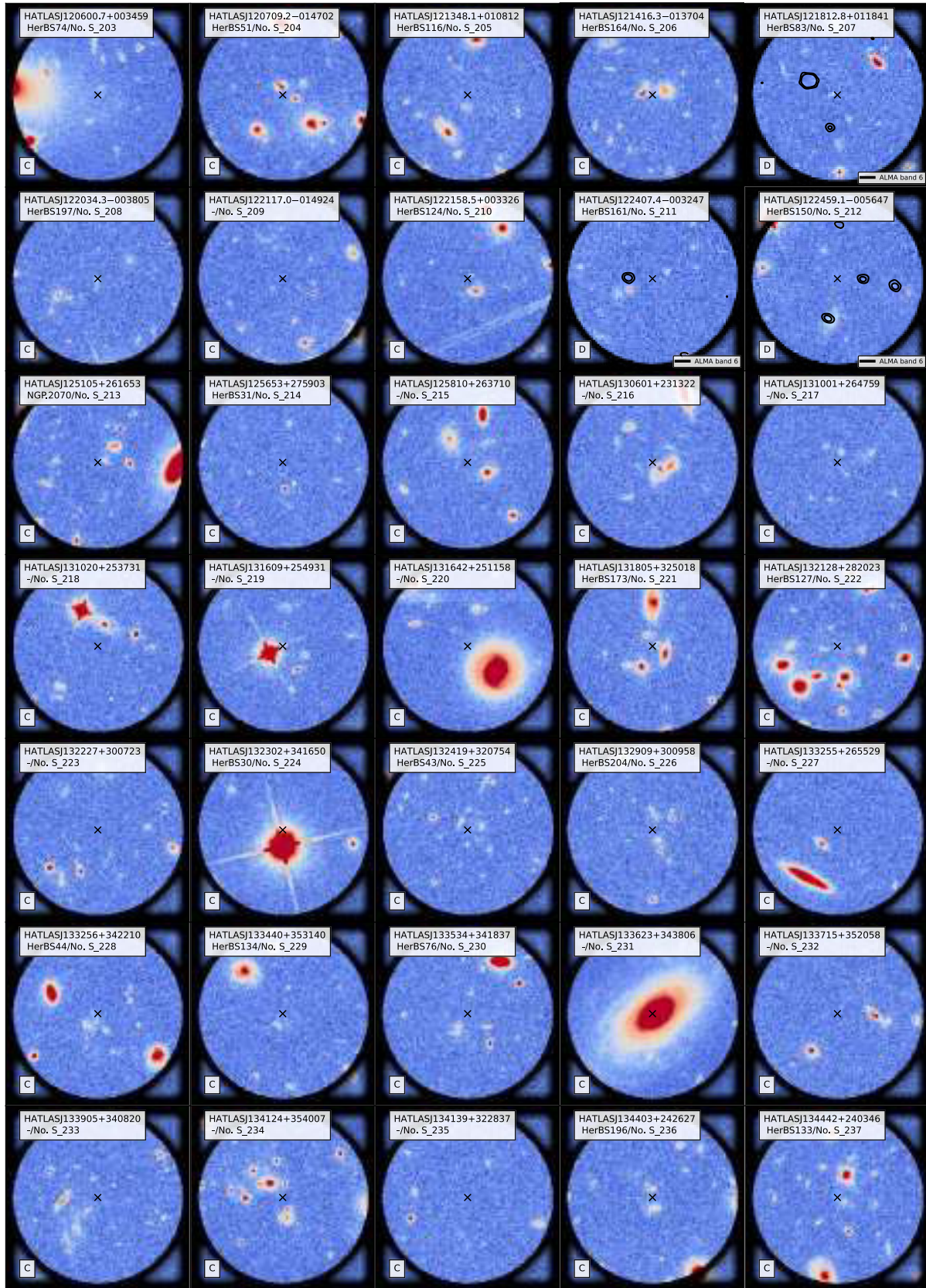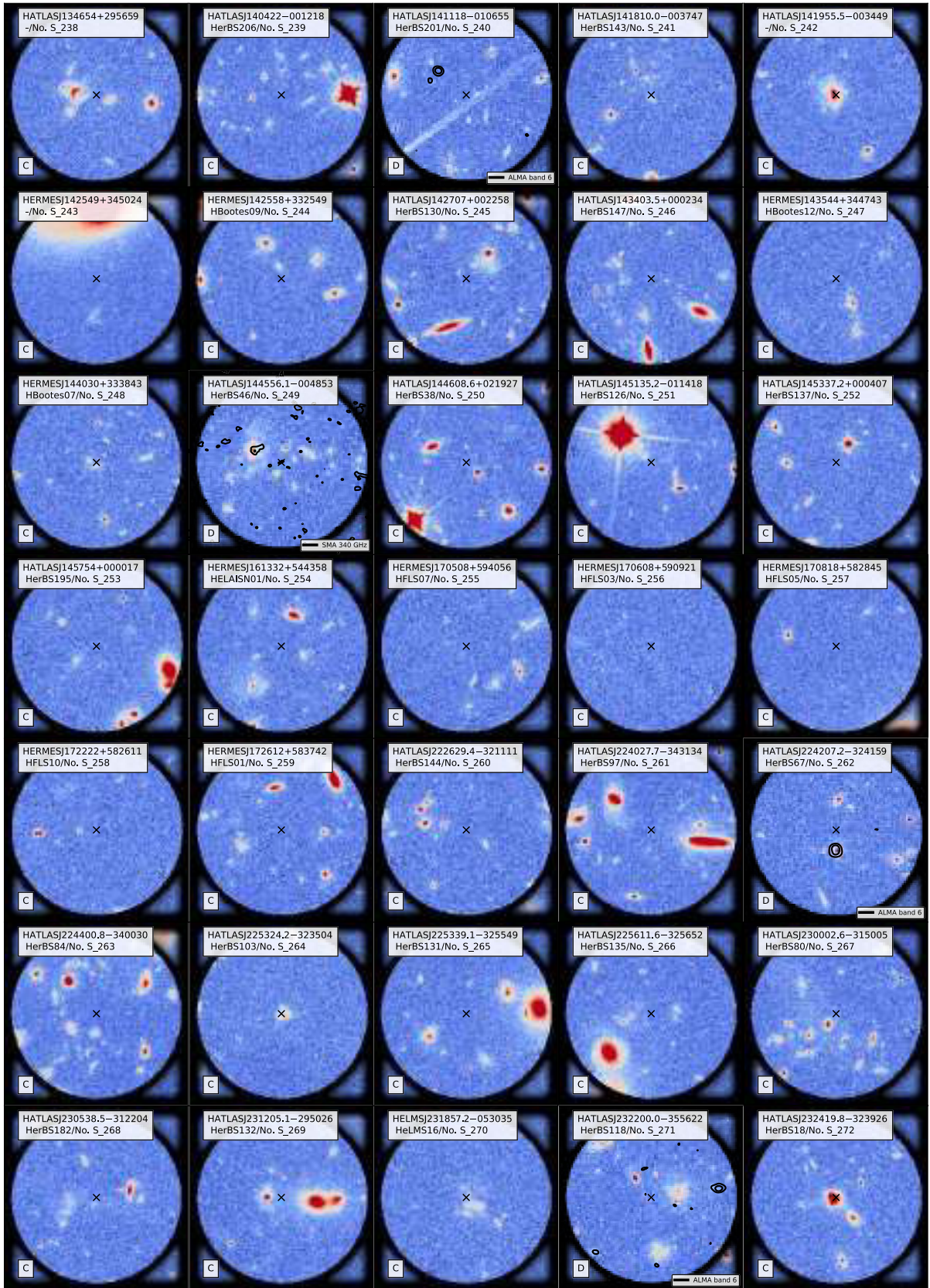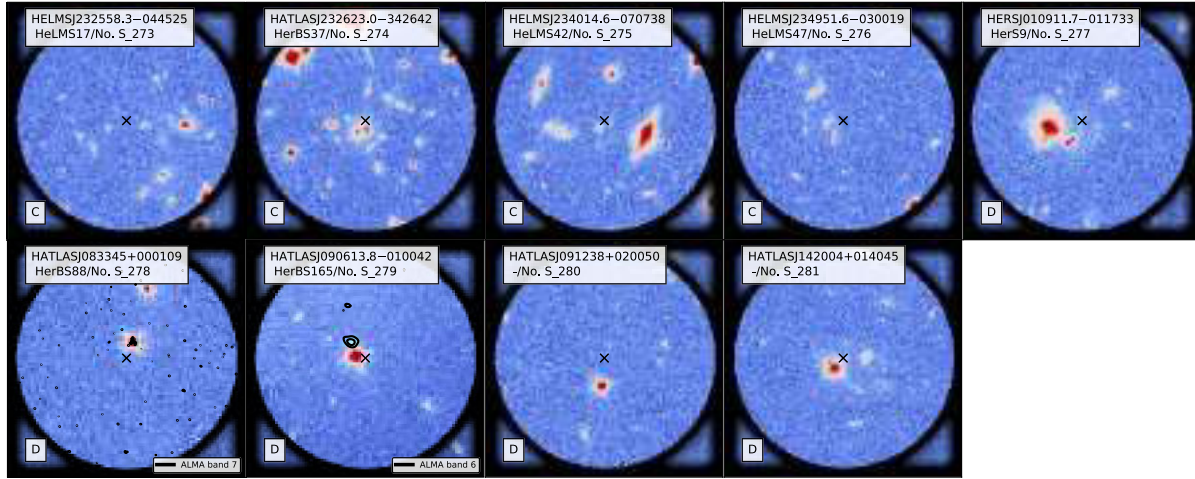| No.	IAU name	Alt. name	Ref.	RA [h m s]	Dec. [d m s]	Vis. class.	Multiw. class.	S_{250} [mJy]	S_{350} [mJy]	S_{500} [mJy]	Ref.
(1)	(2)	(3)	(4)	(5)	(6)	(7)	(8)	(9)	(10)	(11)	(12)
S_66	HELMSJ000215.9 − 012829	HELMS3	Na16	00:02:16	−01:28:29.00	B	–	643.0 ± 7.0	510.0 ± 6.0	258.0 ± 7.0	Na16
S_67	HELMSJ001800.1 − 060235	HELMS21	Na16	00:18:00	−06:02:35.00	B	–	206.0 ± 6.0	186.0 ± 7.0	130.0 ± 7.0	Na16
S_68	HELMSJ002208.1 + 034044	HELMS38	Na16	00:22:08	+03:40:44.00	B	–	190.0 ± 6.0	157.0 ± 6.0	113.0 ± 7.0	Na16
S_69	HATLASJ002533.5 − 333825	HerBS87	Ba18	00:25:34	−33:38:26.00	B	–	114.7 ± 5.2	127.8 ± 6.1	96.0 ± 7.3	Ba18
S_70	HERMESJ002906 − 421419	HELAISS01	Wa13	00:29:06	−42:14:19.00	B	–	129.0	116.0	81.0	Ca14
S_71	HATLASJ003207.7 − 303724	HerBS56	Ba18	00:32:08	−30:37:24.00	B	–	80.3 ± 5.0	106.2 ± 5.2	105.8 ± 6.3	Ne17
S_72	HERMESJ003824 − 433705	HELAISS02	Ca14	00:38:24	−43:37:05.00	B	D	115.0 ± 6.0	124.0 ± 6.0	108.0 ± 6.0	Bu15
S_73	HELMSJ004747.1 + 061444	HELMS26	Na16	00:47:47	+06:14:44.00	B	–	85.0 ± 7.0	119.0 ± 6.0	125.0 ± 8.0	Na16
S_74	HERSJ010301.2 − 003300	HERS6	Na16	01:03:01	−00:33:01.00	B	–	121.0 ± 7.0	147.0 ± 6.0	130.0 ± 8.0	Na16
S_75	HERSJ011640.1 − 000454	HERS4	Na16	01:16:40	−00:04:54.00	B	–	137.5 ± 6.75	196.11 ± 6.56	189.91 ± 7.81	Su17
S_76	HATLASJ012415.9 − 310500	HerBS69	Ba18	01:24:16	−31:05:00.00	B	–	140.4 ± 5.4	154.5 ± 5.7	100.3 ± 7.0	Ne17
S_77	HERSJ012521.0 + 011724	HERS13	Na16	01:25:21	+01:17:24.00	B	–	165.0 ± 8.0	153.0 ± 7.0	114.0 ± 10.0	Na16
S_78	HERSJ012546.3 − 001143	HERS12	Na16	01:25:46	−00:11:43.00	B	–	152.0 ± 8.0	135.0 ± 7.0	114.0 ± 9.0	Na16
S_79	HERSJ012754.1 + 004940	HERS3	Na16	01:27:54	+00:49:40.00	B	–	253.0 ± 6.0	250.0 ± 6.0	191.0 ± 7.0	Na16
S_80	HATLASJ012853.0 − 332719	HerBS73	Ba18	01:28:53	−33:27:19.00	B	–	117.1 ± 6.0	129.0 ± 6.2	99.6 ± 7.4	Ba18
S_81	HATLASJ013840.5 − 281855	HerBS14	Ba18	01:38:41	−28:18:56.00	B	Unc.	116.3 ± 5.7	177.0 ± 6.0	179.4 ± 7.1	Ne17
S_82	HATLASJ013951.9 − 321446	HerBS55	Ba18	01:39:52	−32:14:46.00	B	–	109.0 ± 4.9	116.5 ± 5.3	107.1 ± 6.2	Ne17
S_83	HERSJ021402.6 − 004612	HERS17	Na16	02:14:03	−00:46:12.00	B	–	110.0 ± 8.0	130.0 ± 8.0	105.0 ± 9.0	Na16
S_84	HERSJ021434.4 + 005926	HERS16	Na16	02:14:34	+00:59:26.00	B	–	110.0 ± 9.0	134.0 ± 8.0	109.0 ± 10.0	Na16
S_85	HERMESJ022017 − 060143	HXMM01	Wa13	02:20:17	−06:01:44.00	B	Unc.	179.0 ± 7.0	188.0 ± 8.0	134.0 ± 7.0	Bu15
S_86	HERMESJ022022 − 015329	HXMM04	Wa13	02:20:22	−01:53:29.00	B	D	162.0 ± 7.0	157.0 ± 8.0	125.0 ± 11.0	Bu15
S_87	HERMESJ022029 − 064846	HXMM09	Wa13	02:20:29	−06:48:46.00	B	D	129.0 ± 7.0	118.0 ± 8.0	85.0 ± 7.0	Bu15
S_88	HERMESJ022135 − 062617	HXMM03	Wa13	02:21:35	−06:26:17.00	B	Unc.	114.0 ± 7.0	134.0 ± 8.0	116.0 ± 7.0	Bu15
S_89	HERMESJ022548 − 041750	HXMM05	Wa13	02:25:48	−04:17:50.00	B	D	103.0 ± 7.0	118.0 ± 8.0	97.0 ± 7.0	Bu15
S_90	HERMESJ045027 − 524126	HADFS08	Ca14	04:50:27	−52:41:26.00	B	D	142.0 ± 6.0	133.0 ± 6.0	90.0 ± 6.0	Bu15
S_91	HERMESJ045058 − 531654	HADFS03	Ca14	04:50:58	−53:16:54.00	B	Unc.	119.0 ± 6.0	102.0 ± 6.0	63.0 ± 6.0	Bu15
S_92	HATLASJ084933 + 021443	G09-v1.124 HerBS8	Ba18	08:49:33	+02:14:43.14	B	D	216.7 ± 7.5	248.5 ± 8.2	208.6 ± 8.6	Ne17
S_93	HATLASJ084958 + 010713	G09v1.1259 HerBS157	Ba18	08:49:58	+01:07:12.73	B	–	81.2 ± 7.3	98.9 ± 8.2	85.2 ± 8.7	Ba18
S_94	HATLASJ090453.2 + 022017	HerBS183 SDP.392	Ba18	09:04:53	+02:20:17.87	B	–	87.0 ± 7.2	98.2 ± 8.0	82.3 ± 8.8	Ba18
S_95	HATLASJ091331 − 003644	SDP.44		09:13:31	−00:36:44.00	B	–	175.5 ± 6.5	142.2 ± 7.4	85.8 ± 7.8	Va16
S_96	HATLASJ092136 + 000132	HerBS91	Ba18	09:21:36	+00:01:31.92	B	–	139.2 ± 7.3	128.8 ± 8.1	95.1 ± 8.6	Ba18
S_97	HATLASJ092409 − 005018	HerBS185		09:24:09	−00:50:18.00	B	–	71.8 ± 7.4	87.7 ± 8.2	82.2 ± 8.5	Ba18
S_98	HERMESJ103618 + 585454	HLock05	Wa13	10:36:18	+58:54:54.36	B	–	71.0	102.0	98.0	Ca14
S_99	HATLASJ113804 − 011736	HerBS96	Ba18	11:38:04	−01:17:36.00	B	–	85.1 ± 7.3	98.4 ± 8.2	94.8 ± 8.8	Ba18
S_100	HATLASJ113833.3 + 004909	HerBS100	Ba18	11:38:33	+00:49:09.68	B	–	96.8 ± 7.3	106.4 ± 8.1	93.4 ± 8.7	Ba18
S_101	HATLASJ113841 − 020237	–	–	11:38:41	−02:02:37.00	B	–	45.2 ± 7.0	72.7 ± 7.7	71.7 ± 8.1	Ma18
S_102	HATLASJ115112 − 012638	HerBS53	Ba18	11:51:12	−01:26:38.00	B	–	141.2 ± 7.4	137.7 ± 8.2	108.4 ± 8.8	Ne17

Table B1 *– continued*

No.	IAU name	Alt. name	Ref.	RA [h m s]	Dec. [d m s]	Vis. class.	Multiw. class.	S_{250} [mJy]	S_{350} [mJy]	S_{500} [mJy]	Ref.
(1)	(2)	(3)	(4)	(5)	(6)	(7)	(8)	(9)	(10)	(11)	(12)
S_103	HATLASJ115120 − 003322	–	–	11:51:20	−00:33:22.00	B	–	146.9 ± 7.8	150.3 ± 8.5	88.0 ± 8.8	Ma18
S_104	HATLASJ120127.8 − 021648	–	–	12:01:28	−02:16:48.00	B	–	207.9 ± 7.3	160.9 ± 8.2	103.6 ± 8.7	Ne17
S_105	HATLASJ120319.1 − 011253	HerBS50	Ba18	12:03:19	−01:12:54.00	B	–	114.3 ± 7.4	142.8 ± 8.2	110.2 ± 8.6	Ne17
S_106	HATLASJ121301.5 − 004922	HerBS48	Ba18	12:13:02	−00:49:23.00	B	–	136.6 ± 6.6	142.6 ± 7.4	110.9 ± 7.7	Ne17
S_107	HATLASJ121334.9 − 020323	–	–	12:13:35	−02:03:23.00	B	–	211.0	197.9	129.9	Ne17
S_108	HATLASJ121542.7 − 005220	HerBS62	Ba18	12:15:43	−00:52:20.00	B	–	119.7 ± 7.4	135.5 ± 8.2	103.4 ± 8.6	Ne17
S_109	HATLASJ130054 + 260303	HerBS129	Ba18	13:00:54	+26:03:02.68	B	–	59.4 ± 5.9	85.4 ± 5.9	89.0 ± 7.0	Ba18
S_110	HATLASJ131322 + 285836	–	–	13:13:22	+28:58:35.61	B	–	160.8 ± 7.4	116.0 ± 8.4	68.0 ± 8.8	Ma18
S_111	HATLASJ134159 + 292833	–	–	13:41:59	+29:28:32.54	B	–	174.4 ± 6.7	172.3 ± 7.7	109.2 ± 8.1	Ne17
S_112	HATLASJ141833 + 010212	HerBS110	Ba18	14:18:33	+01:02:12.40	B	–	66.0	106.5	92.8	Ba18
S_113	HERMESJ142201 + 533214	HEGS01		14:22:01	+53:32:13.70	B	–	74.0	98.0	89.0	Ca14
S_114	HATLASJ142318.3 + 013913	–	–	14:23:18	+01:39:13.80	B	–	61.8 ± 7.5	83.0 ± 8.2	65.1 ± 8.8	Ma18
S_115	HATLASJ143203 − 005219	–	–	14:32:03	−00:52:19.00	B	–	160.6 ± 7.6	125.0 ± 8.3	76.1 ± 8.9	Ma18
S_116	HERMESJ143331 + 345440	HBootes01		14:33:31	+34:54:39.60	B	Unc.	158.0	191.0	160.0	Ca14
S_117	HATLASJ144243 + 015506	HerBS153	Ba18	14:42:43	+01:55:05.86	B	–	123.2 ± 7.2	133.4 ± 8.1	85.7 ± 8.8	Ba18
S_118	HATLASJ144715 − 012114	–	–	14:47:15	−01:21:14.00	B	–	132.7 ± 7.3	118.9 ± 8.2	74.7 ± 8.6	Ma18
S_119	HATLASJ222503.7 − 304847	HerBS166 UR085S	Ba18	22:25:04	−30:48:48.00	B	D	32.4 ± 7.2	50.1 ± 8.5	84.3 ± 10.3	Ba18
S_120	HATLASJ223942.4 − 333304	HerBS111	Ba18	22:39:42	−33:33:04.00	B	–	105.9 ± 6.5	115.6 ± 6.2	92.7 ± 7.4	Ba18
S_121	HATLASJ224026.5 − 315154	HerBS148	Ba18	22:40:27	−31:51:55.00	B	–	120.6 ± 5.0	121.2 ± 5.5	86.3 ± 6.8	Ba18
S_122	HATLASJ224759.6 − 310134	HerBS141	Ba18	22:48:00	−31:01:35.00	B	–	122.1 ± 6.1	124.4 ± 6.5	87.3 ± 7.5	Ba18
S_123	HATLASJ224805.3 − 335820	HerBS33	Ba18	22:48:05	−33:58:20.00	B	–	122.3 ± 5.7	135.5 ± 6.3	126.9 ± 7.2	Ne17
S_124	HATLASJ225045.5 − 304719	HerBS168	Ba18	22:50:46	−30:47:19.00	B	–	65.5 ± 6.1	88.1 ± 6.1	84.0 ± 7.5	Na16
S_125	HATLASJ230546.2 − 331038	HerBS49	Ba18	23:05:46	−33:10:39.00	B	–	76.8 ± 5.6	110.9 ± 5.9	110.4 ± 7.0	Ne17
S_126	HELMSJ231447.5 − 045658	HELMS44	Na16	23:14:48	−04:56:58.00	B	–	220.0 ± 8.0	141.0 ± 7.0	106.0 ± 8.0	Na16
S_127	HATLASJ232210.9 − 333749	HerBS146	Ba18	23:22:11	−33:37:49.00	B	–	122.4 ± 5.2	134.6 ± 5.4	86.6 ± 6.8	Ba18
S_128	HATLASJ232531.3 − 302235	HerBS17	Ba18	23:25:31	−30:22:36.00	B	–	175.5 ± 4.3	227.0 ± 4.7	175.7 ± 5.7	Ne17
S_129	HELMSJ232617.5 − 025319	HELMS51	Na16	23:26:18	−02:53:19.00	B	–	86.0 ± 6.0	109.0 ± 6.0	104.0 ± 7.0	Na16
S_130	HELMSJ232831.8 − 004035	HELMS55	Na16	23:28:32	−00:40:35.00	B	–	95.0 ± 7.0	120.0 ± 6.0	102.0 ± 7.0	Na16
S_131	HELMSJ232833.6 − 031416	HELMS48	Na16	23:28:34	−03:14:16.00	B	–	49.0 ± 6.0	104.0 ± 6.0	105.0 ± 8.0	Na16
S_132	HELMSJ233420.4 − 003458	HELMS43	Na16	23:34:20	−00:34:58.00	B	–	156.0 ± 7.0	141.0 ± 5.0	109.0 ± 8.0	Na16
S_133	HELMSJ233721.9 − 064740	HELMS49	Na16	23:37:22	−06:47:40.00	B	–	173.0 ± 6.0	161.0 ± 7.0	105.0 ± 8.0	Na16
S_134	HELMS233728.8 − 045106	HELMS20	Na16	23:37:29	−04:51:06.00	B	–	162.0 ± 6.0	178.0 ± 7.0	132.0 ± 8.0	Na16
S_135	HELMSJ234314.0 + 012152	HELMS36	Na16	23:43:14	+01:21:52.00	B	–	115.0 ± 6.0	115.0 ± 6.0	113.0 ± 8.0	Na16
S_136	HATLASJ234955.7 − 330833	HerBS184	Ba18	23:49:56	−33:08:33.00	B	–	91.9 ± 5.9	107.6 ± 6.0	82.3 ± 7.1	Ba18
S_137	HELMSJ235101.7 − 024425	HELMS50	Na16	23:51:02	−02:44:26.00	B	–	112.0 ± 6.0	124.0 ± 6.0	105.0 ± 7.0	Na16
S_138	HATLASJ235121.9 − 332902	HerBS159	Ba18	23:51:22	−33:29:02.00	B	Unc.	92.1 ± 5.9	98.3 ± 5.9	85.0 ± 7.1	Ba18
S_139	HELMSJ235331.7 + 031717	HELMS40	Na16	23:53:32	+03:17:18.00	B	–	102.0 ± 6.0	123.0 ± 7.0	111.0 ± 7.0	Na16
S_140	HATLASJ000455.3 − 330811	HerBS170	Ba18	00:04:55	−33:08:12.00	C	D	61.9 ± 5.4	78.8 ± 6.0	83.8 ± 7.0	Ba18
S_141	HATLASJ001030.1 − 330621	HerBS98	Ba18	00:10:30	−33:06:22.00	C	–	56.3 ± 4.9	51.7 ± 5.0	94.4 ± 6.5	Ba18
S_142	HELMSJ001226.9 + 020810	HELMS45	Na16	00:12:27	+02:08:10.00	C	–	107.0 ± 6.0	142.0 ± 6.0	106.0 ± 7.0	Na16
S_143	HELMSJ001325.7 + 042509	HELMS56	Na16	00:13:26	+04:25:09.00	C	–	89.0 ± 6.0	98.0 ± 6.0	102.0 ± 7.0	Na16
S_144	HATLASJ002144.8 − 295217	HerBS156	Ba18	00:21:45	−29:52:18.00	C	–	103.7 ± 5.7	91.3 ± 6.1	85.4 ± 6.9	Ba18
S_145	HELMSJ002719.5 + 001204	HELMS34	Na16	00:27:20	+00:12:04.00	C	–	248.0 ± 6.0	206.0 ± 7.0	116.0 ± 8.0	Na16
S_146	HERMESJ002854 − 420457	HELAISS04	Ca14	00:28:54	−42:04:57.00	C	–	131.0	102.0	58.0	Ca14
S_147	HELMSJ003519.7 + 072806	HELMS57	Na16	00:35:20	+07:28:06.00	C	–	134.0 ± 7.0	135.0 ± 7.0	101.0 ± 8.0	Na16
S_148	HATLASJ003728.7 − 284124	HerBS174	Ba18	00:37:29	−28:41:25.00	C	–	95.6 ± 5.7	84.8 ± 5.9	83.2 ± 7.4	Ba18
S_149	HELMSJ004622.3 + 073509	HELMS46	Na16	00:46:22	+07:35:09.00	C	–	82.0 ± 9.0	113.0 ± 9.0	105.0 ± 10.0	Na16
S_150	HATLASJ005132.8 − 301848	HerBS45	Ba18	00:51:33	−30:18:48.00	C	–	164.6 ± 5.4	160.2 ± 5.8	113.0 ± 7.2	Ne17
S_151	HELMSJ005258.6 + 061319	HELMS10	Na16	00:52:59	+06:13:19.00	C	D	88.0 ± 6.0	129.0 ± 6.0	155.0 ± 7.0	Na16
S_152	HATLASJ005849.9 − 290122	HerBS181	Ba18	00:58:50	−29:01:22.00	C	–	92.5 ± 5.7	116.6 ± 6.0	82.6 ± 7.2	Ba18
S_153	HATLASJ011014.5 − 314813	HerBS160	Ba18	01:10:14	−31:48:14.00	C	Unc.	48.6 ± 5.6	84.2 ± 6.0	84.8 ± 7.1	Ba18
S_154	HATLASJ011730.3 − 320719	HerBS138	Ba18	01:17:30	−32:07:19.00	C	–	120.4 ± 5.8	111.2 ± 6.4	87.4 ± 7.8	Ba18
S_155	HATLASJ012209.4 − 273824	HerBS114	Ba18	01:22:09	−27:38:24.00	C	–	81.7 ± 5.9	93.8 ± 6.0	91.8 ± 7.7	Ba18
S_156	HATLASJ012335.1 − 314618	HerBS145	Ba18	01:23:35	−31:46:19.00	C	D	54.7 ± 6.0	67.4 ± 6.2	86.8 ± 7.7	Ba18
S_157	HERSJ013212.2 + 001754	HERS18	Na16	01:32:12	+00:17:54.00	C	–	176.0 ± 7.0	175.0 ± 6.0	104.0 ± 8.0	Na16
S_158	HATLASJ013239.9 − 330906	HerBS40	Ba18	01:32:40	−33:09:07.00	C	–	112.0 ± 5.5	148.8 ± 6.2	117.7 ± 7.0	Ne17
S_159	HERSJ014057.3 − 010547	HERS14	Na16	01:40:57	−01:05:47.00	C	–	136.0 ± 8.0	143.0 ± 8.0	112.0 ± 9.0	Na16
S_160	HATLASJ014520.0 − 313834	HerBS107	Ba18	01:45:20	−31:38:35.00	C	–	97.3 ± 6.1	99.1 ± 6.4	93.1 ± 7.8	Ba18
S_161	HERSJ020529.1 + 000501	HERS19	Na16	02:05:29	+00:05:01.00	C	–	89.0 ± 6.0	112.0 ± 6.0	102.0 ± 8.0	Na16
S_162	HERMESJ021632 − 053421	HXMM14	Ca14	02:16:32	−05:34:21.00	C	–	98.0	98.0	78.0	Ca14
S_163	HERMESJ021837 − 035315	HXMM13	Ca14	02:18:37	−03:53:15.00	C	–	55.0	88.0	94.0	Ca14
S_164	HERMESJ021943 − 052433	HXMM20	Ca14	02:19:43	−05:24:33.00	C	D	85.0	79.0	67.0	Ca14
S_165	HERMESJ022206 − 070727	HXMM23	Ca14	02:22:06	−07:07:27.00	C	D	137.0	108.0	57.0	Ca14
S_166	HERMESJ022213 − 070222	HXMM28	Ca14	02:22:13	−07:02:22.00	C	–	27.0	47.0	87.0	Ca14
S_167	HERMESJ022251 − 032414	HXMM22	Ca14	02:22:51	−03:24:14.00	C	D	101.0 ± 6.0	85.0 ± 6.0	61.0 ± 6.0	Bu15
S_168	HERMESJ022515 − 024707	HXMM19	Ca14	02:25:15	−02:47:07.00	C	–	43.0	67.0	70.0	Ca14
S_169	HERMESJ022518 − 044610	HXMM27	Ca14	02:25:17	−04:46:10.00	C	–	0.0	48.0	43.0	Ca14
S_170	HERMESJ023006 − 034153	HXMM12	Ca14	02:30:06	−03:41:53.00	C	Unc.	98.0 ± 7.0	106.0 ± 8.0	82.0 ± 7.0	Bu15

Table B1 *– continued*

No.	IAU name	Alt. name	Ref.	RA [h m s]	Dec. [d m s]	Vis. class.	Multiw. class.	S_{250} [mJy]	S_{350} [mJy]	S_{500} [mJy]	Ref.
(1)	(2)	(3)	(4)	(5)	(6)	(7)	(8)	(9)	(10)	(11)	(12)
S_171	HERMESJ032434 − 292646	HECDFS08	Ca14	03:24:34	−29:26:46.00	C	–	104.0	67.0	54.0	Ca14
S_172	HERMESJ032443 − 282134	HECDFS03	Ca14	03:24:43	−28:21:34.00	C	–	83.0	118.0	113.0	Ca14
S_173	HERMESJ032713 − 285106	HECDFS09	Ca14	03:27:13	−28:51:06.00	C	–	77.0	66.0	51.0	Ca14
S_174	HERMESJ033118 − 272015	HECDFS11	Ca14	03:31:18	−27:20:15.00	C	–	45.0	52.0	42.0	Ca14
S_175	HERMESJ043341 − 540338	HADFS04	Ca14	04:33:41	−54:03:38.00	C	Unc.	74.0 ± 6.0	93.0 ± 6.0	84.0 ± 6.0	Bu15
S_176	HERMESJ043830 − 541832	HADFS02	Ca14	04:38:30	−54:18:32.00	C	D	19.0 ± 6.0	39.0 ± 5.0	52.0 ± 6.0	Bu15
S_177	HERMESJ044947 − 525427	HADFS09	Ca14	04:49:47	−52:54:27.00	C	D	98.0 ± 6.0	102.0 ± 6.0	72.0 ± 6.0	Bu15
S_178	HATLASJ083153 + 014014	–	–	08:31:53	+01:40:14.43	C	D	69.8 ± 7.3	93.0 ± 8.1	82.0 ± 8.6	Va16
S_179	HATLASJ083546 + 002804	–	–	08:35:46	+00:28:03.75	C	–	86.6 ± 6.6	94.5 ± 7.5	79.5 ± 8.0	Va16
S_180	HATLASJ083817 − 004134	HerBS108	Ba18	08:38:17	−00:41:34.00	C	–	84.5 ± 7.4	106.1 ± 8.2	93.0 ± 8.8	Ba18
S_181	HATLASJ083859.3 + 021325	HerBS169	Ba18	08:38:59	+02:13:25.87	C	–	95.2 ± 7.5	105.2 ± 8.2	84.0 ± 8.7	Ba18
S_182	HATLASJ083945 + 021023	HerBS171	Ba18	08:39:45	+02:10:22.83	C	–	71.3 ± 7.3	97.4 ± 8.1	83.4 ± 8.6	Ba18
S_183	HATLASJ084259.9 + 024959	HerBS188	Ba18	08:43:00	+02:49:59.02	C	–	84.2 ± 7.4	101.5 ± 8.1	81.8 ± 8.6	Ba18
S_184	HATLASJ085033 + 012914	–	–	08:50:33	+01:29:14.10	C	–	182.5 ± 6.9	131.6 ± 7.7	74.7 ± 8.0	Ma18
S_185	HATLASJ085126 + 014638	–	–	08:51:26	+01:46:38.37	C	–	66.4 ± 7.4	92.3 ± 8.1	79.1 ± 8.5	Va16
S_186	HATLASJ085309 − 005727	HerBS136	Ba18	08:53:09	−00:57:27.00	C	–	68.3 ± 7.5	97.5 ± 8.2	87.7 ± 8.6	Ne17
S_187	HATLASJ090953 − 010811	SDP.60		09:09:53	−01:08:11.00	C	–	152.1 ± 7.2	109.3 ± 8.1	83.5 ± 8.4	Va16
S_188	HATLASJ091454 − 010357	HerBS142	Ba18	09:14:54	−01:03:57.00	C	D	69.0 ± 7.3	72.2 ± 8.1	87.2 ± 8.5	Ba18
S_189	HATLASJ091809 + 001927	HerBS99	Ba18	09:18:09	+00:19:27.27	C	–	93.2 ± 7.4	116.6 ± 8.2	94.3 ± 8.7	Ba18
S_190	HATLASJ091857 − 000047	–	–	09:18:57	−00:00:47.00	C	–	171.6 ± 6.4	145.7 ± 7.4	85.1 ± 7.7	Va16
S_191	HATLASJ091949 − 005037	–	–	09:19:49	−00:50:37.00	C	–	150.7 ± 7.5	141.4 ± 8.4	90.4 ± 8.7	Va16
S_192	HATLASJ092141 + 005356	–	–	09:21:41	+00:53:55.58	C	–	71.2 ± 7.3	85.4 ± 8.2	79.6 ± 8.8	Va16
S_193	HERMESJ100057 + 022014	HCOSMOS02 COSBO3	Ca14	10:00:57	+02:20:13.70	C	D	70.0 ± 6.0	85.0 ± 6.0	71.0 ± 6.0	Bu15
S_194	HERMESJ103958 + 563120	HLock17	Wa13	10:39:58	+56:31:19.92	C	–	62.0	82.0	67.0	Ca14
S_195	HERMESJ104051 + 560654	HLock02 LSW102	Wa13	10:40:51	+56:06:54.14	C	–	53.0	115.0	140.0	Ca14
S_196	HERMESJ104140 + 570859	HLock11	Wa13	10:41:40	+57:08:59.42	C	–	97.0	112.0	80.0	Ca14
S_197	HERMESJ105712 + 565458	HLock03	Wa13	10:57:12	+56:54:58.25	C	–	114.0 ± 7.0	147.0 ± 10.0	114.0 ± 8.0	Ca14
S_198	HATLASJ113243 − 005109	HerBS71	Ba18	11:32:43	−00:51:09.00	C	–	68.0 ± 7.0	106.0 ± 8.0	100.0 ± 9.0	Ma19
S_199	HATLASJ113834 − 014657	HerBS119	Ba18	11:38:34	−01:46:57.00	C	–	68.5 ± 7.2	85.6 ± 8.1	91.2 ± 8.6	Ba18
S_200	HATLASJ114753 − 005832	HerBS85	Ba18	11:47:53	−00:58:32.00	C	–	92.1 ± 6.6	104.2 ± 7.4	96.0 ± 7.7	Ba18
S_201	HATLASJ115521 − 021332	HERBS179		11:55:21	−02:13:32.00	C	D	67.3 ± 7.2	84.9 ± 8.1	75.7 ± 8.9	Va16
S_202	HATLASJ115820 − 013754	HerBS66	Ba18	11:58:20	−01:37:54.00	C	–	120.0 ± 7.0	124.0 ± 8.0	101.0 ± 8.0	Ma19
S_203	HATLASJ120600.7 + 003459	HerBS74	Ba18	12:06:01	+00:34:59.51	C	–	88.7 ± 7.4	104.1 ± 8.1	98.8 ± 8.7	Ba18
S_204	HATLASJ120709.2 − 014702	HerBS51	Ba18	12:07:09	−01:47:03.00	C	–	143.2 ± 7.4	149.2 ± 8.1	110.3 ± 8.7	Ne17
S_205	HATLASJ121348.0 + 010812	HerBS116	Ba18	12:13:48	+01:08:12.59	C	–	65.1 ± 7.4	96.6 ± 8.2	93.6 ± 8.5	Ba18
S_206	HATLASJ121416.3 − 013704	HerBS164	Ba18	12:14:16	−01:37:04.00	C	–	88.0 ± 6.4	99.3 ± 7.4	84.3 ± 7.7	Ba18
S_207	HATLASJ121812.8 + 011841	HerBS83	Ba18	12:18:13	+01:18:41.67	C	D	49.5 ± 7.2	79.7 ± 8.1	94.1 ± 8.8	Ba18
S_208	HATLASJ122034.2 − 003805	HerBS197	Ba18	12:20:34	−00:38:06.00	C	–	81.9 ± 7.5	93.8 ± 8.2	84.8 ± 8.7	Ba18
S_209	HATLASJ122117.0 − 014924	–	–	12:21:17	−01:49:24.00	C	–	146.6 ± 7.4	128.9 ± 8.2	87.2 ± 8.3	Va16
S_210	HATLASJ122158.5 + 003326	HerBS124	Ba18	12:21:59	+00:33:26.15	C	–	135.7 ± 7.3	116.1 ± 8.2	89.8 ± 8.6	Ba18
S_211	HATLASJ122407.4 − 003247	HerBS161	Ba18	12:24:07	−00:32:47.00	C	D	56.5 ± 7.3	75.7 ± 8.1	82.4 ± 8.8	Ba18
S_212	HATLASJ122459.1 − 005647	HerBS150	Ba18	12:24:59	−00:56:47.00	C	D	53.6 ± 7.2	81.3 ± 8.3	92.0 ± 8.9	Ba18
S_213	HATLASJ125105 + 261653	NGP.2070		12:51:05	+26:16:52.62	C	–	116.5 ± 5.5	125.3 ± 6.5	81.3 ± 7.7	Va16
S_214	HATLASJ125653 + 275903	HerBS31	Ba18	12:56:53	+27:59:02.98	C	–	133.9 ± 7.5	164.1 ± 8.2	131.8 ± 8.9	Ne17
S_215	HATLASJ125810 + 263710	–	–	12:58:10	+26:37:09.99	C	–	131.6 ± 7.3	122.9 ± 8.3	78.8 ± 8.5	Ma18
S_216	HATLASJ130601 + 231322	–	–	13:06:01	+23:13:21.65	C	–	86.0 ± 7.3	88.0 ± 8.2	76.5 ± 8.6	Va16
S_217	HATLASJ131001 + 264759	–	–	13:10:01	+26:47:59.05	C	–	142.1 ± 7.3	124.1 ± 8.2	81.2 ± 8.9	Va16
S_218	HATLASJ131020 + 253731	–	–	13:10:20	+25:37:31.47	C	–	186.4 ± 7.3	158.7 ± 8.1	93.7 ± 8.5	Va16
S_219	HATLASJ131609 + 254931	–	–	13:16:09	+25:49:31.15	C	–	121.4 ± 7.3	108.2 ± 8.1	76.8 ± 8.7	Va16
S_220	HATLASJ131642 + 251158	–	–	13:16:42	+25:11:58.38	C	–	62.7 ± 6.9	71.5 ± 7.7	63.9 ± 8.1	Ma18
S_221	HATLASJ131805 + 325018	HerBS173	Ba18	13:18:05	+32:50:18.05	C	–	73.3 ± 5.6	92.7 ± 6.0	83.3 ± 7.2	Ba18
S_222	HATLASJ132128 + 282023	HerBS127	Ba18	13:21:28	+28:20:22.74	C	–	110.0 ± 5.5	122.7 ± 6.1	89.5 ± 6.9	Ba18
S_223	HATLASJ132227 + 300723	–	–	13:22:27	+30:07:22.54	C	–	48.0 ± 7.3	78.6 ± 8.2	25.0 ± 8.8	Va16
S_224	HATLASJ132302 + 341650	HerBS30	Ba18	13:23:02	+34:16:49.66	C	–	124.2 ± 7.3	144.6 ± 8.2	137.0 ± 8.7	Ne17
S_225	HATLASJ132419 + 320754	HerBS43	Ba18	13:24:19	+32:07:54.43	C	–	84.5 ± 6.8	116.0 ± 7.6	115.4 ± 8.0	Ne17

Table B1 – *continued*

No.	IAU name	Alt. name	Ref.	RA [h m s]	Dec. [d m s]	Vis. class.	Multiw. class.	S_{250} [mJy]	S_{350} [mJy]	S_{500} [mJy]	Ref.
(1)	(2)	(3)	(4)	(5)	(6)	(7)	(8)	(9)	(10)	(11)	(12)
S_226	HATLASJ132909 + 300958	HerBS204	Ba18	13:29:09	+30:09:58.23	C	–	57.9 ± 5.5	95.3 ± 6.1	80.1 ± 7.1	Ba18
S_227	HATLASJ133255 + 265529	–	–	13:32:55	+26:55:29.23	C	–	192.5 ± 7.4	167.4 ± 8.1	116.6 ± 8.6	Ne17
S_228	HATLASJ133256 + 342210	HerBS44 NA.v1.267	Ba18	13:32:56	+34:22:09.50	C	–	164.3 ± 7.5	186.8 ± 8.1	114.9 ± 8.7	Ne17
S_229	HATLASJ133440 + 353140	HerBS134	Ba18	13:34:40	+35:31:40.17	C	–	69.9 ± 5.9	97.3 ± 6.2	87.9 ± 7.3	Ba18
S_230	HATLASJ133534 + 341837	HerBS76	Ba18	13:35:34	+34:18:36.97	C	–	108.5 ± 5.9	124.3 ± 6.0	98.5 ± 7.0	Ba18
S_231	HATLASJ133623 + 343806	–	–	13:36:23	+34:38:05.88	C	–	78.8 ± 7.4	83.2 ± 8.3	79.1 ± 8.6	Ma18
S_232	HATLASJ133715 + 352058	–	–	13:37:15	+35:20:58.04	C	–	69.9 ± 7.5	88.1 ± 8.3	69.4 ± 8.8	Ma18
S_233	HATLASJ133905 + 340820	–	–	13:39:05	+34:08:20.20	C	–	59.3 ± 7.3	82.7 ± 8.2	70.1 ± 8.7	Va16
S_234	HATLASJ134124 + 354007	–	–	13:41:24	+35:40:06.58	C	–	62.9 ± 7.3	79.9 ± 8.2	82.2 ± 8.5	Va16
S_235	HATLASJ134139 + 322837	–	–	13:41:39	+32:28:37.34	C	–	39.8 ± 7.4	42.7 ± 8.1	80.1 ± 8.8	Va16
S_236	HATLASJ134403 + 242627	HerBS196	Ba18	13:44:03	+24:26:26.95	C	–	86.9 ± 5.7	92.3 ± 6.3	81.0 ± 7.1	Ba18
S_237	HATLASJ134442 + 240346	HerBS133	Ba18	13:44:42	+24:03:46.12	C	–	85.4 ± 5.5	98.5 ± 6.1	88.1 ± 7.3	Ba18
S_238	HATLASJ134654 + 295659	–	–	13:46:54	+29:56:59.06	C	–	85.0 ± 7.6	82.0 ± 8.3	77.8 ± 8.6	Va16
S_239	HATLASJ140422 − 001218	HerBS206	Ba18	14:04:22	−00:12:18.00	C	–	79.3 ± 7.4	102.6 ± 8.4	80.2 ± 8.8	Ba18
S_240	HATLASJ141118 − 010655	HerBS201	Ba18	14:11:18	−01:06:55.00	C	D	52.2 ± 7.2	78.6 ± 8.2	80.5 ± 8.7	Ba18
S_241	HATLASJ141810.0 − 003747	HerBS143	Ba18	14:18:10	−00:37:47.00	C	–	77.7 ± 6.5	97.3 ± 7.4	87.1 ± 7.9	Ba18
S_242	HATLASJ141955.5 − 003449	–	–	14:19:56	−00:34:49.00	C	–	76.4 ± 7.5	94.9 ± 8.0	80.2 ± 8.9	Va16
S_243	HERMESJ142549 + 345024	–	–	14:25:49	+34:50:23.57	C	–	48.0 ± 7.4	64.4 ± 8.3	52.9 ± 9.0	Ma18
S_244	HERMESJ142558 + 332549	HBootes09		14:25:58	+33:25:48.68	C	–	69.0	81.0	60.0	Ca14
S_245	HATLASJ142707 + 002258	HerBS130	Ba18	14:27:07	+00:22:57.60	C	–	119.4 ± 7.3	118.7 ± 8.1	88.8 ± 8.6	Ba18
S_246	HATLASJ143403.5 + 000234	HerBS147	Ba18	14:34:04	+00:02:34.34	C	–	103.3 ± 7.4	103.3 ± 8.1	86.6 ± 8.5	Ba18
S_247	HERMESJ143544 + 344743	HBootes12		14:35:44	+34:47:43.37	C	–	11.0	52.0	21.0	Ca14
S_248	HERMESJ144030 + 333843	HBootes07		14:40:30	+33:38:42.68	C	–	86.0	88.0	72.0	Ca14
S_249	HATLASJ144556.1 − 004853	G15v2.481 HerBS46	Ba18	14:45:56	−00:48:53.00	C	Unc.	126.7 ± 7.3	132.6 ± 8.4	111.8 ± 8.7	Ne17
S_250	HATLASJ144608.6 + 021927	HerBS38	Ba18	14:46:09	+02:19:27.01	C	–	73.4 ± 7.1	111.7 ± 8.1	122.1 ± 8.7	Ne17
S_251	HATLASJ145135.2 − 011418	HerBS126	Ba18	14:51:35	−01:14:18.00	C	–	81.9 ± 7.2	95.9 ± 8.2	89.8 ± 8.8	Ba18
S_252	HATLASJ145337.2 + 000407	HerBS137	Ba18	14:53:37	+00:04:07.94	C	–	86.0 ± 7.2	103.6 ± 8.0	87.7 ± 8.6	Ba18
S_253	HATLASJ145754 + 000017	HerBS195	Ba18	14:57:54	+00:00:17.07	C	–	70.3 ± 7.3	92.7 ± 8.1	81.0 ± 8.8	Ba18
S_254	HERMESJ161332 + 544358	HELAISN01		16:13:32	+54:43:57.76	C	–	123.0	129.0	88.0	Ca14
S_255	HERMESJ170508 + 594056	HFLS07	Ca14	17:05:08	+59:40:56.32	C	–	115.0	92.0	69.0	Ca14
S_256	HERMESJ170608 + 590921	HFLS03	Ca14	17:06:08	+59:09:21.28	C	–	98.0	105.0	81.0	Ca14
S_257	HERMESJ170818 + 582845	HFLS05	Ca14	17:08:18	+58:28:45.41	C	–	40.0	75.0	74.0	Ca14
S_258	HERMESJ172222 + 582611	HFLS10	Ca14	17:22:22	+58:26:10.82	C	–	52.0	50.0	32.0	Ca14
S_259	HERMESJ172612 + 583742	HFLS01	Ca14	17:26:12	+58:37:42.24	C	–	107.0	123.0	98.0	Ca14
S_260	HATLASJ222629.4 − 321111	HerBS144	Ba18	22:26:29	−32:11:12.00	C	–	98.9 ± 8.4	116.5 ± 8.2	87.0 ± 11.5	Ba18
S_261	HATLASJ224027.7 − 343134	HerBS97	Ba18	22:40:28	−34:31:35.00	C	–	96.1 ± 6.0	98.5 ± 6.3	94.4 ± 7.7	Ba18
S_262	HATLASJ224207.2 − 324159	HerBS67	Ba18	22:42:07	−32:41:59.00	C	Unc.	73.0 ± 5.5	88.1 ± 6.2	100.8 ± 7.7	Ne17
S_263	HATLASJ224400.8 − 340030	HerBS84	Ba18	22:44:01	−34:00:31.00	C	–	105.1 ± 5.9	123.0 ± 6.4	97.0 ± 7.6	Ba18
S_264	HATLASJ225324.2 − 323504	HerBS103	Ba18	22:53:24	−32:35:04.00	C	–	126.1 ± 5.3	131.2 ± 5.7	93.5 ± 7.0	Ba18
S_265	HATLASJ225339.1 − 325549	HerBS131	Ba18	22:53:39	−32:55:50.00	C	–	85.5 ± 5.2	99.7 ± 5.5	88.0 ± 6.9	Ba18
S_266	HATLASJ225611.6 − 325652	HerBS135	Ba18	22:56:12	−32:56:53.00	C	–	85.4 ± 5.5	96.7 ± 6.2	87.8 ± 7.5	Ba18
S_267	HATLASJ230002.6 − 315005	HerBS80	Ba18	23:00:00	−31:50:05.00	C	–	122.7 ± 5.7	121.1 ± 6.3	97.7 ± 7.6	Ba18
S_268	HATLASJ230538.5 − 312204	HerBS182	Ba18	23:05:39	−31:22:04.00	C	–	89.0 ± 5.7	109.1 ± 6.2	82.3 ± 7.9	Ba18
S_269	HATLASJ231205.1 − 295026	HerBS132	Ba18	23:12:05	−29:50:27.00	C	–	86.7 ± 5.8	102.6 ± 6.0	90.6 ± 7.8	Ba18
S_270	HELMSJ231857.2 − 053035	HELMS16	Na16	23:18:57	−05:30:35.00	C	–	143.0 ± 7.0	183.0 ± 7.0	146.0 ± 8.0	Na16
S_271	HATLASJ232200.0 − 355622	HerBS118	Ba18	23:22:00	−35:56:22.00	C	D	60.0 ± 6.3	84.3 ± 6.6	90.9 ± 7.7	Ba18
S_272	HATLASJ232419.8 − 323926	HerBS18 SC.v1.128	Ba18	23:24:20	−32:39:27.00	C	–	213.0 ± 4.4	244.2 ± 4.8	169.4 ± 5.8	Ne17
S_273	HELMSJ232558.3 − 044525	HELMS17	Na16	23:25:58	−04:45:25.00	C	–	190.0 ± 6.0	189.0 ± 6.0	142.0 ± 8.0	Na16
S_274	HATLASJ232623.0 − 342642	HerBS37 SB.v1.202	Ba18	23:26:23	−34:26:42.00	C	–	153.7 ± 4.4	178.3 ± 5.0	123.5 ± 6.2	Ne17
S_275	HELMSJ234014.6 − 070738	HELMS42	Na16	23:40:15	−07:07:38.00	C	–	158.0 ± 6.0	154.0 ± 6.0	110.0 ± 8.0	Na16
S_276	HELMSJ234951.6 − 030019	HELMS47	Na16	23:49:52	−03:00:19.00	C	–	186.0 ± 7.0	167.0 ± 6.0	105.0 ± 8.0	Na16
S_277	HERSJ010911.7 − 011733	HERS9	Na16	01:09:12	−01:17:33.00	D	–	393.0 ± 8.0	220.0 ± 8.0	118.0 ± 9.0	Na16
S_278	HATLASJ083345 + 000109	HerBS88	Ba18	08:33:45	+00:01:09.41	D	D	71.0 ± 7.6	96.0 ± 8.1	95.9 ± 8.8	Ba18
S_279	HATLASJ090613.8 − 010042	HerBS165	Ba18	09:06:14	−01:00:43.00	D	D	73.4 ± 7.4	80.2 ± 8.0	84.3 ± 8.7	Ba18
S_280	HATLASJ091238 + 020050	–	–	09:12:38	+02:00:49.71	D	–	173.2 ± 7.7	140.2 ± 8.2	97.6 ± 9.1	Ma18
S_281	HATLASJ142004 + 014045	–	–	14:20:04	+01:40:44.73	D	–	191.7 ± 7.5	150.1 ± 8.3	65.2 ± 8.7	Ma18

Notes. Column (1): source reference number. Column (2): IAU name of the *Herschel* detection. Columns (3) and (4): alternative name and reference. Columns (5) and (6): ICRS RA and Dec. coordinate (J2000.0) of the *Herschel* detection. Columns (7) and (8): visual and multiwavelength lens classifications. Columns (9), (10), (11), and (12): SPIRE flux density at 250, 350, and 500 μm, and reference.
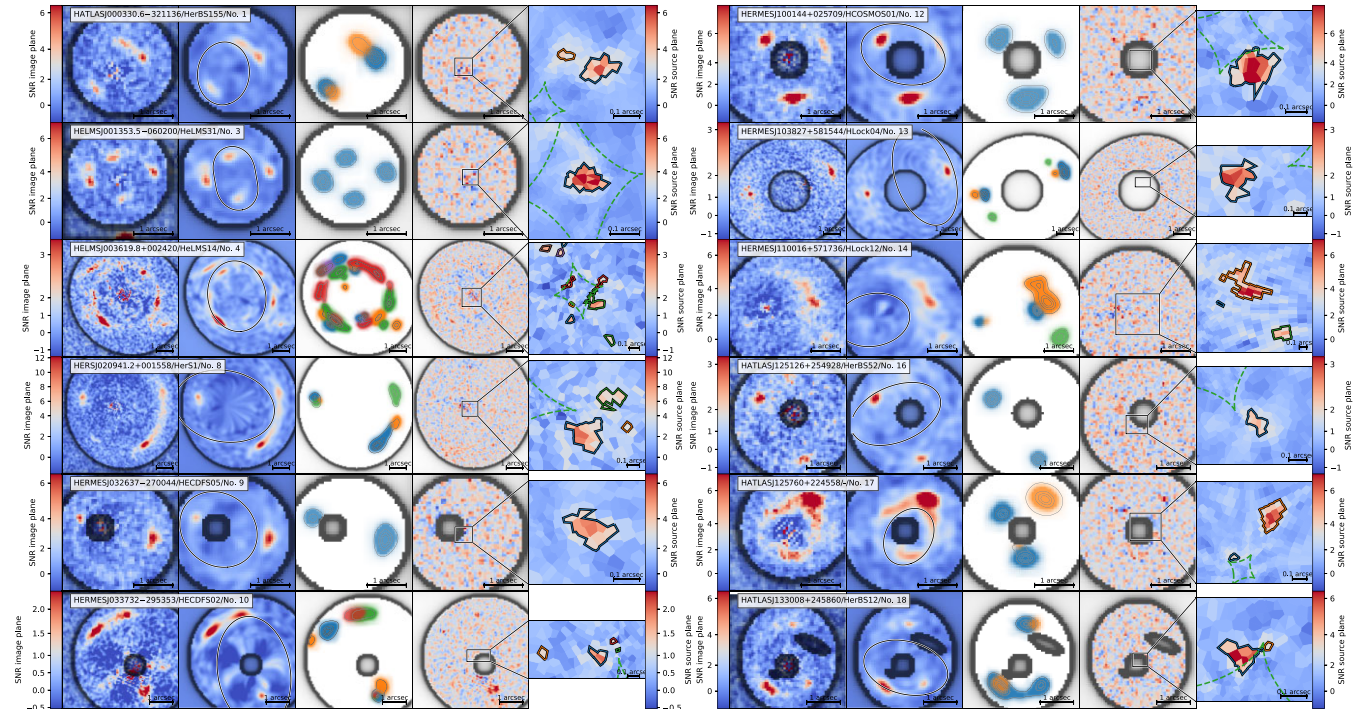
APPENDIX C: LENS MODELLING RESULTS

Figure C1. From left to right panels: lens-subtracted image, best-fitting model of the lensed source, SNR > 3 regions of the reconstructed source plane lensed back to the image plane, SNR map of the residuals obtained after subtracting the model of the lensed source from the input lens-subtracted image, and the reconstructed background source with caustic curves (dashed line). Each of the first three panels shows the pixel mask (black-shaded region) adopted for the lens modelling. The second panel from the left also shows the critical curves (continous curve). In the source plane image, we highlighted with black contours the SNR > 3 region adopted for computing the magnification and source size.
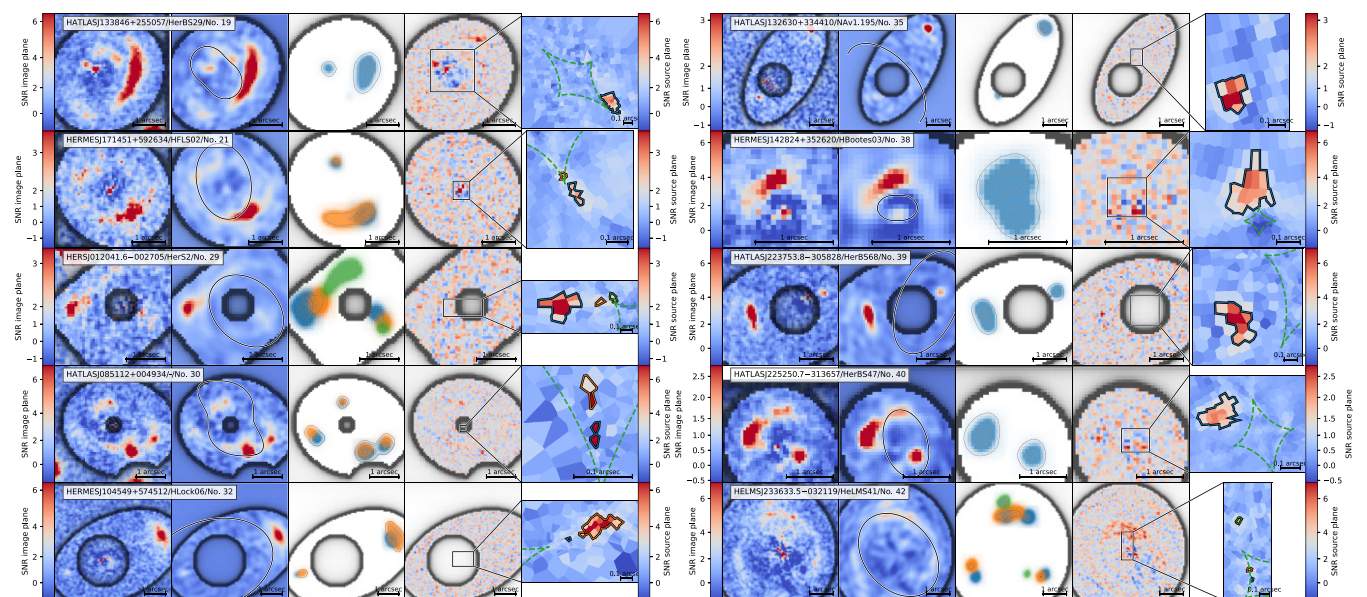

Figure C1. Continued.

[1]*Dipartimento di Fisica e Astronomia 'G. Galilei', Università di Padova, vicolo dell'Osservatorio 3, I-35122 Padova, Italy*

[2]*Department of Astronomy, University of Cape Town, 7701 Rondebosch, Cape Town, South Africa*

[3]*INAF – Istituto di Radioastronomia, Via Piero Gobetti 101, I-40129 Bologna, Italy*

[4]*Inter-University Institute for Data Intensive Astronomy, Department of Astronomy, University of Cape Town, 7701 Rondebosch, Cape Town, South Africa*

[5]*School of Physics and Astronomy, Cardiff University, The Parade, Cardiff CF24 3AA, UK*

[6]*INAF – Osservatorio Astronomico di Padova, vicolo dell'Osservatorio 2, I-35122 Padova, Italy*

[7]*Department of Physics and Astronomy, University of North Carolina Asheville, 1 University Heights, Asheville, NC 28804, USA*

[8]*Department of Physics, Institute for Computational Cosmology, Durham University, South Road, Durham DH1 3LE, UK*

[9]*Department of Physics and Astronomy, Rutgers, the State University of New Jersey, 136 Frelinghuysen Road, Piscataway, NJ 08854-8019, USA*

[10]*Department of Physics and Astronomy, University of the Western Cape, Robert Sobukwe Road, Bellville 7535, South Africa*

[11]*Division of Particle and Astrophysical Science, Graduate School of Science, Nagoya University, Aichi 464-8602, Japan*

[12]*National Astronomical Observatory of Japan, 2-21-1, Osawa, Mitaka, Tokyo 181-8588, Japan*

[13]*Institut d'Astrophysique Spatiale, Bât. 121, Université Paris-Sud, F-91405 Orsay Cedex, France*

[14]*Institut de Radioastronomie Millimétrique, 300 rue de la piscine, F-38406 Saint-Martin-d'Hères, France*

[15]*Physikalisches Institut, Universität zu Köln, Zülpicher Strasse 77, D-50937 Köln, Germany*

[16]*Blackett Lab, Imperial College, Prince Consort Road, London SW7 2AZ, UK*

[17]*Department of Physics and Astronomy, University of California, Irvine, CA 92697, USA*

[18]*Sorbonne Université, UPMC Université Paris 6 and CNRS, UMR 7095, Institut d'Astrophysique de Paris, 98bis boulevard Arago, F-75014 Paris, France*

[19]*Instituto de Astrofísica de Canarias, C/Vía Láctea, s/n, E-38205 San Cristóbal de La Laguna, Tenerife, Spain*

[20]*Dpto. Astrofísica, Universidad de La Laguna, E-38206 San Cristóbal de La Laguna, Tenerife, Spain*

[21]*School of Physics and Astronomy, University of Nottingham, University Park, Nottingham, NG7 2RD, UK*

[22]*Department of Physics and Astronomy 'Augusto Righi' (DIFA), University of Bologna, Via Gobetti 93/2, I-40129 Bologna, Italy*

[23]*INAF– Osservatorio di Astrofisica e Scienza dello Spazio, Via Gobetti 93/3, I-40129, Bologna, Italy*

[24]*Department of Physics and Astronomy, University of Hawai'i, 2505 Correa Road, Honolulu, HI 96822, USA*

[25]*Institute for Astronomy, University of Hawai'i, 2680 Woodlawn Drive, Honolulu, HI 96822, USA*

[26]*Departamento de Física, Universidad de Oviedo, C. Federico García Lorca 18, E-33007 Oviedo, Spain*

[27]*Instituto Universitario de Ciencias y Tecnologías Espaciales de Asturias (ICTEA), C. Independencia 13, E-33004 Oviedo, Spain*

[28]*Instituto Nacional de Astrofísica, Óptica y Electrónica, Luis Enrique Erro 1, Tonantzintla, Puebla, C.P. 72840, Mexico*

[29]*Aix-Marseille Universit'e, CNRS and CNES, Laboratoire d'Astrophysique de Marseille, 38 rue Frédéric Joliot-Curie, F-13388 Marseille, France*

[30]*Cosmic Dawn Center (DAWN), University of Copenaghen, Jagtvej 128, Tårn I, 2200, Copenhagen, Denmark*

[31]*DTU Space, Technical University of Denmark, Elektrovej 327, DK-2800 Kgs. Lyngby, Denmark*

[32]*SISSA, Via Bonomea 265, 34136 Trieste, Italy*

[33]*Centre de Recherche Astrophysique de Lyon, Université Lyon 1, ENS de Lyon, CNRS UMR5574, F-69230 Saint-Genis-Laval, France*

[34]*Department of Physics and Astronomy, University of British Columbia, 6224 Agricultural Road, V6T 1Z1, Vancouver, B.C.,, Canada*

[35]*School of Physical Sciences, The Open University, Walton Hall, Milton Keynes, MK7 6AA, UK*

[36]*Leiden Observatory, Leiden University, PO Box 9513, NL-2300 RA, Leiden, The Netherlands*

[37]*Department of Physics and Astronomy, Inter-University Institute for Data Intensive Astronomy, University of the Western Cape, 7535 Bellville, Cape Town, South Africa*

[38]*SRON Netherlands Institute for Space Research, Landleven 12, NL-9747 AD, Groningen, The Netherlands*

[39]*Kapteyn Astronomical Institute, University of Groningen, Postbus 800, NL-9700 AV, Groningen, The Netherlands*

[40]*Department of Earth and Space Sciences, Chalmers University of Technology, Onsala Observatory, SE-439 94 Onsala, Sweden*

This paper has been typeset from a TEX/LATEX file prepared by the author.